Chair of Petroleum and Geothermal Energy Recovery

Master's Thesis

CFD Analysis of Ground Source Heat Exchangers

Constantin Julian Dörr, BSc

October 2020

Master's Thesis

CFD Analysis of Ground Source Heat Exchangers

Written by:
Constantin Dörr
01335658

Internal Advisors:
Univ.-Prof. Dipl.-Ing. Dr.mont. Herbert Hofstätter
Dipl.-Ing. Fatemeh Fazeli Tehrani

External Advisor:
Dipl.-Ing. Dr. Christoph Reichl

Leoben, October 2020

MONTANUNIVERSITÄT LEOBEN
www.unileoben.ac.at

EIDESSTATTLICHE ERKLÄRUNG

Ich erkläre an Eides statt, dass ich diese Arbeit selbständig verfasst, andere als die angegebenen Quellen und Hilfsmittel nicht benutzt, und mich auch sonst keiner unerlaubten Hilfsmittel bedient habe.

Ich erkläre, dass ich die Richtlinien des Senats der Montanuniversität Leoben zu "Gute wissenschaftliche Praxis" gelesen, verstanden und befolgt habe.

Weiters erkläre ich, dass die elektronische und gedruckte Version der eingereichten wissenschaftlichen Abschlussarbeit formal und inhaltlich identisch sind.

Datum 29.10.2020

Unterschrift Verfasser/in
Constantin Julian, Dörr

Acknowledgements

First and foremost, I wish to express my sincere appreciation to my supervisor, *Dipl.-Ing. Dr. Christoph Reichl*, for providing constant guidance and detailed feedback, as well as necessary information and direction.

Additionally, I would like to thank the entire *Austrian Institute of Technology's GEOFIT* team for their contributions and support. The transition to remote office work and regular video conference meetings amidst the *COVID-19* pandemic has worked seamlessly. Therefore, I am incredibly grateful that the work-flow and time-frame of this thesis was not affected by the pandemic. I would like to thank *Dipl.-Ing. Dr. Michael Lauermann* and *Dipl.-Ing. Stephan Kling*, who have provided the experimentally measured data and played large organisational roles in my thesis from the AIT's side.

I would also like to recognise the invaluable assistance of my predecessor *Alexander Steurer, B.Sc.* in particular, who has taught me the CFD modelling and mesh building skills necessary to complete this thesis and who was always available to answer any further questions I had.

I would like to thank my supervisor *Dipl.-Ing. Fatemeh Fazeli Tehrani* from the *University of Leoben* for the swift and flawless organisation of my thesis from the university's side, as well as the fast responses to any questions I had.

I wish to show my gratitude to my wife *Claire Dörr, M.Sc.* for her continued support as well as for proofreading my thesis.

Finally, my deepest appreciation goes to my parents for their support throughout my life and studies.

Kurzfassung

Diese Masterarbeit wurde in Zusammenarbeit mit dem österreichischen Forschungsinstitut *Austrian Institute of Technology (AIT)* im Rahmen des *GEOFIT* Forschungsprojektes durchgeführt, welches Teil des Förderprogrammes *Horizon 2020* der Europäischen Union ist. Das Ziel dieser Masterarbeit ist die Modellierung des Wärmeflusses im unmittelbaren Umfeld von kompakten Erdwärmetauschern in unterschiedlichen Substraten. Die Lösungen dieser sogenannten Nahfeldmodelle werden als Eingabeparameter für die weitere Fernfeldmodellierung dienen, die von den *GEOFIT*-Partnern des AIT durchgeführt wird. Erdwärmekörbe und Ringgrabenkollektoren stellten sich für diesen Zweck als am besten geeignete geometrische Erdwärmetauscherkonfigurationen heraus und entsprechende Modelle mit der CFD-Software *ANSYS Fluent* wurden entwickelt.

Der Einfluss der Materialeigenschaften Wärmeleitfähigkeit und Wärmediffusivität des wärmeleitenden Mediums auf den Wärmetransport wurde für Sande und Humuserden mit unterschiedlichem Feuchtegehalt untersucht. Da die Variation des wärmeleitenden Substrats im großräumigen Erdwärmekorbexperiment des AIT einen großen Zeit- und Arbeitsaufwand erfordert, wurde ein kleineres „Thermo-Pipe“ Experiment entwickelt. Das Ziel des Thermo-Pipe Experimentes ist, das thermische Verhalten verschiedener wärmeleitender Substrate zu modellieren und zu testen, bevor sie im großen Erdwärmekorbexperiment eingesetzt werden. Das entsprechende CFD-Modell wurde im Rahmen dieser Arbeit ebenfalls entwickelt und dessen Ergebnisse mit den experimentell gemessenen Daten verglichen. Um die Ergebnisse der Erdwärmetauschermodelle weiter zu untermauern, wurden außerdem die maßgeblichen physikalischen Konzepte des Wärmetransports der numerischen *ANSYS Fluent* Software untersucht. Um den analytischen Rechenaufwand zu reduzieren und damit eine analytische Lösung zu ermöglichen, wurde ein geometrisch vereinfachtes Modell erstellt. Die analytisch berechnete Lösung wurde dann mit der numerisch berechneten Lösung der Software verglichen und zeigte sehr genaue Übereinstimmungen für unterschiedliche zeitunabhängige Wärmeeinträge. Aus der analytischen Lösung lässt sich ableiten, dass die Wärmeleitfähigkeit die einzige Materialeigenschaft ist, die in der stationären Lösung auftritt und somit die maximal auftretende Temperatur beim Erreichen des thermischen Gleichgewichts direkt beeinflusst. Die Wärmediffusivität, die auch Temperaturleitfähigkeit genannt wird, tritt dagegen ausschließlich im instationären Bereich der Lösung auf und beeinflusst die Zeit die benötigt wird, bis das thermische Gleichgewicht im System erreicht ist. Um die Ergebnisse der Wärmetauschermodelle zu validieren, wurden sie mit einem bereits vorhandenen Modell und einem entsprechenden Experiment verglichen, welche vom AIT erstellt wurden.

Diese Arbeit trägt zur Grundlage der Zielsetzung des *GEOFIT*-Projekts bei, nämlich ein „Engineering Tool“ basierend auf akkuraten Wärmestrommodellen zur genauen Auslegung kompakter Erdwärmetauscher zu entwickeln, welche zur geothermischen Nachrüstung europäischer Haushalte geeignet sind.

Abstract

This master's thesis was conducted in collaboration with the *Austrian Institute of Technology (AIT)* as part of the *GEOFIT* research project's framework, funded by the European Union's *Horizon 2020* programme.

The objective of this thesis is to model heat flow in the vicinity or "near-field" of non-standard compact ground source heat exchangers in varying substrates. Earth baskets and horizontal slinky heat exchangers have been chosen as the most suitable geometric configurations to be examined and corresponding models with the CFD software *ANSYS Fluent* were developed.

The influence of the heat conducting medium's material properties affecting the heat transport, namely the thermal conductivity and thermal diffusivity, was investigated for sands and soils with varying moisture content. As the variation of the heat conducting substrate in the AIT's large-scale earth basket experiment requires significant time and man-power, a small-scale experiment named the "Thermo-Pipe" was developed at AIT. The objective of the Thermo-Pipe is to model and test the thermal response of varying heat conducting substrates before they qualify to be used in the large-scale experiment. The corresponding model has been developed as part of the framework of this thesis as well and its matching results were compared to the experimentally measured data. Additionally, to further substantiate the models' results, the governing physical concepts of heat transport incorporated in the numeric *ANSYS Fluent* solver were investigated. This was accomplished through creating a geometrically simplified model, to reduce the calculation effort and thus make an analytical solution possible.

The analytically calculated solution was then compared to the solver's numerically calculated solution and showed highly accurate matches for varying time-independent heat inputs. The analytical solution has shown that the thermal conductivity is the sole material property appearing in the steady-state solution and thus directly influences the maximum temperature reached at the system's thermal equilibrium. The thermal diffusivity on the other hand appears in the transient solution and influences the time it takes until the thermal equilibrium is reached. This could be observed in the CFD solutions for varying substrates as well. To validate the results of the heat exchangers' models, they were compared to a pre-existing model and corresponding experiment, developed at AIT.

The solutions of these near-field models will serve as input parameters for further far-field modelling, conducted by the AIT's *GEOFIT* partners. This thesis aims to contribute to the groundwork of the *GEOFIT* project's greater objective, to develop an engineering design tool through accurate heat flow modelling for compact ground source heat exchangers applicable in large-scale geothermal retrofitting of pre-existing European housing.

Table of Contents

List of Figures

List of Tables

List of Symbols

The following list describes several symbols that will be later used within the body of the document.

Greek Letters

α	Thermal Diffusivity	($m^2\,s^{-1}$)
ϑ	Temperature	($^\circ C$)
λ	Thermal Conductivity	($W\,m^{-1}\,K^{-1}$)
λ_x	Thermal Conductivity in x-direction	($W\,m^{-1}\,K^{-1}$)
μ_n	Eigenvalues	(m^{-2})
ξ	Position of the Maximum of the Source Function	(m)
ρ	Density	($kg\,m^{-3}$)
σ	Bell Curve Width of the Source Function	(m^{-2})

Latin Letters

A	Amplitude of the Source Function	($W\,m^{-3}$)
c	Specific Heat Capacity	($J\,kg^{-1}\,K^{-1}$)
c_p	Specific Heat Capacity at Constant Pressure	($J\,kg^{-1}\,K^{-1}$)
F_n	Eigenfunctions	(1)
h	Convective Heat Transfer Coefficient	($W\,m^{-2}\,K^{-1}$)
i	Imaginary Unit	(1)
L	Length of the Rod Model	(m)
m	Mass	(kg)
Q	Amount of Heat	(W)
$Q(x)$	Time-Independent Heat Source	($W\,m^{-3}$)
q	Heat Flux	($W\,m^{-2}$)
s	Additional Position Variable for Integration	(m)
T	Total Temperature Solution	(K)
$\tilde{T}$	Transient Temperature Solution	(K)
T^*	Steady-State Temperature Solution	(K)
t	Time	(s)
u_x	Fluid Velocity in x-direction	($m\,s^{-1}$)
x	Position	(m)

Number Sets

$\mathbb{N}$	Set of Natural Numbers Including Zero
$\mathbb{R}$	Set of Real Numbers

List of Abbreviations

The following list describes several abbreviations that will be later used within the body of the document.

AIT Austrian Institute of Technology . . . iii

CAD Computer-Aided Design . . . 43

CAS Computer Algebra System . . . 32

CFD Computational Fluid Dynamics . . . 1

HFM Heat-Flow-Meter . . . 40

l.h.s. left hand side . . . 27

ODE Ordinary Differential Equation . . . 27

PDE Partial Differential Equation . . . 26

r.h.s. right hand side . . . 27

RTD Resistance Temperature Detector . . . 39

SI International System of Units . . . 17

TRT Thermal Response Test . . . 3

1 Introduction

Technologies which increase the energy efficiency of residential buildings are beginning to play a central role in renewable energy policies of European states. A multitude of European governments have placed considerable attention and resources, aimed at retrofitting residential housing to higher energy efficiency standards, through direct government grants or funded research projects (Rau et al., 2019). Thus, an opportunity presents itself for geothermal heating technologies.

The research project *GEOFIT*, funded by the European Union's *Horizon 2020* programme, aims to take this opportunity and address a variety of research topics connected to geothermal retrofitting of residential housing. One of the research topics is the design and construction of shallow ground source heat exchangers in urban environments, where surface area is limited and drilling solutions for vertical borehole heat exchangers in individual households are not viable. This is due to pre-existing underground city services infrastructure. An objective of the *GEOFIT* research project is the creation of a better understanding of unconventional compact shallow ground source heat exchangers and to subsequently increase their technology readiness level. The focus of this thesis is placed on two non-standard ground source heat exchanger designs, namely the earth basket and the horizontal slinky heat exchanger. Furthermore, Computational Fluid Dynamics (CFD) models simulating the heat flow in the immediate vicinity or near-field of these heat exchanger types have been created as part of the framework of this thesis. They will contribute to the necessary research groundwork and subsequently aid in the development of accurate engineering tools for compact shallow ground source heat exchangers.

To substantiate these models, a pre-existing earth basket experiment with a corresponding model was developed by the AIT. As previously mentioned, the heat flow in the near-field of the earth basket heat exchanger geometry is investigated by the AIT's *GEOFIT* team. In order to accurately measure this heat flow in the substrate surrounding the heat exchanger under experimental conditions, the direction of the heat flow has been reversed in the experiment. A heating cable, on which a constant and measurable heat input can be applied to, was used as a heat source and has been moulded into the helical shape of an earth basket. Accurate temperature sensors were placed in the substrate surrounding the heating coil. In order to accurately control the ambient temperature, the large box containing this experimental setup was placed in a cooling chamber. The temperature field inside the container is then recorded until the thermal equilibrium is reached. Probes of the experiment's substrate were taken and the material properties thermal conductivity, specific heat capacity and in-situ bulk density were accurately measured by the AIT laboratory engineers. These material parameters were then used to develop CFD models with the measured parameters describing the heat conductive medium. In order to create a basis for a meaningful comparison between experiment and simulation, the models have been setup identically to the experiment. The recorded tem-

perature data of the AIT's earth basket experiment and the corresponding CFD simulation's results are compared in chapter seven. An accurate match will further validate the additional models of geometric and material property variations, that were created with identical external parameters such as control volume, boundary and initial conditions and heat input as part of the framework of this thesis. Their results will be presented towards the end of this thesis, in chapters eight and nine.

To further support these models, the physical concepts of heat conduction used by the numeric solver have been verified by comparing an analytically calculated solution with results of the numeric solver. In order to make an analytical solution possible, the calculation effort had to be significantly reduced. Thus, a geometrically simplified rod model was created, whose solution could be calculated by solving the one-dimensional heat equation with a time-independent source term. The solutions' accuracy was then tested for a heat input function depending on the position with varying amplitudes, maximum positions and curve widths. These results, as well as the calculation steps are presented in chapter five.

As the previously explained earth basket experiment has large dimensions, varying the heat conductive medium is a time-consuming process. Therefore, a small-scale experiment named the "Thermo-Pipe" was developed by the AIT, to test the heat conductive behaviour of substrates before they are implemented in the large-scale earth basket experiment. If the "Thermo-Pipe" experiment and corresponding model provide matching and satisfying results, the tested heat conductive medium may be used in an experimental run of the slinky heat exchanger experiment. The corresponding CFD model was developed as part of the framework of this thesis and the experimental results are compared to the simulated data in chapter six.

Before the developed double earth basket and horizontal slinky heat exchanger models, as well as the material property variation, are presented and discussed, a brief literature review of the functionality and applications of shallow ground source heat exchangers and the basic physical principles behind heat transport will be presented in chapters three and four respectively. In the following chapter two, the *GEOFIT* research project and the contribution of this thesis will be presented in detail.

2 The *GEOFIT* Research Project

GEOFIT (Grant Agreement No. 792210) is a research project funded by the European Union's *Horizon 2020* programme incorporating 24 partners across the EU. The project began in *May 2018* and its expected duration is 4 years; furthermore, the coordination of the project is located in Italy. The goal of the project is to implement and deploy cost effective geothermal systems through energy efficient building retrofitting. According to "GEOFIT – Project Objectives" (2020), the building industry is responsible for over a third of Europe's annual CO_2 emissions. Hence, the call for the project arose due to European targets for energy efficient and renewable energy in existing buildings.

2.1 Objectives

An opportunity presents itself, whereby shallow geothermal applications can be utilised in buildings. However, it should be noted that its adoption is hampered by long installation times and costs. Additionally, technical difficulties arise when coupling heat pumps with existing high temperature heating systems, as well as the risk of structural damages resulting from drilling activities. The *GEOFIT* project intends to mitigate these hindrances through the following goals: [1]

1. Innovative geothermal systems, whereby the systems are specifically developed for geothermal based retrofitting. This encompasses an optimisation and integration of the geothermal system's components, as well as novel heat exchange concepts. Furthermore, the project will incorporate cost effective heat pumps, innovative heating and cooling components, as well as progressive IT control and monitoring technologies.

2. Integrate advanced methods of work site inspection, such as ground research, building structural monitoring, Thermal Response Test (TRT) methods and work site characterisation. The approach used to achieve this is a multi-stakeholder and collaborative method, grounded predominantly on integrated delivery projects.

3. For the stock of existing buildings in Europe, the goal is to implement a global, energy-efficient retrofitting strategy.

[1] *GEOFIT – project objectives*. (2020). Retrieved February 26, 2020, from https://geofit-project.eu/project/objectives/

2.2 Problem Description

The *GEOFIT* project intends to use compact geothermal heat exchangers, as an alternative to the currently most wide spread ground source heat exchanger systems in Europe, namely; vertical borehole heat exchangers. These heat exchangers are installed at depths ranging between 100 m and 300 m and have been used for more than 30 years worldwide. However, this technology has a number of disadvantages, which do not make it suitable for efficient large-scale building retrofitting in densely populated areas. Namely, high installation costs created through drilling and environmental concerns when water bearing formations are traversed. Furthermore, in urban environments this technology isn't suitable due to pre-existing and complex underground city services infrastructure. The solution to these issues are shallow compact ground source heat exchangers such as helical slinky heat exchangers or "earth baskets". These non-standard heat exchangers are pivotal in retrofit applications, to reduce costs and to enable the retrofitting to geothermal heating systems, where drilling is not possible and large available surface areas are not a given ("GEOFIT – Compact Geothermal Heat Exchangers", 2020).

Thus, a study has been conducted on the limiting factors of non-standard, compact ground source heat exchangers ("GEOFIT – Compact Geothermal Heat Exchangers", 2020). One of the limiting factors is the absence of standardised TRT methods specifically designed for non-standard and highly flexible configurations. The lack of specific TRT methods makes contractors and installers choose other types of heat exchangers with standardised TRT methods, such as vertical borehole heat exchangers. Due to the high grade of uncertainty and since the optimal heat exchanger configurations (depending on the required thermal capacity) are not exactly known, most of these installations have been drastically over-sized. Often to the point, where their initial cost benefits over other technologies were mitigated. This reduced the acceptance of the technology, due to the perceived risks and higher costs due to over-sizing.

2.3 Work Package Three

The AIT's *GEOFIT* deliverable addresses this issue as a part of the *GEOFIT* work package three. As described in "GEOFIT – Project Objectives" (2020), in order to allow geothermal systems to be retrofitted in urban areas where drilling proves to be economically not viable, as well as to reduce the overall cost, alternatives such as compact geometries based on helical slinky heat exchangers or "earth baskets" have been considered and will be optimised. Such non-standard heat exchangers for limited spaces are essential in retrofit applications, for reducing costs and allowing systems to be realised where deep drilling is not possible. The state of the art will be advanced through field-test campaigns in a variety of European countries and with a variety of housing types and by developing new test methods. The *GEOFIT* project aims to target the development and standardisation of special TRT methods for novel shallow heat exchanger designs, such as basket and helix configurations ("GEOFIT

– Compact Geothermal Heat Exchangers", 2020).

Experimentally validated CFD models of heat exchangers will enable the optimisation of individual heat exchangers' configurations and thus, further significantly advance the current state of the art ("GEOFIT – Compact Geothermal Heat Exchangers", 2020). The ultimate goal of the WP3 deliverable, namely the development of design tools which are derived from accurate heat flow models, will ensure that the ground source heat exchanger is not over or under-sized and possesses the optimal thermal and economical design required for the respective heating or cooling capacity at the intended efficiency ("GEOFIT – Compact Geothermal Heat Exchangers", 2020).

2.3.1 Thesis Contribution

This thesis contributes to the AIT's work package three deliverable of the *GEOFIT* project. A CFD analysis with the software *ANSYS Fluent* of different slinky heat exchanger geometries will be performed in order to advance the understanding of heat flow around slinky heat exchangers in different substrates. The models' results are then compared to a pre-existing experiment with a corresponding model conducted by the AIT. The AIT is responsible for researching the heat flow through the ground's substrate in the compact heat exchanger's vicinity or "near-field" through CFD modelling and experimental runs. The work package three partners like *EURECAT* from Spain or *Groenholland* from the Netherlands simultaneously model the thermal "far-field" behaviour and use the AIT's computed near-field results as input data. Therefore, the results of the models presented in this thesis can be exported onto a cylindrical shaped surface at every time step, which serves as an input parameter for the AIT's *GEOFIT* partners responsible for further far-field modelling. This will contribute towards the larger *GEOFIT* goal previously discussed, namely the development of TRT methods and engineering design tools for compact shallow ground source heat exchangers ("GEOFIT – Project Objectives", 2020). Addressing the issue from the point of view of the client, the risks and costs involved with over and under-sized ground source heat exchangers will be mitigated, as the engineering tool will allow designers and engineers to accurately verify site conditions and design parameters ("GEOFIT – Project Objectives", 2020). Therefore, the risk of choosing geothermal technology will be greatly reduced and its acceptance increased.

3 Shallow Ground Source Heat Exchangers

Shallow geothermal energy is a renewable energy source which is available almost everywhere, offering a clean energy form as an alternative to fossil fuels (Javadi et al., 2019). Generally, shallow geothermal energy systems pertain wells with a depth fewer than 250 m, whereby heat is exchanged with the ground to provide heating and cooling to buildings (Javadi et al., 2019). As discussed by Florides and Kalogirou (2007), the temperature of the ground at a specific depth remains fairly constant throughout the year and the ground capacitance can therefore be regarded as a passive source of heating and cooling. They further elaborate, that the reason for this constant temperature is due to the diminishment of temperature fluctuations below the surface of the ground. This is a result of the high thermal inertia of the soil as the depth of the ground increases. Thus, at a sufficient depth, the ground temperature will always be higher than that of the outside air in winter and lower in summer (Florides & Kalogirou, 2007). This difference in temperature between the ground and outside air can be utilised as preheating means in winter and pre-cooling in summer. In order to harness this heat effectively, a heat-exchanger system is constructed (Florides & Kalogirou, 2007).

3.1 Open Loop Systems

There are two types of ground source heat exchangers; namely, open (ground-water) and closed (ground-coupled) systems (Javadi et al., 2019). As shown in Figure 1a below, in most cases in open systems two wells are required, one is required to extract the ground water and the other injects it back into the water-bearing layer (Florides & Kalogirou, 2007). Proper planning is required when using a production / injection doublet, for example the amount and rate of water abstraction and the distance between the two wells (Manzella, 2015). However, it is possible that a single open well can be utilised instead, whereby the ground water is not re-injected back into the aquifer. Instead, the water is released at the surface and the cost of a second borehole is mitigated. However, this is only recommended when there are no negative environmental impacts or risk of reducing the groundwater level (Manzella, 2015). Open systems pertain the advantages of utilising natural water which is “free” for cooling or drinking depending on its quality (Manzella, 2015). Additional cost reductions can be realised by using the single well configuration, whereby the water is released at the surface into a nearby pond, stream or sewage system. Open loop systems generally absorb more heat from the ground than a comparable closed loop configuration of similar size (Manzella, 2015).

3.2 Closed Loop Systems

The other type of ground source heat exchanger is a closed system, where continuous pipe loops are placed horizontally or vertically in the ground and circulate the heat carrier fluid (Eswiasi & Mukhopadhyaya, 2020). These pipes are typically made from high-density polyethy-

lene and contain a mixture of water and anti-freeze on Glycol basis (Manzella, 2015). In shallow geothermal applications these closed systems are the most common. A schematic representation of a closed loop system is displayed in Figure 1b below. In the horizontal option, pipes are placed in either series or parallel arrangements. Furthermore, in the horizontal configuration pipes are also occasionally placed in curled loops called "slinky" arrangements, for land space saving purposes, while still maximising the heat exchanger's surface contact with the ground (Eswiasi & Mukhopadhyaya, 2020).

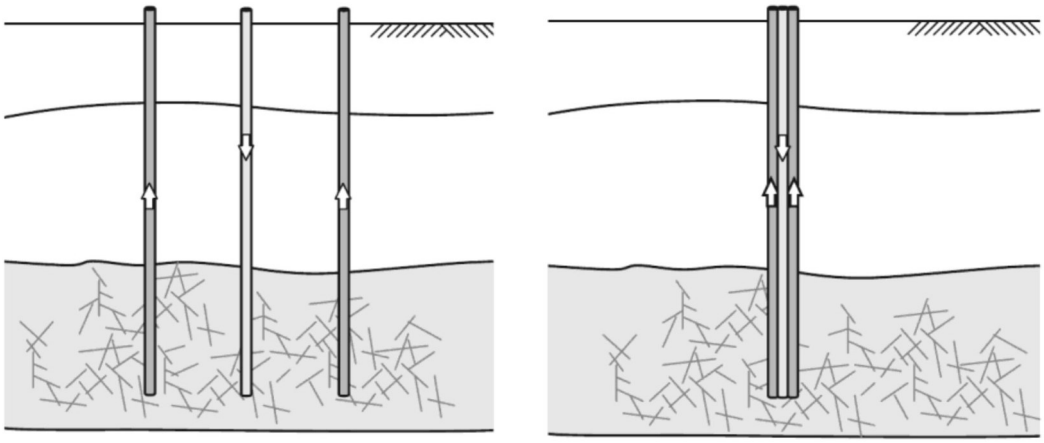

(a) Open Loop System (b) Closed Loop System

Figure 1: Schematic representation of open and closed loop geothermal systems. [1]

3.2.1 Borehole Heat Exchangers

Vertical ground source heat exchangers, also more commonly known as borehole heat exchangers, are installed when a significant heat exchange capacity is required and the surface area is limited (Florides & Kalogirou, 2007). The depth of borehole heat exchangers varies significantly and largely depends on the required capacitance and the local geothermal gradient. Said gradient has an average value of $3.5\ ^{\circ}C$ per 100 m, but may vary significantly depending on the geographic location. Depending on national law, private applications may reach depths between 250 m and 300 m. The high temperatures reached in these installations may therefore not only be utilised for spatial room heating, but also for hot water applications, thus mitigating the necessity for electric or gas powered boilers. After the borehole is drilled the tubing is installed in various configurations, such as single or double U-tubes or coaxial tubing, and fixated by a thermally conductive grouting (Javadi et al., 2019). The challenge in these installations lies in the high temperature difference between inlet and outlet, whereby the flow and return tubing are situated in each others vicinity inside the borehole. To minimise the cooling effect of the return flow in the upper part of the borehole, insulation material should be applied cautiously.

[1] Reprinted from Al-Khoury, R. (2011). *Computational modeling of shallow geothermal systems*. CRC Press, p. 4

3.2.2 Horizontal Heat Exchangers

Horizontal ground source heat exchangers are the most cost-effective arrangement, as their trenches are easy to dig (Javadi et al., 2019). However, it should be noted that horizontal ground source heat exchangers require a large surface area and are therefore rarely used in the heating and cooling of larger buildings in densely populated areas (Manzella, 2015). In order to maximise the horizontal heat exchanger's surface contact with the ground and to minimise the large surface area required, the underground piping may be arranged in many geometrical variations of beneficial loops and coils. Horizontal slinky heat exchangers consist out of coiled piping connected in series with a specified overlap called the loop pitch. The schematic of a possible horizontal slinky heat exchanger configuration is displayed in Figure 2a below. This interesting configuration minimises the required surface area to be dug up and is often placed around the outer edges of properties, with minimally invasive installation procedures. This geothermal ground source heat exchanger configuration is also modelled as part of the framework of this thesis.

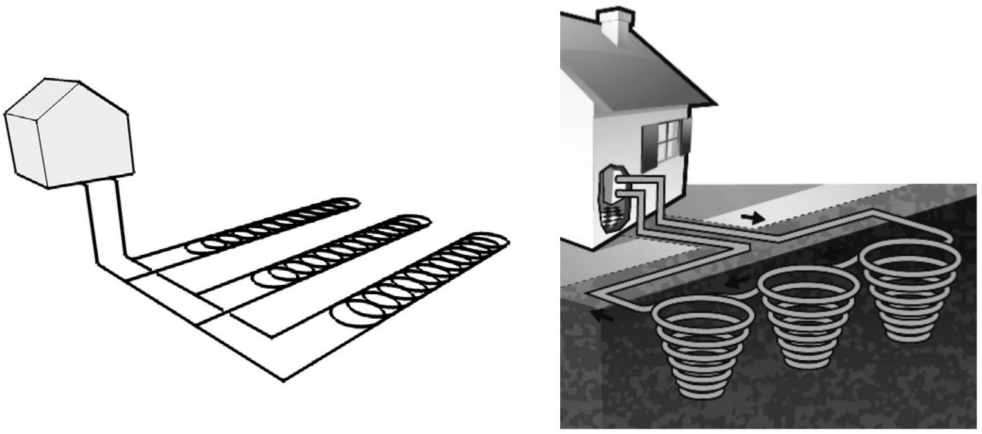

(a) Horizontal Slinky [2]

(b) Earth Baskets [3]

Figure 2: Schematic representation of horizontal slinky and earth basket heat exchangers.

[2]Reprinted from Xiong, Z., Fisher, D. E., & Spitler, J. D. (2015). Development and validation of a slinky^{TM} ground heat exchanger model. *Applied Energy*, *141*, 57–69. https://doi.org/10.1016/j.apenergy.2014.11.058, p. 58

[3]Reprinted from Manzella, A. (2015). Geothermal energy [Publisher: EDP Sciences]. *EPJ Web of Conferences*, *98*(4004), 22. https://doi.org/10.1051/epjconf/20159804004, p. 7

3.2.3 Earth Baskets

An attractive and cost-efficient alternative to vertical borehole heat exchangers and horizontal ground source heat exchangers is a vertical helix heat exchanger. These helical shaped baskets are commonly known as earth baskets and will be referred to as earth baskets throughout this thesis. Earth baskets consist of a heat exchanging loop, which is buried at a shallow depth in the ground, forming a cylindrical or a truncated cone helix, as shown in Figure 2b above (Conti, 2018). The advantages of using earth baskets as opposed to vertical boreholes, is that they have significantly less installation costs due to trench excavation being considerably less expensive than drilling vertical boreholes (Xiong et al., 2015). In comparison to horizontal ground source heat exchangers, earth baskets require significantly less land surface area for installation. Therefore, one can argue that earth baskets boast a hybrid cost effective alternative, whereby they mitigate costs such as drilling and materials in addition to requiring less land surface area. For geothermal building retrofitting in densely populated areas, where underground city infrastructure makes the drilling of numerous borehole heat exchangers economically unviable and the surface space required for extensive horizontal heat exchangers is sparse, the earth basket's advantages make this type of ground source heat exchanger highly interesting for the *GEOFIT* research project.

4 Principles of Heat Transport

Wetzel and von Böckh (2012) define the essence of heat transport as the following: "Heat transfer is the transport of thermal energy, due to a spacial temperature difference" (p. 1). The second law of thermodynamics describes the direction of heat transfer, whereby heat always flows spontaneously from a hotter region to a colder region. As Al-Khoury (2011) explains, this heat flow between two regions posing a spacial temperature difference will continue until both regions reach thermal equilibrium or "steady-state" conditions. In this state they both possess the same temperature and no further change in temperature over time is recorded. The temperature gradient over time is thus zero: $\frac{\partial T}{\partial t} = 0$. If the observed system's heat flow has not reached steady-state conditions yet and is in the "transient" state, the change in temperature recorded over the change in time is equal to a function f depending on the time t: $\frac{\partial T}{\partial t} = f(t)$. Heat may be transferred in three different ways called modes, namely thermal conduction, convection and radiation. These three heat transfer modes are graphically depicted in Figure 3 below.

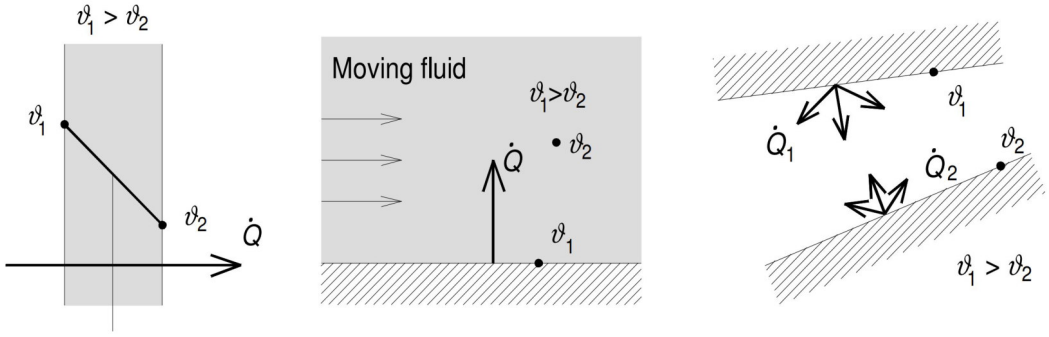

(a) Conduction (b) Convection / Advection (c) Radiation

Figure 3: Modes of heat transfer. [1]

4.1 Thermal Conduction

Figure 3a above visualises the process of heat transfer through a solid medium. This mode is called thermal conduction and is also sometimes referred to as heat diffusion (Al-Khoury, 2011). In solid materials or static fluids thermal conduction occurs when a spatial temperature gradient is present, as indicated with the higher temperature ϑ_1 and lower temperature ϑ_2 in Figure 3a above. Heat is transferred from the solid's hot surface through the body to its cold surface. On a microscopic level, heat is transferred through collisions of adjacent molecules or atoms. An increase in temperature coincides with an energy increase of molecules and atoms, which in return causes them to move or vibrate faster resulting in more frequent collisions with neighbouring molecules or atoms. This transfer in kinetic energy is called heat conduction and

[1] Reprinted from Wetzel, T., & von Böckh, P. (2012). *Heat transfer: Basics and practice*. Berlin, Heidelberg, Springer. https://doi.org/10.1007/978-3-642-19183-1, p. 3

thus thermal energy can be seen as a form of kinetic energy. Therefore thermal conduction is the dominant mode of heat transfer in solids and static fluids, where molecules and atoms are packed closely together (Al-Khoury, 2011). As Al-Khoury (2011) states, on a macroscopic level thermal conduction is described by the heat flux, defined as the heat transfer rate per unit area normal to the direction of heat flow. This heat flux is defined by *Fourier's* law of heat conduction and takes the following form for one-dimensional heat conduction as depicted in Eq. (1) below (Al-Khoury, 2011):

$$q_x = -\lambda_x \cdot \frac{\partial T}{\partial x} \tag{1}$$

This law is the governing principle behind heat transport in the heat exchanger models created as part of the framework of this thesis. *Fourier's* law of heat conduction in Eq. (5) and the heat conduction or diffusion equation will be discussed in further detail during the calculation of a geometrically simplified model's analytical solution in the following chapter.

4.2 Thermal Convection

As Wetzel and von Böckh (2012) explain, heat transfer is differentiated between solids or static fluids and fluids in motion. Heat transfer within a fluid in motion is called convective heat transfer or thermal convection. In Figure 3b above, heat transport between a solid wall and a moving fluid is visualised. The solid wall has a higher temperature ϑ_1 than the fluid in contact with the wall ϑ_2. This results in heat being transported from the static wall to the fluid in motion. Wetzel and von Böckh (2012) explain, that this heat transport occurs through two modes, firstly through thermal conduction between the solid wall and the fluid's static boundary layer which is in contact with the wall and secondly, through convective heat transport within the fluid. Once heat has been transferred through thermal conduction to the static fluid molecules in the boundary layer, these molecules expand due to the experienced increase in temperature. Expanded molecules with a higher temperature have a lower density than the surrounding colder molecules and begin to rise within the static fluid. The heat transported through this diffusion of molecules with higher temperature and lower density is called free convection. A further differentiation is made between free convection and forced convection, also referred to as advection. While during free convection the fluid's motion is created by gravity due to the molecule's difference in density caused by a spatial temperature gradient, during forced convection or advection, the fluid flow is created by an external pressure gradient (Wetzel & von Böckh, 2012). This is displayed in Figure 3b above. Al-Khoury (2011) states, that on a microscopic scale thermal convection is caused by thermal diffusion, while on a macroscopic scale heat is being transported through the resulting bulk fluid motion. This combination between diffusion and advection can also be recognised in the convective heat flux, which is displayed in its one-dimensional form in Eq. (2) below (Al-Khoury, 2011):

$$q_x = -\lambda_x \cdot \frac{\partial T}{\partial x} + \rho \cdot c_p \cdot u_x \cdot T \tag{2}$$

In Eq. (2) above, the first term with the thermal conductivity in x-direction λ_x is the diffusive term, while the latter term with the material properties like density ρ and specific heat capacity c_p and the fluid's velocity in x-direction u_x is called the advective term. Al-Khoury (2011) further elaborates, that convective heat transports from a boundary surface of temperature ϑ_1 that is exposed to a low velocity fluid of temperature ϑ_2, as it is depicted in Figure 3b above, may be described by *Newton's law of cooling*:

$$q = h \cdot (\vartheta_1 - \vartheta_2) \tag{3}$$

Whereby h in Eq. (3) above is the convective heat transfer coefficient.

4.3 Thermal Radiation

The third and last possible mode of heat transport is thermal radiation. Wetzel and von Böckh (2012) explain, that all matter which consists out of more than two atoms per molecule and possesses a finite temperature, will emit energy in the from of electromagnetic waves. This means that thermal radiation is the only form of heat transport that can occur without contact or the existence of an intervening medium (Wetzel & von Böckh, 2012). This is displayed in Figure 3c above, whereby two solid bodies with different temperatures ϑ_1 and ϑ_2 are separated by a vacuum. Both bodies will emit and absorb a heat flux, yet the emission of the body with the higher temperature ϑ_1 has a higher intensity (Wetzel & von Böckh, 2012). Thus, according to Wetzel and von Böckh (2012), thermal radiation can be defined as the result of the exchange of electromagnetic waves between two surfaces with differing temperature. This is formulated by *Stefan Boltzmann's* law. In reality, heat transport occurs as a combination of all three heat transfer modes that contribute to the total transferred heat with significantly different proportions. Al-Khoury (2011) agrees, that for the purpose of investigating heat flow in the vicinity of shallow geothermal heat exchangers, heat transfer through thermal radiation has a negligible effect and is therefore not further discussed in this thesis.

5 Analytical Solution

In order to display and verify the physical concepts behind the numeric *ANSYS Fluent* solver, a hand-calculated analytical solution and the numerically solved solution of a simplified heat conduction model are compared in the following chapter.

5.1 Rod Model Description

As shown below in Figure 4, a thin rod has been chosen as the heat conductive body of the model, so that the one-dimensional heat conduction can be accurately evaluated along the centred x-axis of the rod model. The rod is 1 metre long and 0.01 metres deep and high. The rod possesses uniform material properties, whereby the density, thermal conductivity and specific heat capacity are all set to a value of 1 in their respective SI units. The temperature on the left and right boundary of the model, as well as the initial temperature throughout the rod is set to a constant value of 0 Kelvin. It is important to mention, that the boundary temperature and material property values of the rod model do not attempt to represent real-life applicable problems. They were chosen as values of 1 and 0 respectively, to make a calculation of the analytical solution possible, by reducing the mathematical complexity. A time-independent heat source $Q(x)$, with a quarter of the amplitude used in the analytical calculation $\left(\frac{A}{4}\right)$, is applied to each of the four remaining boundaries. As one can see on the right-end boundary in Figure 4, the mesh has a resolution of $(1\,000|10|10)$ cells along the respective axes, which adds up to a total of $100\,000$ uniform cubic cells with a cell size of 10^{-9} m^3.

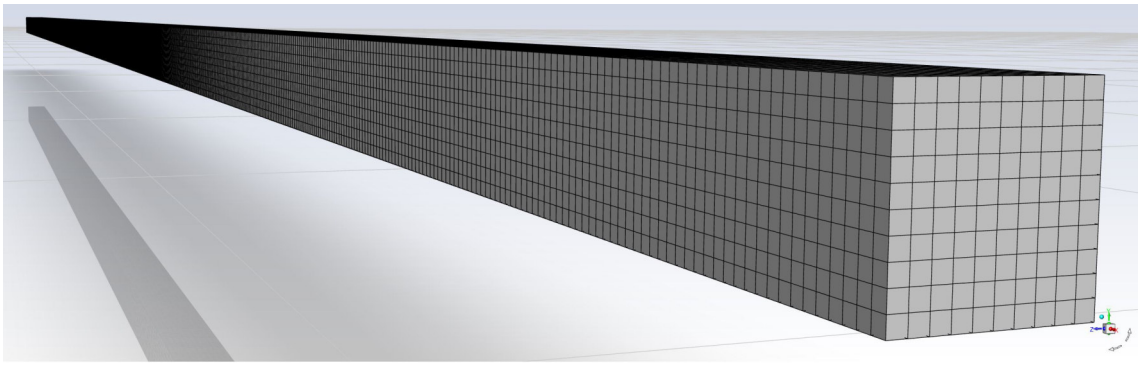

Figure 4: Rod model with a resolution of $100\,000$ cells.

5.1.1 Mesh Independence

Before the numerical solutions of the model can be compared to the analytical solutions, their accuracy needs to be verified. Even though the residuals have converged to an acceptable low value and the steady state has been reached, the effect of the model's mesh resolution on the numerical solution cannot be neglected yet. Therefore, for every new mesh type, a mesh

independence study has to be conducted. This is done by increasing and decreasing the cell numbers of the mesh, or in other words the mesh resolution. The solutions of these varying mesh resolutions are then compared. Some of the mesh sizes compared to the regular model with a mesh size of $100\,000$ cells were $211\,250$ cells, $53\,311$ cells, $32\,683$ cells and lastly $12\,500$ cells. Due to the small size and uniform shape of the model there are almost no detectable differences between the solutions with varying mesh resolution. Therefore the solution is deemed "mesh independent" and we may proceed with the analysis and comparison of the model's solution.

5.2 The One-Dimensional Heat Conduction Equation

In this section the governing physical principles behind the heat transfer through the rod model from the previous section are examined.

A body with a non-uniform temperature distribution, like a rod with a heat source is considered. The second law of thermodynamics states, that heat or thermal energy is transferred from regions of higher temperature to regions of lower temperature. According to Widder (1976), the following three physical principles describe this transfer of thermal energy within a solid body: Absorption, Conduction and Conservation of Energy.

If a body consists out of a uniform material, then the amount of increase in heat quantity ΔQ is directly proportional to the mass m of the body and to the increase in temperature ΔT: [1]

$$\Delta Q = c_p \cdot m \cdot \Delta T \tag{4}$$

The constant of proportionality c_p from Eq. (4) is dependent on the material of the body and is called the specific heat capacity of the material at constant pressure. It is defined as the energy required to raise a unit mass of the material by one unit of temperature, while the pressure remains constant (Hancock, 2006).

In 1822, Joseph Fourier first formulated what is known today as Fourier's law of thermal conduction: "The heat flux resulting from thermal conduction is proportional to the magnitude of the temperature gradient and opposite to it in sign" (Connor, 2019, p. 1). Hancock (2006) simplifies this formulation by stating, that heat is transferred from areas of higher temperature to areas of lower temperature.

$$\vec{q} = -\vec{\lambda} \cdot \nabla T \tag{5}$$

The proportionality constant from Eq. (5) above is known as the thermal conductivity $\vec{\lambda}$. For three-dimensional heat conduction $\vec{\lambda}$ is a vector representing the varying thermal conductivity of the heat conducting medium in multiple dimensions, while ∇ is the gradient operator. The heat flux $\vec{q}$ is defined as the rate of heat transfer per unit area normal to the direction of the

[1] Widder, D. V. (1976). *The heat equation* (Vol. 76). Academic Press, p. 2

heat transfer. As the heat flux possesses a magnitude as well as a direction, it is defined as a vector field for heat conduction in multiple dimensions.

Now, similarly to the previously mentioned rod model, a uniform long rod with a length l and a non-uniform heat distribution is considered. Uniform in this case means, that material and geometric properties like density ρ, specific heat capacity c, thermal conductivity λ and cross-sectional area A all remain constant throughout the rod. Additionally, the rod may be designated as long, as its length in x-axis direction is multiple factors larger than it's width in the y and z-axes. Therefore, the heat conduction within the rod may be described as one-dimensional heat conduction in x-direction. Once the material properties and geometry of the rod are defined, an arbitrary thin slice with the width Δx between x and $x + \Delta x$ is chosen (Hancock, 2006). According to Showalter (2013), the amount of heat stored in a section $[x, x + \Delta x]$ of the rod, with $\Delta x > 0$ is given by Eq. (6) below:

$$Q(\Delta x) = \int_x^{x+\Delta x} \rho\, c_p\, A\, T(s,t)\, ds \tag{6}$$

Applying the law of conservation of energy, the rate at which heat is stored within the section of the rod is equal to the sum of the rate of heat that flows in and out of the section and the the rate at which heat is generated in the section (Showalter, 2013).

$$\frac{\partial}{\partial t} \int_x^{x+\Delta x} \rho\, c_p\, A\, T(s,t)\, ds = A\,(q(x,t) - q(x+\Delta x, t)) + \int_x^{x+\Delta x} A\, Q(s)\, ds \tag{7}$$

The term $Q(s)$ from Eq. (7) is the heat generation or source term and is the heat generated within the slice per unit volume. This source term may be dependent on time and position. However, for simplification of the analytical solution, the term used in the model is time-independent and will be further defined in the next section.

According to Showalter (2013), dividing Eq. (7) by $A\Delta x$ while letting $\Delta x \to 0$, yields the following conservation of energy equation:

$$\rho\, c_p\, \frac{\partial T}{\partial t}(x,t) + \frac{\partial q}{\partial x}(x,t) = Q(x) \tag{8}$$

Lastly, Showalter (2013) substitutes Fourier's law of thermal conduction from Eq. (5) into the energy conservation law from Eq. (8) above:

$$\rho\, c_p\, \frac{\partial T}{\partial t}(x,t) - \frac{\partial}{\partial x}\left(\lambda\, \frac{\partial T}{\partial x}(x,t)\right) = Q(x) \tag{9}$$

This is the one-dimensional heat conduction equation, also known as the diffusion equation and can be re-written into following compact form:

$$\frac{\partial T}{\partial t}(x,t) - \alpha\, \frac{\partial^2 T}{\partial x^2}(x,t) = \frac{1}{\rho\, c_p}\, Q(x) \tag{10}$$

Whereby $\alpha = \frac{\lambda}{\rho\, c_p}$ from Eq. (10) is the thermal diffusivity of the material. Showalter (2013)

defines the thermal diffusivity as a measure of the material's rate of change in temperature.

Subsequently, the basic form of the one-dimensional heat equation without a heat source is the following (Widder, 1976):

$$\frac{\partial T}{\partial t} = \alpha \frac{\partial^2 T}{\partial x^2} \tag{11}$$

According to Widder (1976), Eq. (11) can be generalised for heat conduction in uniform materials to higher dimensions accordingly:

$$\rho\, c_p \frac{\partial T}{\partial t} = \lambda_1 \frac{\partial^2 T}{\partial x_1^2} + \lambda_2 \frac{\partial^2 T}{\partial x_2^2} + ... + \lambda_n \frac{\partial^2 T}{\partial x_n^2} \tag{12}$$

5.2.1 Defining a Time-Independent Source Term

Taking a closer look at the one-dimensional heat conduction equation from Eq. (11), the temperature T is a function of the position x and time t, while α is the thermal diffusivity. As explained previously, the thermal diffusivity can be re-written as a fraction of the thermal conductivity λ , the density ρ and the specific heat capacity at constant pressure c_p. Furthermore, a time-independent heat source $Q(x)$ is added into the model:

$$\rho\, c_p \frac{\partial T}{\partial t} = \lambda \frac{\partial^2 T}{\partial x^2} + Q(x) \tag{13}$$

This source term $Q(x)$ in W m^{-3} from Eq. (13) may be an arbitrary function of the position x, defined over the length L of the model. For the verification of the model, a Gaussian function with an amplitude A at the position ξ was chosen as a source term. A Gaussian function was chosen, as it finds many applications in descriptions of natural processes who's entropy is maximised. Additionally, its asymptotic shape does not drastically interfere with the fixed boundary conditions on either side of the rod.

$$Q(x) = A\, e^{-\sigma(x-\xi)^2} \tag{14}$$

Whereby σ describes the width of the bell curve. Substituting Eq. (14) into Eq. (13) results in:

$$\rho\, c_p \frac{\partial T}{\partial t} = \lambda \frac{\partial^2 T}{\partial x^2} + A\, e^{-\sigma(x-\xi)^2} \tag{15}$$

Now the one-dimensional heat equation with a given source term can be solved.

5.3 Steady-State Solution

In order to solve Eq. (15), the time-independent solution has to be considered first. Hereby, the time-dependent term on the left-hand side disappears and the equation is rearranged as

follows:

$$\frac{\partial^2 T}{\partial x^2} = -\frac{A}{\lambda}\, e^{-\sigma(x-\xi)^2} \tag{16}$$

By integrating the time-independent Eq. (16) after the position twice, a general steady-state solution $T^*(x)$ of the one-dimensional heat equation with a time-independent source term is achieved.

$$T^*(x) = -\frac{A}{\lambda} \iint_x e^{-\sigma(s-\xi)^2}\, ds\, dx + C_1 x + C_2 \tag{17}$$

Through integrating after the additional position variable s through substitution (see Appendix A), the equation below follows, whereby the Gauss error function is denoted as erf :

$$T^*(x) = -\frac{A}{2\lambda}\sqrt{\frac{\pi}{\sigma}} \int \mathrm{erf}\left(\sqrt{\sigma}(x-\xi)\right) dx + C_1 x + C_2 \tag{18}$$

By further integrating through substitution after the location x (see Appendix A), the general steady-state solution for the heat equation is the following:

$$T^*(x) = -\frac{A}{2\lambda\sigma}\left[\sqrt{\pi\sigma}\,(x-\xi)\,\mathrm{erf}\left(\sqrt{\sigma}(x-\xi)\right) + e^{-\sigma(x-\xi)^2}\right] + C_1 x + C_2 \tag{19}$$

Analysing the units from Eq. (19), the steady-state solution $T^*(x)$ is a temperature in Kelvin, if the source term $Q(x)$ is given in $\mathrm{W\,m^{-3}}$ and the heat conductivity λ in its International System of Units (SI) $\mathrm{W\,m^{-1}\,K^{-1}}$. The integration constants C_1 and C_2 will be defined through the boundary conditions of the model:

$$T^*(0) = T^*(L) = 0 \tag{20}$$

The first boundary condition $T^*(x=0) = 0$ leads to the following expression for the integration constant C_2:

$$C_2 = \frac{A}{2\lambda\sigma}\left[\sqrt{\pi\sigma}\xi\,\mathrm{erf}\left(\sqrt{\sigma}\xi\right) + e^{-\sigma\xi^2}\right] \tag{21}$$

Subsequently, the second boundary condition $T^*(x=L) = 0$ leads to an expression for the integration constant C_1:

$$C_1 = \frac{A}{2\lambda\sigma L}\left[\sqrt{\pi\sigma}\left[(L-\xi)\,\mathrm{erf}\left(\sqrt{\sigma}\,(L-\xi)\right) - \xi\,\mathrm{erf}\left(\sqrt{\sigma}\xi\right)\right] + e^{-\sigma(L-\xi)^2} - e^{-\sigma\xi^2}\right] \tag{22}$$

Substituting the integration constants back into Eq. (19) leads to the general steady-state solution of the one-dimensional heat equation for a model with Dirichlet boundary conditions from Eq. (20) and a source term from Eq. (14).

$$\begin{aligned} T^*(x) = &-\frac{A}{2\lambda\sigma}\left[\sqrt{\pi\sigma}\,(x-\xi)\,\mathrm{erf}\left(\sqrt{\sigma}(x-\xi)\right) + e^{-\sigma(x-\xi)^2}\right] \\ &+ \frac{A}{2\lambda\sigma}\left[\sqrt{\pi\sigma}\left[(L-\xi)\,\mathrm{erf}\left(\sqrt{\sigma}\,(L-\xi)\right) - \xi\,\mathrm{erf}\left(\sqrt{\sigma}\xi\right)\right] + e^{-\sigma(L-\xi)^2} - e^{-\sigma\xi^2}\right]\frac{x}{L} \\ &+ \frac{A}{2\lambda\sigma}\left[\sqrt{\pi\sigma}\xi\,\mathrm{erf}\left(\sqrt{\sigma}\xi\right) + e^{-\sigma\xi^2}\right] \end{aligned} \tag{23}$$

In the following section the analytical solution is compared to the numerical solution of the model for multiple source terms along the entire length of the model.

5.3.1 Steady-State Solution Comparison

In the following section, the analytical steady-state solution from Eq. (23) above will be compared to the *ANSYS Fluent* solver's numerical steady-state solution. Furthermore, the match between the two solutions for varying amplitudes, bell widths and maximum positions of the heat source function will be analysed.

As shown below in Figure 5, a centred Gaussian heat source function from Eq. (13) with an amplitude $A = 6000$ W m^{-3}, a bell width $\sigma = 50$ m^{-2} and a maximum at the centre of the rod $\xi = \frac{L}{2} = 0.5$ m is used to compare the analytical and numerical solutions. Therefore, Eq. (13) takes the following form:

$$Q(x) = 6000\, e^{-50\,(x-0{,}5)^2} \quad (\mathrm{W\,m^{-3}}) \tag{24}$$

Taking the small volume of the rod model into consideration, this leads to a total heat input of $Q = 0.15$ W into the rod.

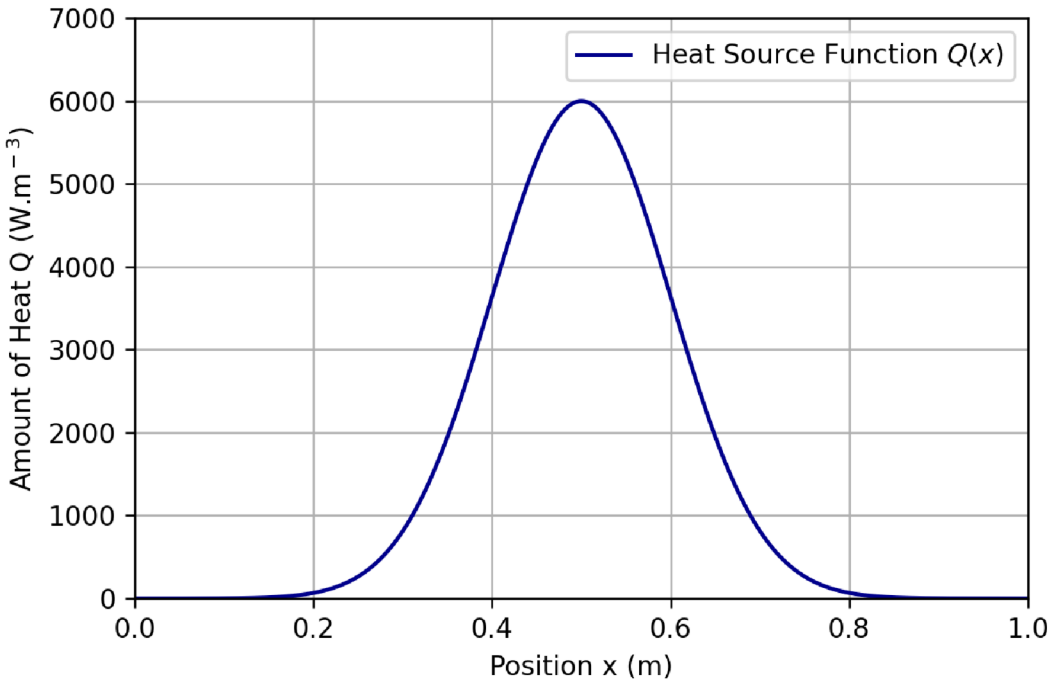

Figure 5: Heat Source Function $Q(x)$ along the length of the rod model.

Now, the analytical solution, calculated with the source function from Eq. (24) is compared to the solver's numeric solution. The graph in Figure 6 below shows the absolute temper-

ature difference between the two solutions, whereby the numerically calculated values were subtracted from the analytically calculated solution.

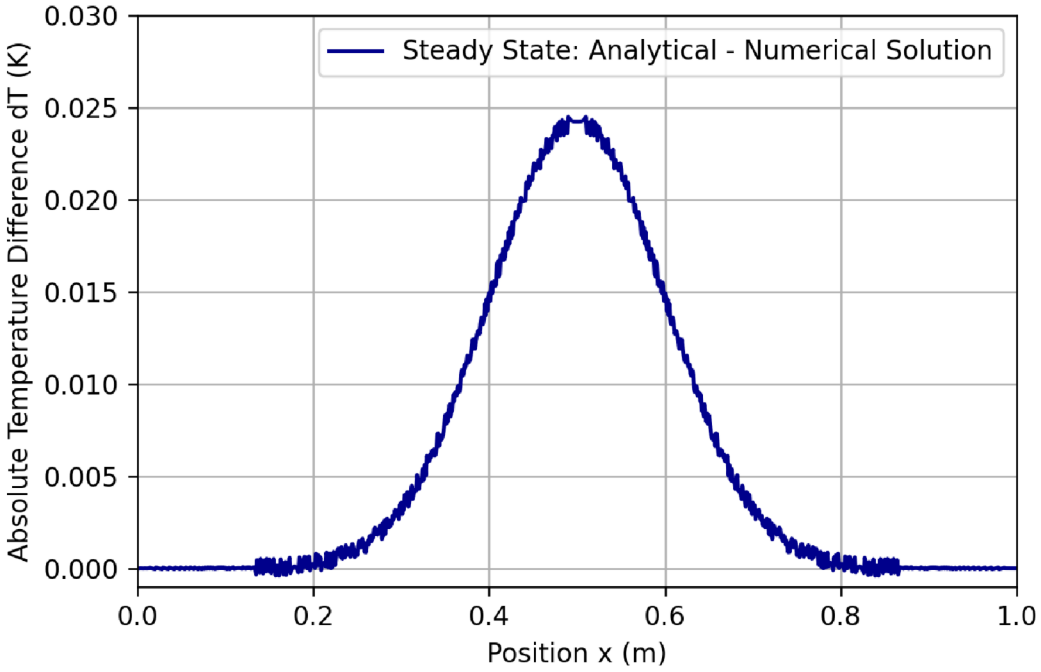

Figure 6: Analytical and numerical solution steady-state absolute temperature difference.

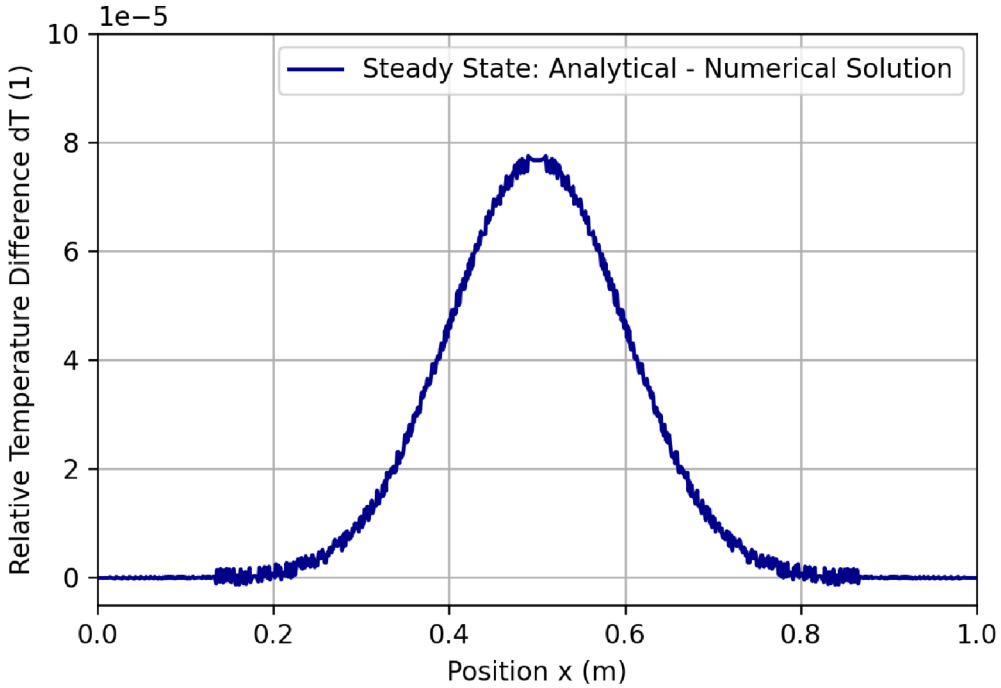

Figure 7: Analytical and numerical solution steady-state relative temperature difference.

Therefore, a purely positive temperature difference indicates that the analytically calculated solution seems to be slightly higher than the numerically calculated solution. Interestingly, the error increases with increased heat input and seems to proportionally follow the heat input function along the x-axis of the rod. A small negligible tremor of the steady-state error is visible in Figure 6 and 7 above. Since the absolute temperature difference from Figure 6 does not allow a qualitative analysis of the analytically calculated error's significance, the relative temperature difference between the two solutions has to be considered. In Figure 7 above, the absolute temperature difference has been scaled to the numerical solution's maximum temperature of $T^*(x = 0.5\,m) = 315.97$ K (see Figure 8 below). With all relative steady-state solution errors well under 0.01 percent, the error between the analytically and numerically calculated steady-state solution can be deemed as negligible.

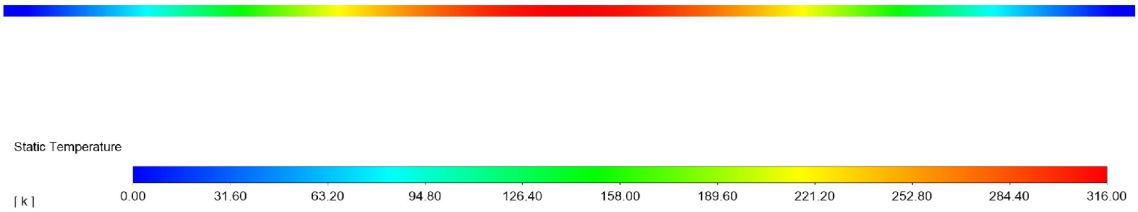

Figure 8: Steady-state temperature contour plot of the rod model's x-y plane.

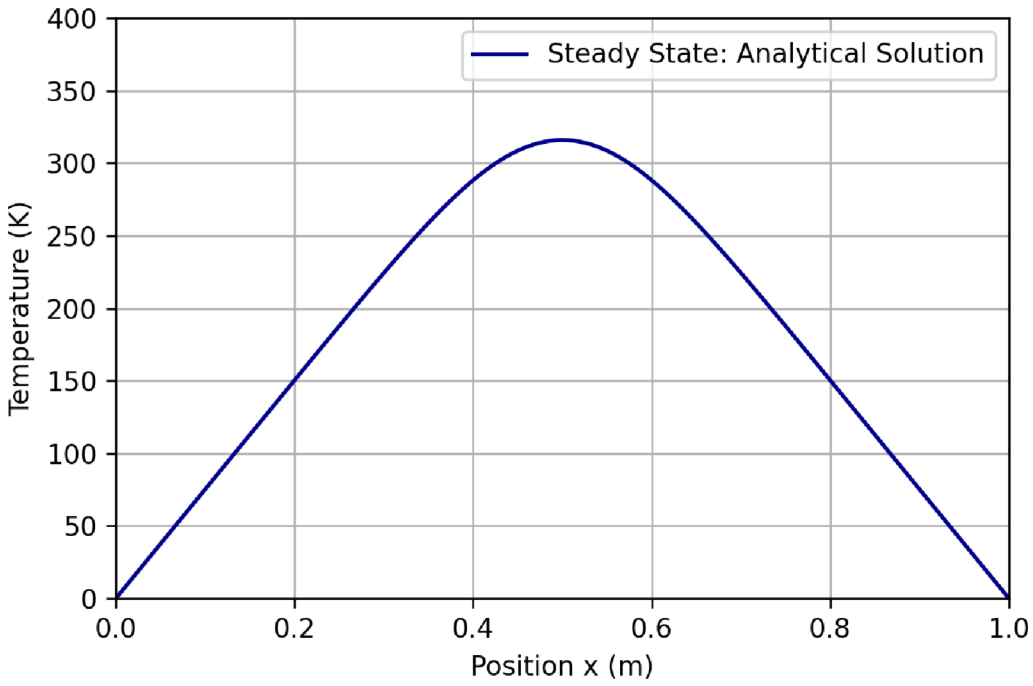

Figure 9: Analytically calculated steady-state temperature at the rod model's centre.

The numerical steady-state solution of the Fluent solver can be seen in the form of a contour plot in Figure 8 above. The boundary conditions of zero Kelvin on the left and right hand side of the rod and the implemented heat source distribution along the rod's x-axis can be observed in the contour plot. The corresponding analytically calculated absolute temperature distribution along the rod's x-axis is seen above in Figure 9.

Since the accuracy of the analytical solution for a specific source function has been verified, the accuracy of the solutions for varying amplitudes A, maximum positions ξ and bell curve widths σ will be studied in the following sections. While one parameter is altered, the other parameters are kept constant.

5.3.1.1 Heat Source Function Amplitude A Variation

The standard amplitude of $A = 6000\ \mathrm{W\,m^{-3}}$ used in the previous section in Eq. (24) has been doubled and halved and the absolute temperature difference between the analytically and numerically calculated solution is compared in Figure 10 below.

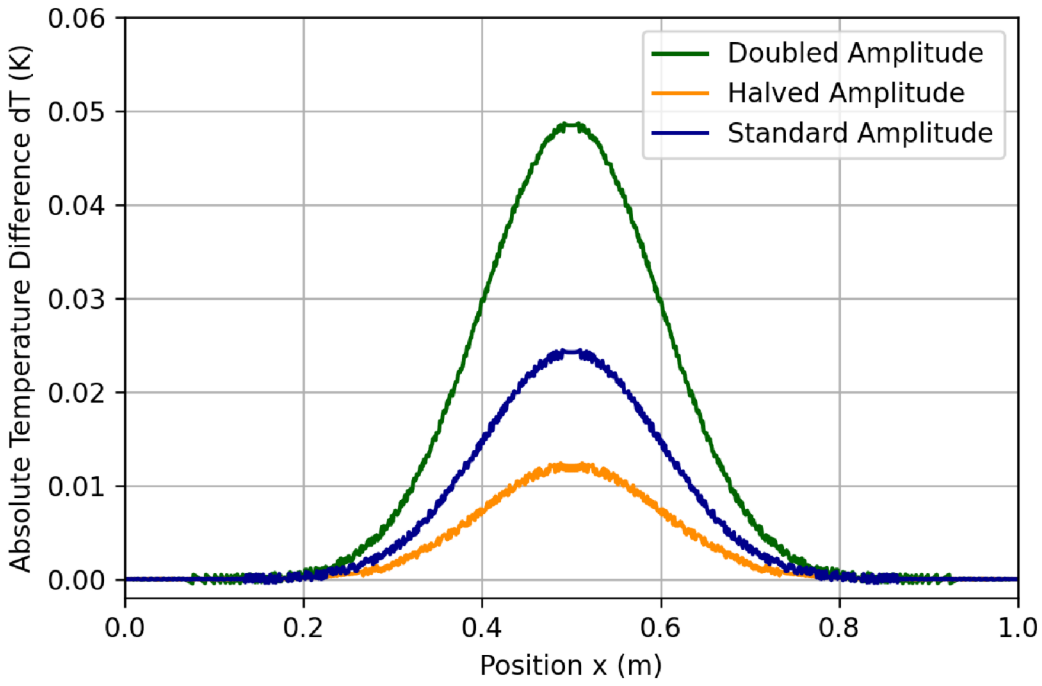

Figure 10: Absolute temperature difference of analytical and numerical solution: amplitude variation.

As expected, the absolute temperature difference increases and decreases proportionally with the amplitude variation. If the amplitude is doubled, the maximum achieved temperature at steady state is doubled as well and the absolute temperature difference between the numerical and analytical solution increases twofold. Analogically, the relative temperature difference between the two solutions does not vary with varying amplitudes. Except for the negligible

tremors, the relative temperature differences for varying amplitudes remain identical and well under 0.01 percent (see Figure 11 below). Thus, the solution's accuracy is not affected by reasonable variations of the amplitude's magnitude.

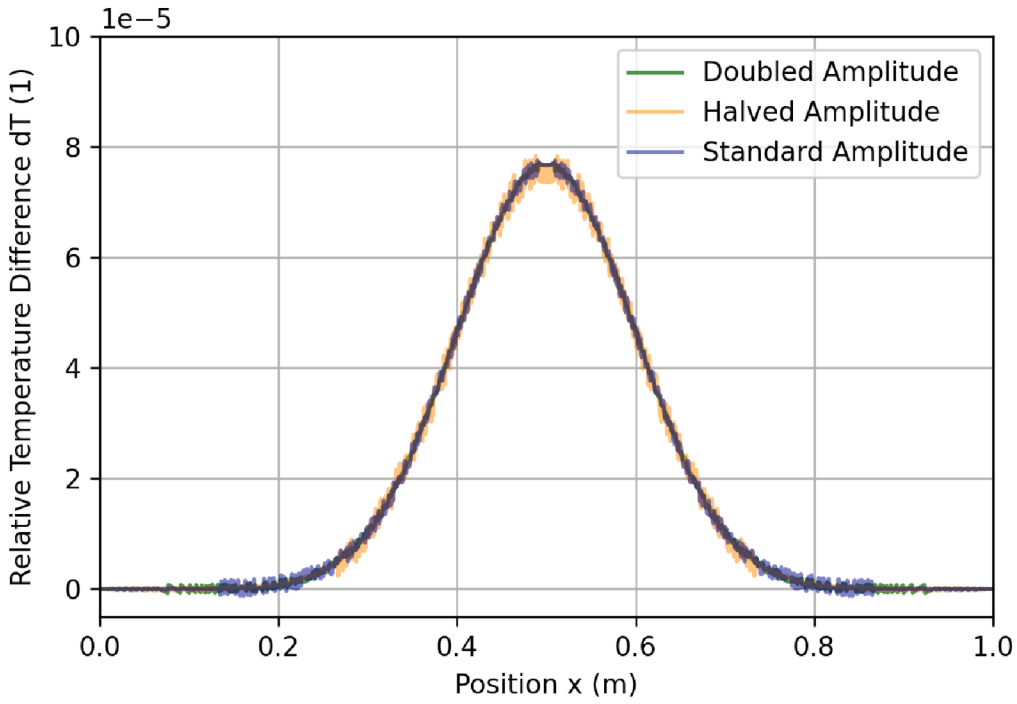

Figure 11: Relative temperature difference of analytical and numerical solution: amplitude variation.

5.3.1.2 Heat Source Function Bell Curve Width σ Variation

Now, the effect of the shape of the source function on the analytical solution's accuracy is studied. The amplitude and maximum position remain constant and centred, while the bell curve's width is altered. The standard bell curve width of $\sigma = 50\ \mathrm{m}^{-2}$ was chosen, so that the asymptotic Gaussian function reaches an insignificantly low value, before approaching the boundary condition of zero Kelvin on either side. Therefore, the bell curve width has been reduced by the factors three and twelve respectively and then compared to the standard width.

Figure 12 below visualises, that the absolute temperature difference between the analytical and numerical solution behaves analogical to the previous amplitude variation and changes proportionally with the heat source function's change in shape. If the amplitude is kept constant, a reduction in the source function's curve width coincides with a reduced total heat input, as the area under the source function decreases. Therefore, a reduction in the source function's curve width results in lower maximum temperatures reached at the rod's centre. While the absolute temperature difference of the two solutions depicted in Figure 12 is purely dependent on the heat source function's amplitude, the relative temperature difference is de-

pendent on the source function's curve width, due to the reduced maximum temperature at the rod's centre (see Figure 13 below).

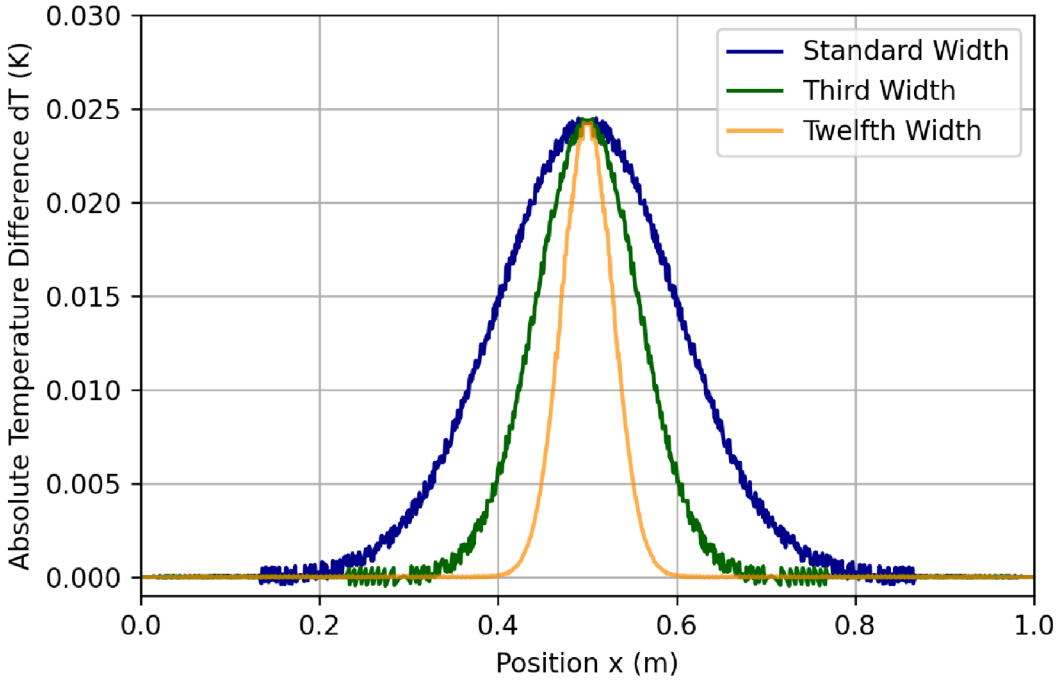

Figure 12: Absolute temperature difference of analytical and numerical solution: curve width variation.

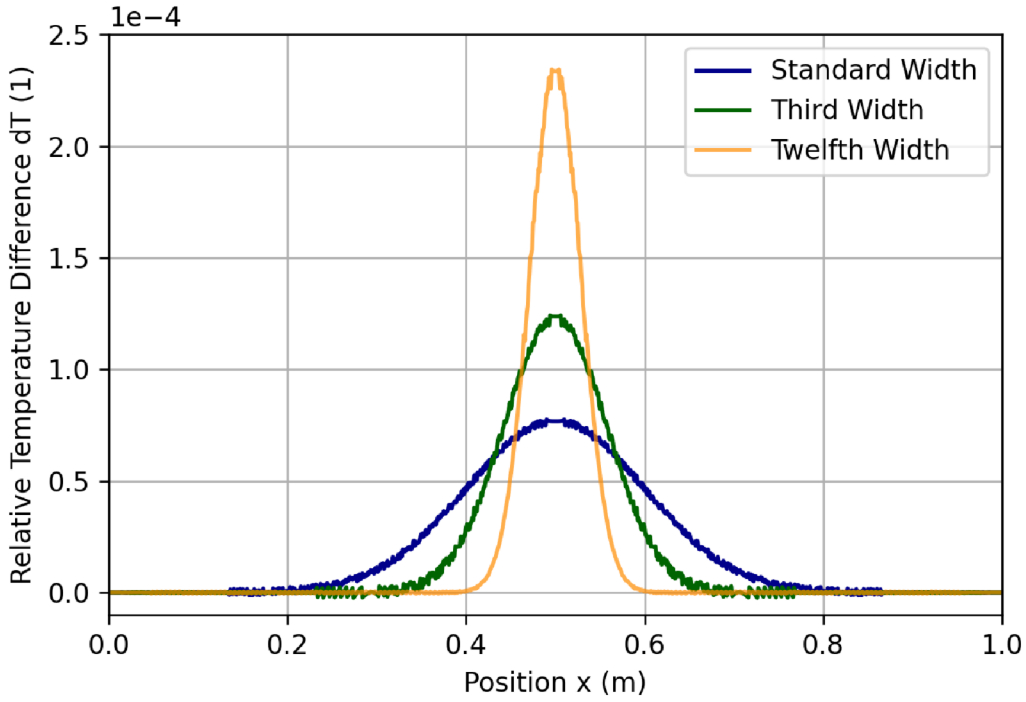

Figure 13: Relative temperature difference of analytical and numerical solution: curve width variation.

For a narrower heat source function, assuming a constant amplitude, the total heat input will be lower and the relative error of the analytical solution will rise, due to the lower maximum temperature. However, if the amplitude for a narrower heat source function would be increased, so that the total heat input remains the same, the maximum relative error would remain constant as well. For a low curve width, the relative error of the analytical solution in Figure 13 above is below 0.025 percent. Thus, the analytical solution still proves to be very accurate for extremely narrow source function shapes at low heat inputs.

5.3.1.3 Heat Source Function Maximum Position ξ Variation

The last variable of the implemented heat source function to be varied is the position of the function's maximum. In the standard model, the Gaussian function's maximum position is placed at the rod's centre at $\xi = \frac{L}{2} = 0.5$ m. This position is now altered and adjusted to a third $\left(\xi = \frac{L}{3}\right)$ and two-thirds $\left(\xi = \frac{2}{3}\,L\right)$ of the rod's length respectively. However, the source function's curve width is changed to a constant $\sigma = 150$ m^{-2}, so that the asymptotic Gaussian function still reaches a negligible low value, before approaching the boundary condition.

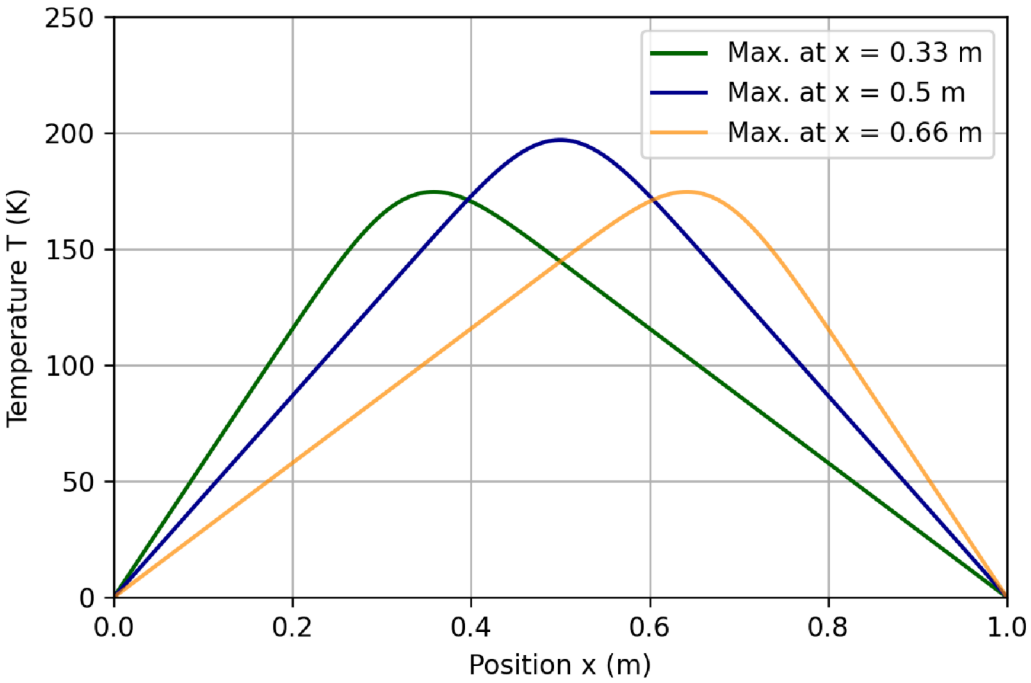

Figure 14: Numerical steady-state solutions with $\sigma = 150$ m^{-2} and varying maximum positions.

In Figure 14 above, the steady-state solutions with the heat source function's maximum positions at $x = 0.33$ m, $x = 0.5$ m and $x = 0.66$ m are visualised. The solution's total maximum temperature is lower than the standard model's maximum temperature, as the heat source function's curve width has been reduced to a constant $\sigma = 150$ m^{-2}. It can be observed, that if the maximum position is shifted closer the left and right boundary, then the maximum

temperature is reduced. This effect is expected, as the boundary conditions have a greater influence on the shifted maximum position and therefore dampen the temperature curve.

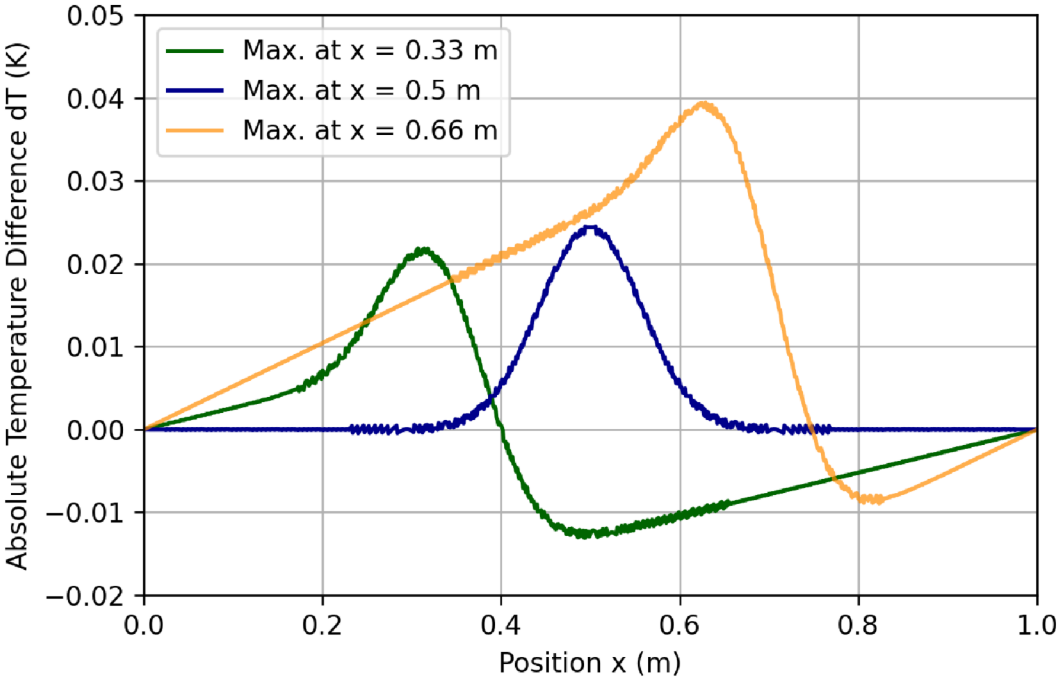

Figure 15: Absolute temperature difference for heat source function's maximum position variation.

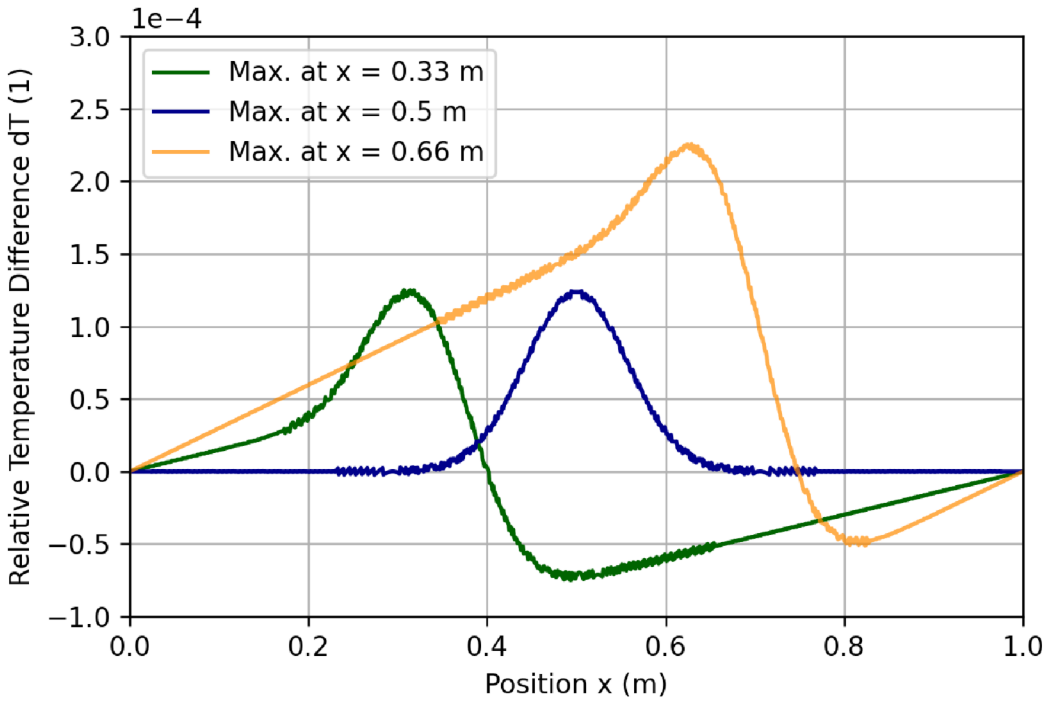

Figure 16: Relative temperature difference for heat source function's maximum position variation.

Interestingly, the temperature difference between the analytically and numerically calculated solutions from Figure 15 and 16 above display a change of sign at the heat function's respective maximum position. Furthermore, the absolute and relative temperature difference increases with increasing maximum position respective to the coordinate systems point of origin at $x = 0$ m. The temperature difference at the maximum position is almost doubled between the heat source function's maximum at $x = 0.33$ m and $x = 0.66$ m. This effect may hint to an interesting non-symmetrical way that the numeric solver approaches certain geometries. Yet, the relative temperature difference is still below 0.025 percent and therefore the solutions for the heat source function's maximum position variations can also be deemed as accurate.

5.4 Transient Solution

The steady-state solution is now no longer an unknown and can therefore be used to obtain the time-dependent solution of the heat equation from Eq. (15). According to Hancock (2006) the solution of the heat equation consists out of a transient part and a steady-state part.

$$T(x,t) = \tilde{T}(x,t) + T^*(x) \tag{25}$$

Whereby the steady-state term is denoted as $T^*(x)$, a function of the position x and the transient term is denoted as $\tilde{T}(x,t)$, a function of the position x and the time t. Equation (25) is then substituted into the heat equation with a heat source:

$$\frac{\partial T}{\partial t}(x,t) = \alpha \frac{\partial^2 T}{\partial x^2}(x,t) + Q(x) \tag{26}$$

Substituting Eq. (25) into Eq. (26) above, results in the following expression for $\tilde{T}(x,t)$:

$$\frac{\partial \tilde{T}}{\partial t}(x,t) = \alpha \frac{\partial^2 \tilde{T}}{\partial x^2}(x,t) \tag{27}$$

As $\frac{\partial^2 T^*}{\partial x^2}(x) = -Q(x)$, the source term is dropped in the Partial Differential Equation (PDE) and Eq. (27) satisfies the homogeneous heat equation. The same Dirichlet boundary conditions apply for the transient PDE:

$$\tilde{T}(0,t) = \tilde{T}(L,t) = 0 \quad \text{for } t > 0 \tag{28}$$

This homogeneous PDE can be solved by separation of variables. The homogeneous boundary conditions create a Sturm-Liouville problem. By applying the principle of superposition, a solution of the PDE from Eq. (27), which satisfies the boundary conditions from Eq. (28), is obtained. This is shown in detail in the upcoming sections and finally leads to a first expression of the transient solution in Eq. (52).

5.4.1 Separation of Variables

The Fourier method is used to solve the PDE from Eq. (27). After separating the variables, the dependence of the solution $\tilde{T}$ on x and t is expressed through the following product:

$$\tilde{T}(x,t) = F(x)\,G(t) \tag{29}$$

Therefore, the relevant partial derivatives are:

$$\frac{\partial \tilde{T}}{\partial t}(x,t) = F(x)\,G'(t) \;\wedge\; \frac{\partial^2 \tilde{T}}{\partial x^2}(x,t) = F''(x)\,G(t) \tag{30}$$

Whereby the primes denote the differentiation of a variable function. These are now inserted into Eq. (27) and rearranged, so that the corresponding variables are on the same side.

$$\frac{G'(t)}{\alpha\,G(t)} = \frac{F''(x)}{F(x)} \tag{31}$$

Now, the left hand side (l.h.s.) only depends on the time t and the right hand side (r.h.s.) only depends on the position x. Therefore, both sides must equal a constant, as shown by Eq. (32) below (Ganster, 2015, p. 5). This constant is called the separation constant and is set to $-\mu$ by convention.

$$\frac{G'(t)}{\alpha\,G(t)} = \frac{F''(x)}{F(x)} = -\mu \tag{32}$$

5.4.2 Solving for $F(x)$: A Sturm-Liouville Eigenvalue Problem

From Eq. (32) we obtain the following two homogeneous Ordinary Differential Equations (ODEs):

$$G'(t) + \alpha\,\mu\,G(t) = 0 \tag{33}$$

$$F''(x) + \mu\,F(x) = 0 \tag{34}$$

The same Dirichlet boundary conditions from Eq. (28) still apply for Eq. (34) and can be re-written as follows:

$$\tilde{T}(0,t) = F(0)\,G(t) = 0 \quad \text{for } t > 0 \tag{35}$$

$$\tilde{T}(L,t) = F(L)\,G(t) = 0 \quad \text{for } t > 0 \tag{36}$$

As Ganster (2015) explains, $G(t)$ is not the zero function and therefore the boundary condition can be simplified to:

$$F(0) = F(L) = 0 \tag{37}$$

With the boundary condition from Eq. (37), the ODEs from Eq. (33) and (34) can be solved. For the ODE $F''(x) + \mu\,F(x) = 0$ the mathematical approach $F(x) = e^{kx}$ is chosen, which

delivers the auxiliary equation $k^2 + \mu = 0$ (Ganster, 2015; see also Hancock, 2006). This boundary value problem is called a Sturm-Liouville Eigenvalue problem, for which three different cases have to be considered: $\mu < 0$, $\mu = 0$ and $\mu > 0$.

5.4.2.1 First Case: $\mu < 0$

For the first case $\mu < 0$ is assumed. Therefore, for all $\mu < 0$, the expression $k_{1,2} = \pm\sqrt{\mu}$ is obtained from the auxiliary equation $k^2 + \mu = 0$. According to Ganster (2015), the solution to Eq. (34) is the following:

$$F(x) = a\, e^{\sqrt{\mu}x} + b\, e^{-\sqrt{\mu}x} \tag{38}$$

The constants a and b can be obtained by inserting the boundary conditions from Eq. (37):

$$\begin{aligned} F(0) = 0 \quad &\Rightarrow \quad a + b = 0 \\ \wedge\, F(L) = 0 \quad &\Rightarrow \quad a\, e^{\sqrt{\mu}L} + b\, e^{-\sqrt{\mu}L} = 0 \end{aligned} \tag{39}$$

From this, the solution for a, b and $F(x)$ can be derived:

$$a = b = 0 \quad \Rightarrow \quad F(x) \equiv 0 \tag{40}$$

$F(x) \equiv 0$ is the trivial solution and thus, the first case is discarded.

5.4.2.2 Second Case: $\mu = 0$

For the second case $\mu = 0$ is assumed. As Ganster (2015) shows, inserted into the auxiliary equation from above this leads to $k_{1,2} = 0$ and the following solution for $F(x)$ is obtained:

$$F(x) = a + b\, x \tag{41}$$

Inserting the boundary conditions from Eq. (37) again, the solution for a, b and $F(x)$ is the following:

$$\begin{aligned} F(0) = 0 \quad &\Rightarrow \quad a = 0 \\ \wedge\, F(L) = 0 \quad &\Rightarrow \quad a + b\, L = 0 \\ \Rightarrow \quad a = b = 0 \quad &\Rightarrow \quad F(x) \equiv 0 \end{aligned} \tag{42}$$

Again, $F(x) \equiv 0$ is a trivial solution and thus, the second case is discarded as well.

5.4.2.3 Third Case: $\mu > 0$

In the third and last case, the separation constant is set to $\mu > 0$. Now, the expression $k_{1,2} = \pm\sqrt{-\mu}$ for all $\mu > 0$ is obtained from the auxiliary equation $k^2 + \mu = 0$. The solution

for k can be re-written as follows: $k_{1,2} = \pm i\sqrt{\mu}$, whereby i is the imaginary unit. As Ganster (2015) and Hancock (2006) explain, for $\mu > 0$ Eq. (34) is the simple harmonic equation with a general solution for $F(x)$ in the following form:

$$F(x) = a\cos(\sqrt{\mu}\,x) + b\sin(\sqrt{\mu}\,x) \tag{43}$$

Now, the boundary conditions from Eq. (37) are used again to obtain a solution for a, b and $F(x)$:

$$\begin{aligned} F(0) = 0 \quad &\Rightarrow \quad a = 0 \\ \wedge\, F(L) = 0 \quad &\Rightarrow \quad a\cos(\sqrt{\mu}\,L) + b\sin(\sqrt{\mu}\,L) = 0 \\ &\Rightarrow \quad b\sin(\sqrt{\mu}\,L) = 0 \end{aligned} \tag{44}$$

The solution to b in the term $b\sin(\sqrt{\mu}L) = 0$ can be split into two cases again. Firstly, simply setting $b = 0$ provides a solution. However, this would lead to the trivial solution of $F(x) \equiv 0$ again and is therefore discarded. Thus, only for $b \neq 0$ a non-trivial solution is obtained.

$$\sin(\sqrt{\mu}\,L) = 0 \quad \Leftrightarrow \quad \sqrt{\mu}\,L = n\pi \quad \text{for} \quad n \in \mathbb{N} \tag{45}$$

From Eq. (45), for any nonzero integer n $(n = 1, 2, 3, ...)$, the following expression for $\sqrt{\mu_n}$ is obtained:

$$\sqrt{\mu} = \frac{n\pi}{L} = \sqrt{\mu_n} \tag{46}$$

The subscript is used to label the particular n-value. According to Hancock (2006) and Ganster (2015), the following Eigenwerte of the Sturm-Liouville Problem are obtained:

$$\mu_n = \left(\frac{n\pi}{L}\right)^2 \tag{47}$$

The corresponding non-trivial solutions of Eq. (34) to the Eigenwerte in Eq. (47), are the following Eigenfunctions of the Sturm-Liouville Problem: [2]

$$F_n(x) = \sin\left(\frac{n\pi}{L}x\right) \tag{48}$$

5.4.3 Solving for $G(t)$

In the previous section, while solving for $F(x)$, the non-trivial solutions μ_n for all nonzero integers n were obtained. These Eigenwerte from Eq. (47) are now inserted into the second ODE from Eq. (33):

$$G'(t) = -\alpha\,\mu\,G(t) \tag{49}$$

[2] Ganster, M. (2015). *Partielle differentialgleichungen* [Mathematik 2 Bauingenieure SS 2015]. Graz University of Technology. Mathematik 2 Bauingenieure SS 2015. Retrieved June 10, 2020, from https://www.math.tugraz.at/~ganster/lv_mathematik_2_bau_ss_2015/08_partielle_dgln.pdf, p. 6

As Ganster (2015) and Hancock (2006) explain, the exponential approach delivers the following solutions to this ODE above, with the inserted Eigenwerte μ_n:

$$G_n(t) = b_n\, e^{-\alpha\mu_n t} = b_n\, e^{-\frac{\alpha n^2\pi^2}{L^2}t} \quad \text{for} \quad n \in \mathbb{N} \tag{50}$$

5.4.4 Solution for $\tilde{T}(x,t)$

Now, inserting the solutions for $F(x)$ from Eq. (48) and $G(t)$ from Eq. (50) into the initial expression for $\tilde{T}(x,t)$ after the separation of variables from Eq. (29), the following solutions are obtained:

$$\tilde{T}_n(x,t) = G_n(t)\, F_n(x) = b_n\, e^{-\frac{\alpha n^2\pi^2}{L^2}t} \sin\left(\frac{n\pi}{L}x\right) \tag{51}$$

As Ganster (2015) and Hancock (2006) explain, by applying the principle of superposition to Eq. (51) above, the following function for $\tilde{T}(x,t)$ is obtained:

$$\tilde{T}(x,t) = \sum_{n=1}^{\infty} b_n\, e^{-\frac{\alpha n^2\pi^2}{L^2}t} \sin\Big(\frac{n\pi}{L}x\Big) \tag{52}$$

Equation (52) is a solution to the PDE from Eq. (27), which also satisfies the boundary conditions from Eq. (28).

Taking a closer look at Eq. (52), one can see, that the transient solution consists out of three distinct terms. Firstly, the term $e^{-\frac{\alpha n^2\pi^2}{L^2}t}$ is responsible for the transient characteristic, as it ensures that $\tilde{T}(x,t) \xrightarrow{t\to\infty} 0$. Secondly, the term $\sin\big(\frac{n\pi}{L}x\big)$ ensures that the transient solution also satisfies the Dirichlet boundary conditions from Eq. (28). Without the factor b_n, the solution in Eq. (52) does not satisfy the initial condition of the PDE. Therefore, the third term b_n depends on the initial condition of the homogeneous PDE and will be developed with a Fourier Series in the next section.

However, the initial condition at the time $t = 0$ for the transient PDE from Eq. (27) has to be defined first. In the model, the initial temperature is set to zero Kelvin:

$$T(x,0) = 0 \tag{53}$$

Inserting this into Eq. (25), the following initial condition for the transient term $\tilde{T}(x,t)$ is obtained:

$$\tilde{T}(x,0) = -T^*(x) \tag{54}$$

With Eq. (54) above, b_n from Eq. (52) can now be developed.

5.4.4.1 Obtaining b_n from the Initial Condition

In order to find an expression for b_n, which satisfies the initial condition $T(x,0)$, the resulting transient initial condition from Eq. (54) is substituted into the solution of the PDE from Eq. (52):

$$\tilde{T}(x,0) = -T^*(x) \quad \Rightarrow \quad \sum_{n=1}^{\infty} b_n \sin\left(\frac{n\pi}{L}x\right) = -T^*(x) \tag{55}$$

Ganster (2015) defines an arbitrary function $f(x)$, which may be set as the initial condition, if $f(x)$ satisfies the given boundary conditions and is piecewise smooth over the defined interval. Applying the Dirichlet boundary conditions from Eq. (28), the function $f(x)$ satisfies $f(0) = f(L) = 0$ and is piecewise smooth over the interval $[0, L]$.

Equation (55) is now adjusted for the arbitrary function $f(x)$, which possesses the above mentioned characteristics:

$$f(x) = \sum_{n=1}^{\infty} b_n \sin\left(\frac{n\pi}{L}x\right) \tag{56}$$

Hancock (2006) identifies Eq. (56) as the Fourier Sine Series of $f(x)$. The Fourier Sine Series of $f(x)$ is odd and two periodic in space. It therefore converges to the following odd periodic extension of $f(x)$ over the interval $[-L, L]$, with a period $T = 2L$, for all $x \in \mathbb{R}$:

$$f(x) = \sum_{n=1}^{\infty} a_n \sin\left(\frac{n\pi}{L}x\right) \quad \text{with} \quad a_n = \frac{2}{L}\int_0^L f(x)\sin\left(\frac{n\pi}{L}x\right)dx \tag{57}$$

A comparison of coefficients leads to the following expression for b_n: [3]

$$a_n = b_n = \frac{2}{L}\int_0^L f(x)\sin\Big(\frac{n\pi}{L}x\Big)dx \tag{58}$$

It has been shown in the beginning of this chapter, that the steady-state solution $T^*(x)$ satisfies the Dirichlet boundary conditions. Since the steady-state solution is piecewise smooth over the interval $[0, L]$ as well, $f(x) = -T^*(x)$ is substituted into Eq. (58) and the following expression for b_n is gained:

$$b_n = -\frac{2}{L}\int_0^L T^*(x)\sin\Big(\frac{n\pi}{L}x\Big)dx \tag{59}$$

Now, the integral from Eq. (59) above is solved in order to gain a solution for b_n, which is then

[3] Ganster, M. (2015). *Partielle differentialgleichungen* [Mathematik 2 Bauingenieure SS 2015]. Graz University of Technology. Mathematik 2 Bauingenieure SS 2015. Retrieved June 10, 2020, from https://www.math.tugraz.at/~ganster/lv_mathematik_2_bau_ss_2015/08_partielle_dgln.pdf, p. 7

inserted into Eq. (52) to obtain a full expression for the transient solution $\tilde{T}(x,t)$.

$$\begin{aligned} b_n = \frac{2}{L}\int_0^L \Bigg[& \left[\sqrt{\pi\sigma}\,(x-\xi)\,\mathrm{erf}\left(\sqrt{\sigma}(x-\xi)\right) + e^{-\sigma(x-\xi)^2}\right] \\ & - \left[\sqrt{\pi\sigma}\left[(L-\xi)\,\mathrm{erf}\left(\sqrt{\sigma}\,(L-\xi)\right) - \xi\,\mathrm{erf}\left(\sqrt{\sigma}\xi\right)\right] + e^{-\sigma(L-\xi)^2} - e^{-\sigma\xi^2}\right]\frac{x}{L} \\ & - \left[\sqrt{\pi\sigma}\xi\,\mathrm{erf}\left(\sqrt{\sigma}\xi\right) + e^{-\sigma\xi^2}\right]\Bigg]\frac{A}{2\lambda\sigma}\sin\left(\frac{n\pi}{L}x\right)dx \end{aligned} \tag{60}$$

In order to reduce the integration effort, terms which do not include a variable x are summarised as constants C_3 and C_4 respectively:

$$C_3 = \sqrt{\pi\sigma}\left[(L-\xi)\,\mathrm{erf}\left(\sqrt{\sigma}\,(L-\xi)\right) - \xi\,\mathrm{erf}\left(\sqrt{\sigma}\,\xi\right)\right] + e^{-\sigma(L-\xi)^2} - e^{-\sigma\xi^2} \tag{61}$$

$$C_4 = \sqrt{\pi\sigma}\xi\,\mathrm{erf}\left(\sqrt{\sigma}\,\xi\right) + e^{-\sigma\xi^2} \tag{62}$$

This simplifies the expression for b_n from Eq. (60) accordingly:

$$b_n = \frac{A}{\lambda\sigma L}\int_0^L \sin\left(\frac{n\pi}{L}x\right)\left[\sqrt{\pi\sigma}\,(x-\xi)\,\mathrm{erf}\left(\sqrt{\sigma}(x-\xi)\right) + e^{-\sigma(x-\xi)^2} - \frac{x}{L}C_3 - C_4\right]dx \tag{63}$$

Using the sum rule, this term can be split into five separate terms, which can be integrated separately. The solutions to these five integrals have been named with a capital I and the respective subscript m. These five integrals differ significantly in complexity, whereby the first two integrals with the constants C_3 and C_4 are not very complex and have the following solutions:

$$I_1 = -C_4\int_0^L \sin\left(\frac{n\pi}{L}x\right)dx = -\frac{(L - L\cos(n\pi))}{n\pi}\,C_4 \tag{64}$$

The second integral can be integrated through substitution (see Appendix B).

$$I_2 = -C_3\int_0^L \sin\left(\frac{n\pi}{L}x\right)\frac{x}{L}\,dx = -\frac{(L\sin(n\pi) - Ln\pi\cos(n\pi))}{\pi^2 n^2}\,C_3 \tag{65}$$

The remaining three integrals however, show an increasing degree of complexity and have therefore been integrated with the aid of the Computer Algebra System (CAS) *Wolfram Mathematica 12.1*. The solution to the third integral is shown below in Eq. (66):

$$\begin{aligned} I_3 &= \int_0^L \sin\left(\frac{n\pi}{L}x\right)e^{-\sigma(x-\xi)^2}\,dx \\ &= \frac{1}{4}\sqrt{\frac{\pi}{\sigma}}e^{-\frac{n^2\pi^2+4in\pi\xi\sigma L}{4\sigma L^2}}\left[i\,\mathrm{erf}\left(\frac{in\pi + 2L\sigma(L-\xi)}{2L\sqrt{\sigma}}\right) - i\,\mathrm{erf}\left(\frac{in\pi - 2L\sigma\xi}{2L\sqrt{\sigma}}\right)\right. \\ &\quad \left. + e^{\frac{2in\pi\xi}{L}}\left(\mathrm{erfi}\left(\frac{n\pi - 2iL\sigma\xi}{2L\sqrt{\sigma}}\right) - \mathrm{erfi}\left(\frac{n\pi + 2iL\sigma(L-\xi)}{2L\sqrt{\sigma}}\right)\right)\right] \end{aligned} \tag{66}$$

Whereby erfi is the imaginary Error function in Eq. (66) and is defined as $\mathrm{erfi}\,(z) = -i\,\mathrm{erf}\,(iz)$.

The fourth integral has the following solution:

$$\begin{aligned} I_4 =& -\xi\sqrt{\pi\sigma}\int_0^L \sin\left(\frac{n\pi}{L}x\right)\operatorname{erf}\left(\sqrt{\sigma}(x-\xi)\right)dx \\ =& -\frac{L\xi}{2n}\sqrt{\frac{\pi}{\sigma}}\Bigg[-2\cos(n\pi)\operatorname{erf}\left(\sqrt{\sigma}(L-\xi)\right)-2\operatorname{erf}\left(\xi\sqrt{\sigma}\right) \\ & -ie^{-\frac{n^2\pi^2+4in\pi\xi\sigma L}{4\sigma L^2}}\left(e^{\frac{2in\pi\xi}{L}}\left(\operatorname{erfi}\left(\frac{\frac{n\pi}{L}-2i\sigma(L-\xi)}{2\sqrt{\sigma}}\right)-\operatorname{erfi}\left(\frac{\frac{n\pi}{L}-2i\sigma\xi}{2\sqrt{\sigma}}\right)\right)\right. \\ & \left.+\operatorname{erfi}\left(\frac{n\pi+2i\sigma\xi L}{2L\sqrt{\sigma}}\right)-\operatorname{erfi}\left(\frac{n\pi-2i\sigma L(L-\xi)}{2L\sqrt{\sigma}}\right)\right)\Bigg] \end{aligned} \tag{67}$$

The fifth and last integral has the highest degree of complexity, as it possesses an additional variable x, compared to the fourth integral I_4. Unfortunately, the solution of the fifth integral is too long to be displayed in this section. Therefore, the full solution to the integral I_5 from Eq. (68) below is displayed in Appendix B.

$$I_5 = \sqrt{\pi\sigma}\int_0^L x\sin\left(\frac{n\pi}{L}x\right)\operatorname{erf}\left(\sqrt{\sigma}(x-\xi)\right)dx \tag{68}$$

Now, the sum of all five solved integrals from Eq. (64) – (68) provides the following solution for b_n:

$$b_n = \frac{A}{\lambda\sigma L}\sum_{m=1}^{5} I_m \tag{69}$$

This expression for b_n from Eq. (69) above is now substituted into Eq. (52):

$$\tilde{T}(x,t) = \frac{A}{\lambda\sigma L}\sum_{n=1}^{\infty}\left(I_1+I_2+I_3+I_4+I_5\right)e^{-\frac{\alpha n^2\pi^2}{L^2}t}\sin\left(\frac{n\pi}{L}x\right) \tag{70}$$

Equation (70) now displays the transient solution $\tilde{T}(x,t)$ depending on time t and position x. It not only adheres to the boundary conditions from Eq. (28), but also satisfies the initial condition from Eq. (54) of the original transient PDE from Eq. (27). This means, that the transient term $\tilde{T}(x,t)$ is initially equal to the negative steady state solution $-T^*(x)$ at time $t = 0$ and gradually disappears with progressing time. This is crucial for the full solution $T(x,t) = \tilde{T}(x,t) + T^*(x)$, as it allows it to first adhere to the initial condition $T(x,0) = T^*(x) - T^*(x) = 0$ and then progress towards the steady-state solution $T^*(x)$ with increasing time t, as the negative transient term $\tilde{T}(x,t)$ disappears.

Thus, the full solution $T(x,t)$ is the sum of the individual transient and steady-state solutions from Eq. (23) & (70), displayed in Eq. (71) on the following page.

$$
\begin{aligned}
T(x,t) = \frac{A}{\lambda\sigma}\Bigg[\Bigg[\frac{1}{L}\sum_{n=1}^{\infty}\left(I_1+I_2+I_3+I_4+I_5\right)e^{-\frac{\alpha n^2\pi^2}{L^2}t}\sin\left(\frac{n\pi}{L}x\right)\Bigg] \\
+\frac{1}{2}\Bigg[-\left(\sqrt{\pi\sigma}\,(x-\xi)\,\mathrm{erf}\left(\sqrt{\sigma}(x-\xi)\right)+e^{-\sigma(x-\xi)^2}\right) \\
+\left(\sqrt{\pi\sigma}\left[(L-\xi)\,\mathrm{erf}\left(\sqrt{\sigma}\,(L-\xi)\right)-\xi\,\mathrm{erf}\left(\sqrt{\sigma}\xi\right)\right]+e^{-\sigma(L-\xi)^2}-e^{-\sigma\xi^2}\right)\frac{x}{L} \\
+\left(\sqrt{\pi\sigma}\xi\,\mathrm{erf}\left(\sqrt{\sigma}\xi\right)+e^{-\sigma\xi^2}\right)\Bigg]\Bigg]
\end{aligned}
\tag{71}
$$

By inspecting the final solution from Eq. (71) in detail, the effect of the material properties on the whole solution become clearer. The thermal conductivity λ in the denominator is the only material property affecting the steady state solution from Eq. (23). Therefore, the thermal conductivity alone affects the absolute maximum value of the solution at steady-state conditions at any given point. The lower the thermal conductivity λ is, the higher the achieved temperature $\tilde{T}(x,t)$ in the rod will be. On the other hand, the thermal diffusivity $\alpha = \frac{\lambda}{\rho\, c_p}$ is found in the exponent of the transient solution. Therefore, the relationship between the thermal conductivity λ and the specific heat capacity combined with the density $\rho\, c_p$ determines how fast the steady state solution is achieved. If the rod is made out of a material with a high thermal conductivity and low specific heat capacity and density, then the material will react very quickly to transient external conditions (Showalter, 2013).

This solution demonstrates the importance of numeric computational modelling, as the analytical solution of a simple rod model with a Gaussian function as a heat source already requires a significant mathematical effort. Thus, it becomes evident that solving and modelling complex and applicable heat flow problems, without the aid of numeric computational software, is simply impossible.

5.4.5 Transient Solution Comparison

The accuracy of the analytically calculated full solution during the transient period is analysed in the following section. In Figure 17 below, the with time exponentially disappearing transient solution is neatly visualised. As already discussed in detail in the previous section, at time $t = 0\,\mathrm{s}$ the negative transient part of the total solution is equal to the steady-state solution and thus, the temperature at $T(x, t = 0\,\mathrm{s})$ is zero Kelvin. With progressing time, the negative transient solution $\tilde{T}(x,t)$ is exponentially increasing in value towards zero at steady-state. Therefore, the total solution is exponentially approaching the steady-state solution with passing time (see Figure 17).

Even though the temperature at the rod model's centre is already within a few degrees of the steady-state solution after $t = 0.5$ s, true steady-state conditions are only achieved after $t = 1.3$ s. At this point the maximum temperature of 315.97 K at the rod's centre is reached and the total net heat transfer rate to the rod model's boundaries is sufficiently close to the

original heat input.

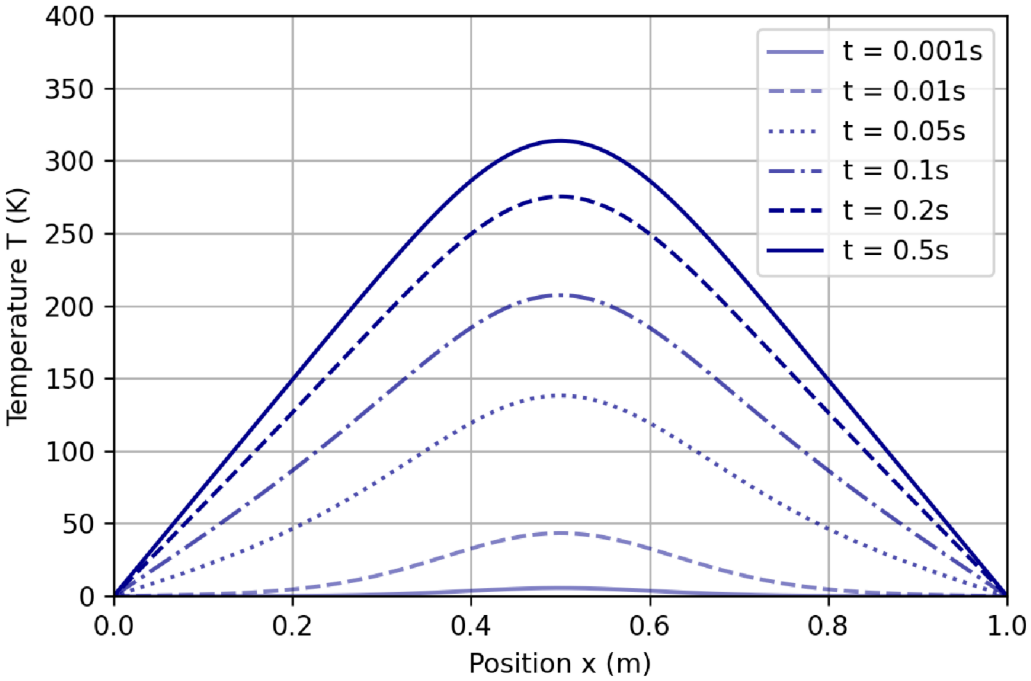

Figure 17: Time progression of the numerically calculated transient solution on the rod's x-axis.

When discussing the accuracy of numerically calculated transient solutions, the time-step size has to be inspected as well. While smaller time-steps ensure a higher solution accuracy, a balance between a sufficiently accurate solution and an efficient calculation time has to be found for every numerical model. This is inspected in Figure 18 below, where the absolute temperature difference between the analytical and numerical solution during the early transient stage at $t = 0.01$ s for three different time-step sizes can be observed. Similarly to the previous section, the numerically calculated values were subtracted from the analytically calculated solution. Therefore, a positive temperature difference indicates that the analytically calculated solution seems to be slightly higher than the numerically calculated solution and visa versa. Alternatively, the same absolute temperature difference is calculated with the optimal time-step size of 10^{-3} s at different times t from transient to steady-state conditions and is displayed along the rod's x-axis in Figure 19 below.

Two aspects have to be considered when discussing the accuracy of the solution in the transient period, namely the time-step size and how far the solution has progressed to steady-state. As shown in Figure 19 below, the more time progresses and the further the transient solution approaches the steady-state solution, the more accurate the solution becomes. This is valid for any chosen time-step size. Secondly, the shorter the time-steps are, the more accurate the solution is (see Figure 18). Yet, this increase in accuracy is obviously linked to an increase in computational effort and calculation time. As seen in Figure 18 below, a time-step size of 0.01 s is too high for this rod model, as the temperature differences to the numerical

solutions with lower time-step sizes and to the analytical solution itself are simply to high. On the other hand, a time-step size of 10^{-4} s has an extremely low temperature difference to the analytically calculated solution, however the calculation time is not very efficient.

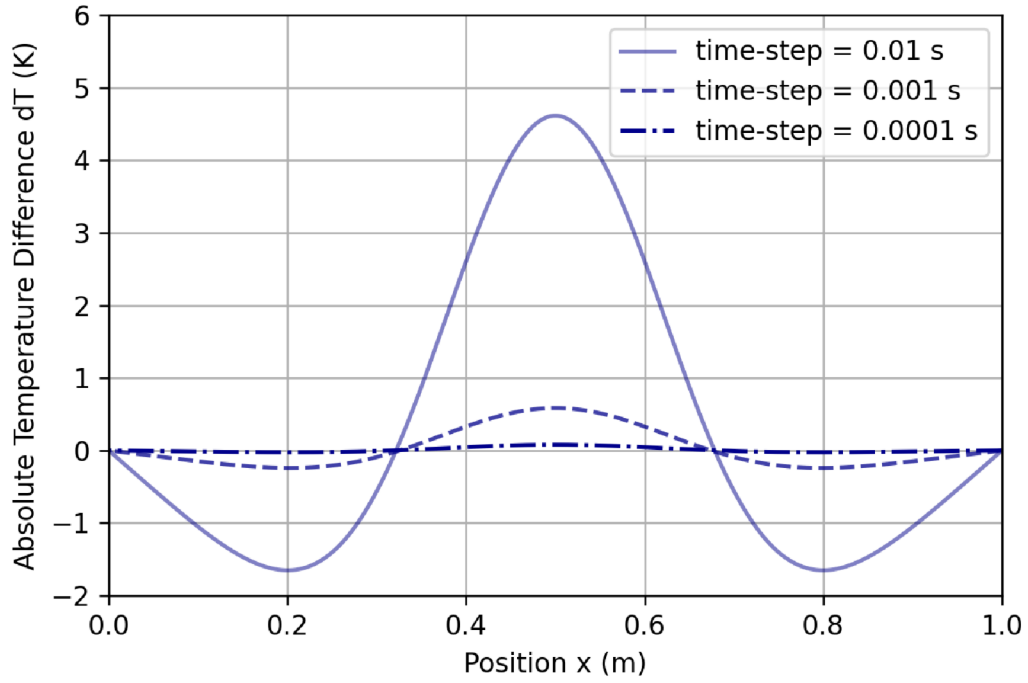

Figure 18: Absolute difference (analytic – numeric) for varying time-step sizes at time $t = 0.01$ s.

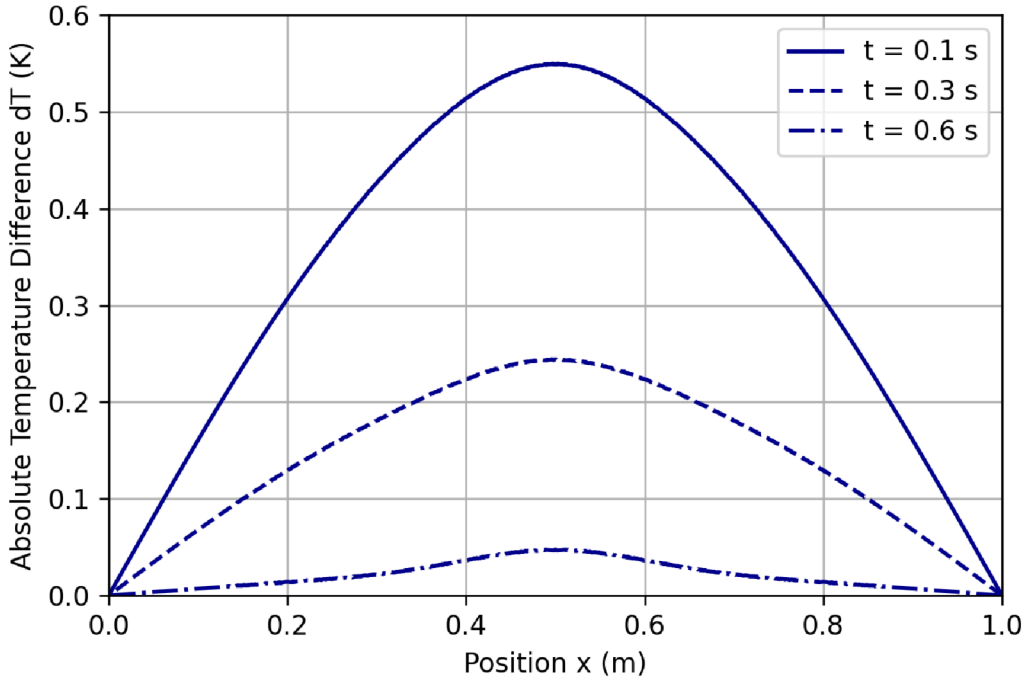

Figure 19: Absolute difference (analytic – numeric) at varying times with a time-step size of 10^{-3} s.

Thus, a time-step size of 10^{-3} s should be chosen for this model, since it offers a compromise between a sufficiently accurate solution, even in the earliest transient stage, and an acceptably efficient calculation time. Another interesting observation in Figure 18 above is the development of the temperature difference between the analytically and numerically calculated solution in the transient stage. For the solution with a time-step size of 10^{-3} s in the early transient period at $t = 0.01$ s in Figure 18 a negative temperature difference to either side of the rod is observed. The negative part disappears with progressing time and cannot be observed at later times in Figure 19. This neatly displays the role of the Fourier series expansion of the analytically calculated transient solution and how the transient solution's effect on the total solution is diminished with progressing time.

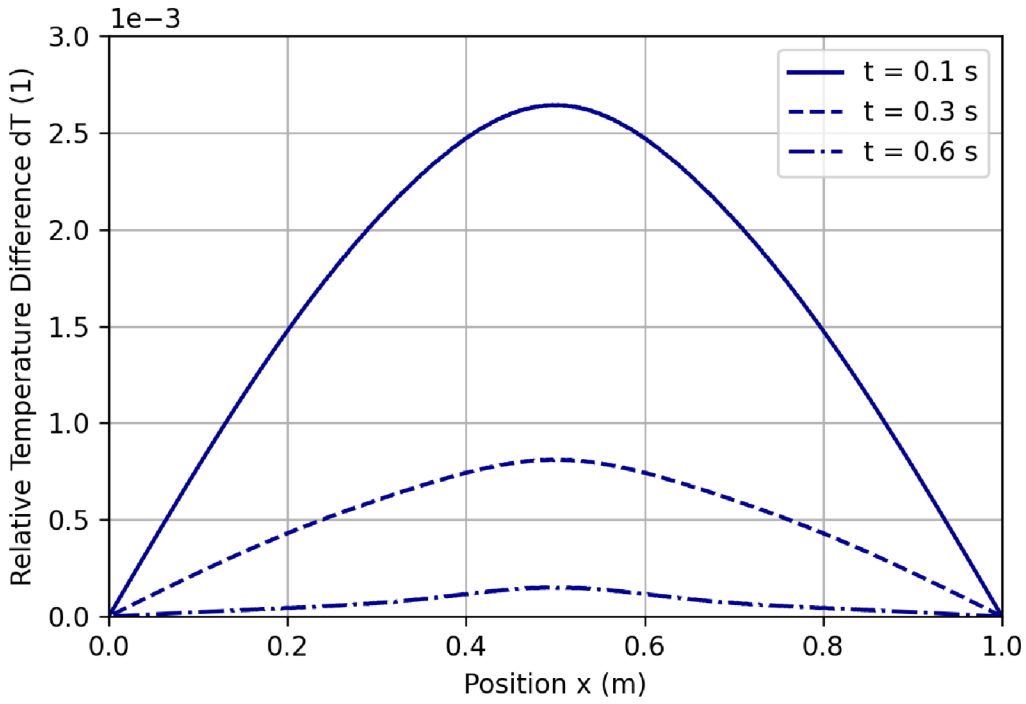

Figure 20: Relative difference (analytic – numeric) at varying times with a time-step size of 10^{-3} s.

Taking a look at the temperature difference relative to the individual solution's maximum temperature between the analytically and numerically calculated solutions in Figure 20 above, one can see that the transient solution's relative temperature difference is significantly higher than the previously calculated steady-state solution's error. The transient solution's relative error is no longer below the steady-state solution's 0.01 percent mark. Nevertheless, the relative error between the two solutions is well below 0.3 percent in the early transient stage and then gradually approaches the steady-state solution's relative error with 0.015 percent at $t = 0.6$ s. These relative error magnitudes can still be deemed negligible and thus, the analytically calculated transient solution for a time-step size of 10^{-3} s is accurate as well. In Figure 21 below, the heat conduction from transient to steady-state conditions through the rod model is visualised in the form of 2D contour plots at a cross-section of the rod model's xy-plane.

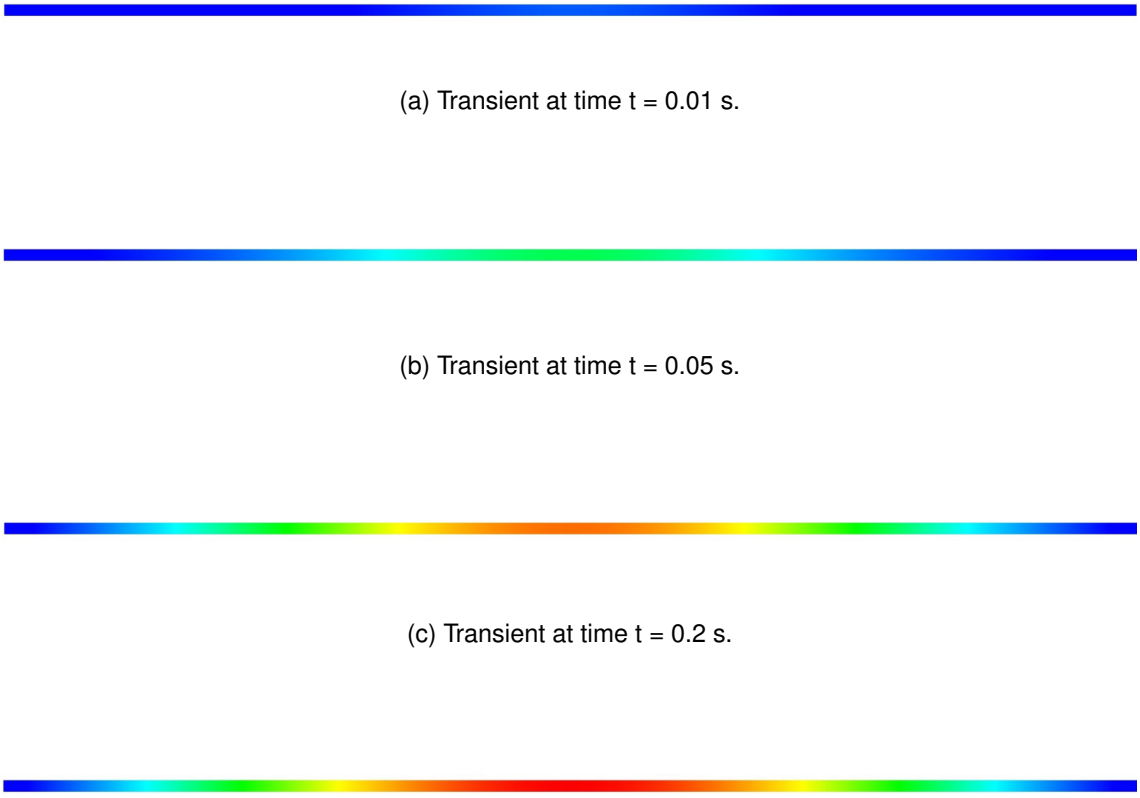

(a) Transient at time t = 0.01 s.

(b) Transient at time t = 0.05 s.

(c) Transient at time t = 0.2 s.

(d) Steady-state from approximately time t = 1.3 s onward.

Figure 21: Contour plots of the rod model's xy-plane from transient to steady-state conditions.

This concludes the analytical solution's chapter, whereby the physical heat conduction concepts of the numeric *ANSYS Fluent* solver have been accurately verified. Furthermore, the basic processes behind numeric modelling and how a model's accuracy is determined and tested, have been displayed to the reader. Furthermore, the effect of material properties on the heat conduction equation could be investigated. The thermal conductivity alone affects the absolute maximum value of the solution at steady-state conditions at any given point. The lower the thermal conductivity λ is, the higher the achieved temperature at the thermal equilibrium will be. The thermal diffusivity $\alpha = \frac{\lambda}{\rho\, c_p}$, which is defined as the relationship between the thermal conductivity λ and the specific heat capacity combined with the density $\rho\, c_p$, determines how fast the steady state solution is achieved. Understanding these effects is important for the CFD model's material property variation presented in chapter eight.

6 Thermo-Pipe Model

In the following chapter, a developed "Thermo-Pipe" model and its corresponding experiment, which was conducted by the AIT research team as a part of the *GEOFIT* project's framework, will be discussed. Due to the large dimensions of the earth basket experiment, which will be analysed in the next chapter, a down-scaled experimental setup was chosen to observe the heat conductive behaviour of different sands and soils before a time consuming large-scale experiment is conducted. The "Thermo-Pipe" has a similar height as the large slinky heat exchanger experiment, in order to create similar conditions regarding the consolidation of the heat conductive medium inside the pipe. This experimental setup was modelled with the *ANSYS Fluent* solver as well. If the experiment and model provide matching and satisfying results, the tested substrate may be used in an experimental run of the slinky heat exchanger experiment. Furthermore, the numeric model of the "Thermo-Pipe" – once validated – can be used to further "pre-select" sand and soil types with known material properties.

6.1 Experiment Setup

The experimental setup of the "Thermo-Pipe" consists out of two *DN160* PVC temperature resistant pipes with a wall thickness of 3.9 mm, which are joined by a sleeve. The total length of the "Thermo-Pipe" is 1140 mm. A heating plate, which acts as the heat source, was placed into the sleeve at the centre of the pipe. With a radius of 56 mm, the heating plate's radius is 2 cm smaller than the pipe's inner radius, in order to avoid exceeding the plastic's temperature rating. The pipe is then filled with a heat conducting substrate like sand or soil. As shown in Figure 22 below, *PT1000* Resistance Temperature Detectors (RTDs) were then placed along the centre of the pipe on either side of the heating plate during the first test runs. The sketch in Figure 22 below was mirrored, as the "Thermo-Pipe" setup was identical on either side for this test run.

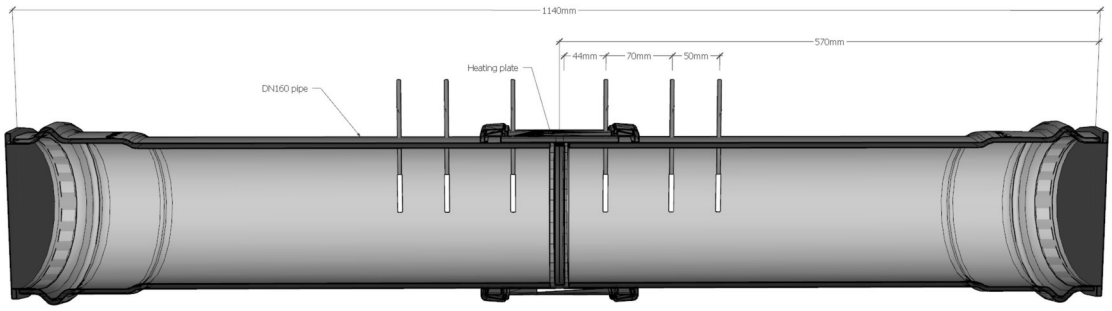

Figure 22: Sketch of the Thermo-Pipe sensor placements during test runs. [1]

As the heating plate emits heat equally in both axial directions, this test was done to ensure correct and uniform sand placement in the zones affected by a measurable temperature

[1] AIT Austrian Institute of Technology. (2020). GEOFIT research project

change. Once this was proven during the first test run, the sensors were then only placed on one side of the heating plate, so that not only the linear heat conduction in the centre of the "Thermo-Pipe", but also the temperature drop towards the walls could be measured. Since the experiment was not conducted in a controlled climate chamber, the ambient temperature was logged as well. This was done, so that the influence of the change in ambient temperature onto the experiment could be evaluated and quantified. However, for no experimental run the change in ambient temperature proved to be severe enough to have a detectable effect on the insulated "Thermo-Pipe". Figure 23 below depicts the final sensor placement.

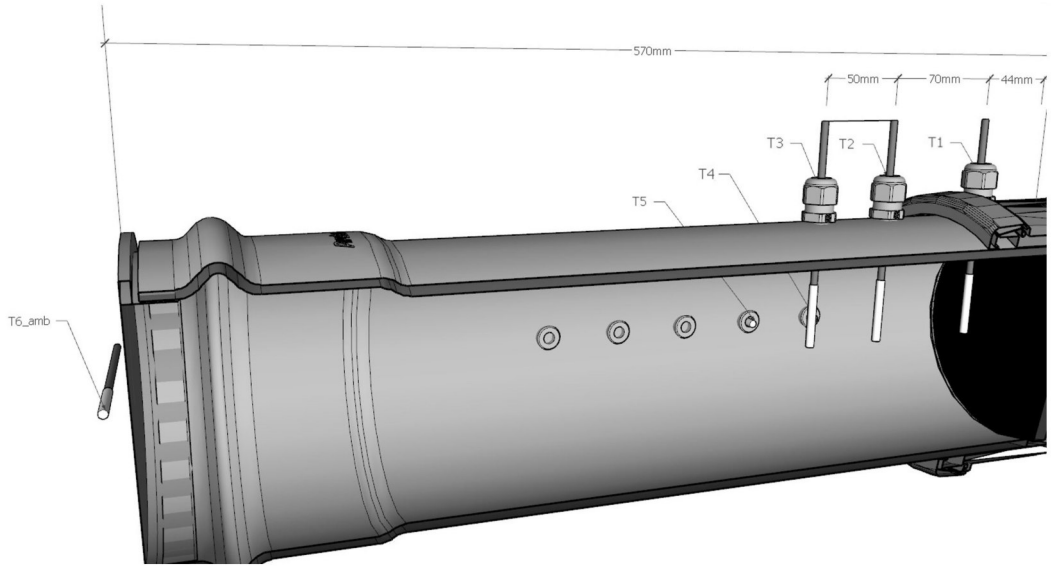

Figure 23: Sketch of the final Thermo-Pipe sensor placement. [2]

An analysis of the expected maximum temperatures and extent of the measurable temperature increase along the length of the "Thermo-Pipe" was conducted with the numeric model beforehand. This lead to the following sensor positions displayed in Figure 23 above, whereby sensors T1, T2 and T3 are placed in the pipe's longitudinal centre axis at 44 mm, 114 mm and 164 mm respectively from the heat source's centre. The RTD sensors T4 and T5 are placed 5 mm from the wall and are aligned with the furthest centre RTD sensors T2 and T3 respectively. T6 is denoted as the ambient temperature sensor.

6.2 Material Parameters

For the model's validation run, the same dry sand as the one from the large-scale earth-basket experiment was used as a heat conducting medium. Probes from the experimental earth basket setup were taken and the material's density ρ, specific heat capacity c_p and thermal conductivity λ were measured in the AIT's laboratory. Whereby the thermal conductivity was measured using a Heat-Flow-Meter (HFM), which uses the hot-plate-method. When speaking of density, it should be noted that the bulk density of the probes was measured and used

[2] AIT Austrian Institute of Technology. (2020). GEOFIT research project

in the model. Since pore space and porosity cannot be separately factored into the *ANSYS Fluent* model, the accurately measured bulk density is used to account for porous spaces. The mentioned measured material properties have been summed up in Table 1 below, whereby multiple measurement runs per probe have been recorded and the mean value from these was taken. Charts of all runs and their statistical analysis are attached in Appendix C.

Table 1: Mean values from AIT measurements of dry sand in large-scale earth basket experiment.

Mean Material Property Values of Dry Sand Probes			
Temperature (°C)	λ (W m^{-1} K^{-1})	c_p (J g^{-1} K^{-1})	ρ (g cm^{-3})
-10	0.3809	0.889	1.8220
0	0.3784	0.947	1.8220
10	0.3796	0.941	1.8220
20	0.3840	0.962	1.8220
25	0.3884	x-x-x	1.8220
30	0.3874	0.985	1.8220
40	0.3896	1.027	1.8220
50	0.3915	1.065	1.8220
60	0.3929	1.038	1.8220
70	0.3873	1.061	1.8220

After the "Thermo-Pipe" was filled with dry sand with the material properties listed in Table 1 above, the pipe was additionally insulated as well. This was done, to firstly isolate the heat conducting medium sand from ambient temperature effects and secondly, to create a lower temperature difference at the transition from the small model's boundaries to the surrounding environment. The latter is important to generate a comparable model in the next section. According to the PVC pipe's manufacturer, the plastic has a thermal conductivity of 0.22 W m^{-1} K^{-1}, a specific heat capacity of 1.9 J g^{-1} K^{-1} and a density of 0.950 g cm^{-3}. In order to sufficiently insulate the "Thermo-Pipe", it was wrapped in 13 mm thick *Kaiflex ST* insulation material.

The change of the insulation material's thermal conductivity with change in temperature, depicted in Table 2 on the following page, has been provided by the manufacturer through the following formula displayed as Eq. (72) below: [3]

$$\lambda_{Ins.}(T) = 0.034 + 7.2 \cdot 10^{-5} T + 1.2 \cdot 10^{-6} T^2 \tag{72}$$

[3] Reprinted from Kaimann GmbH. (2020). Kaiflex ST Datenblatt. Retrieved June 17, 2020, from https://www.kaimann.com/authoring/auth/Documents/Kaiflex_ST-AUTDE.pdf

Table 2: Material values provided by the manufacturer of the 13 mm *Kaiflex ST* © insulation.

Material Property Values of Thermo-Pipe Insulation Material			
Temperature (°C)	λ (W m^{-1} K^{-1})	c_p (J g^{-1} K^{-1})	ρ (g cm^{-3})
-10	0.0334	1.450	0.090
0	0.0340	1.450	0.090
10	0.0348	1.450	0.090
20	0.0359	1.450	0.090
30	0.0372	1.450	0.090
40	0.0388	1.450	0.090
50	0.0406	1.450	0.090
60	0.0426	1.450	0.090
70	0.0449	1.450	0.090
80	0.0474	1.450	0.090
90	0.0502	1.450	0.090
100	0.0532	1.450	0.090

Figure 24 below depicts the aforementioned "Thermo-Pipe" experimental setup.

(a) Filling process of the Thermo-Pipe.

(b) Insulated Thermo-Pipe setup.

Figure 24: Pictures of the Thermo-Pipe filling and experimental setup. [4]

[4] AIT Austrian Institute of Technology. (2020). GEOFIT research project

6.3 Model Setup

A corresponding "Thermo-Pipe" model with the same dimensions and material parameters was developed. Since the "Thermo-Pipe" model is radially uniform in shape and material, a two dimensional mesh of the cross-section of the vertically halved pipe, with the x-axis running through the pipe's longitudinal centre axis, was created with the *ANSYS* Computer-Aided Design (CAD) software *SpaceClaim* and meshing program (see Figure 25 below). The numeric solver *Fluent* can then model this two dimensional space with an "axisymmetric" option, whereby the solution is projected 360 degrees radially. This was done to significantly decrease the computational calculation time to further enhance the model's capability as a numerical and experimental "quick-testing" station. Due to the model's geometry, the axisymmetric calculation does not significantly decrease the model's accuracy, as the solution has no spatial dependence in the circumferential direction. Only the radial coordinates and distance to the heat source are influencing factors.

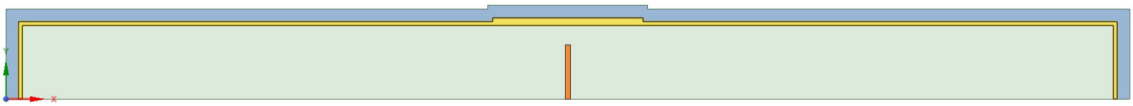

(a) View of the full length Thermo-Pipe model in *ANSYS SpaceClaim*.

(b) Enlarged half of the Thermo-Pipe model in *ANSYS SpaceClaim*.

Figure 25: Cross-sectional area of half the Thermo-Pipe in the x-y plane.

In Figure 25 above, the cross-sectional area of the heating-plate with a radius of 56 mm is depicted in orange. In the experimental setup the heat source has a spiral shape, which was simplified as a heating plate in the model. A variety of shapes approximating the heat source's geometry have been tested, including a thin wall extending over the pipe's entire diameter and individual rings with varying diameters. However, the heating plate's solution has shown no significant deviation to geometries of higher complexities and was thus chosen as a good geometrical approximation of the spiral heat source in the experiment. The heat conductive medium sand is depicted in green, the PVC pipe's wall with a wall-thickness of 3.9 mm and an inner radius of 76.1 mm in yellow and lastly the 13 mm *Kaiflex ST* insulation material in blue. Identical to the experimental setup, the full length of the "Thermo-Pipe" is $1\,140$ mm — excluding the insulation material on either side. The heat source is situated exactly at the pipe's centre, where the added thickness of the joining sleeve is visible as well.

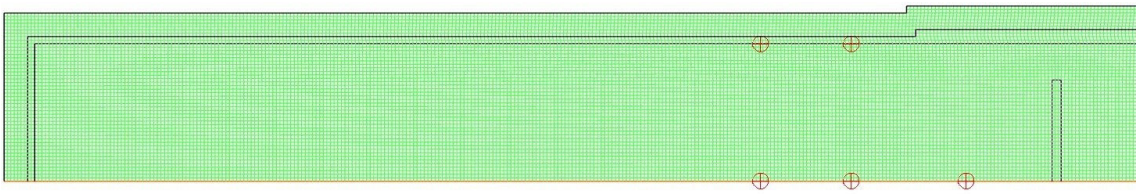

Figure 26: Enlarged view of the Thermo-Pipe mesh with the sensor data-point locations.

After the design of the Thermo-Pipe has been created and meshed, it is imported into the numeric CFD modelling software *ANSYS Fluent*. The borders between the different types of interior solids, namely copper (heating plate), sand, plastic and insulation are defined as walls and displayed in black in Figure 26 below. The x-axis is defined as an axis (orange) in *Fluent* as well, around which the model's solution is rotated as previously explained. Point-surfaces are added at the same locations where the RTD sensors were placed in the experiment and can be observed as red dots in Figure 26 above. The mesh itself has an element size of 2 mm, with $28\,246$ cells in the two dimensional planar space. On the three exterior insulation walls, namely the top, bottom and mantle, a constant temperature of 296.65 K is applied as a boundary condition. This temperature is equal to the average ambient temperature measured with the RTD sensor T6. During the experimental run the heating plate in the centre of the pipe emitted a constant heat of 21.9 W. Therefore, at steady-state conditions the total transferred heat through the model's outer boundary walls should approach -21.9 W. The total transported heat through all three exterior walls after $200\,000$ s is precisely -21.8798 W and is still gradually advancing towards the constant heat input with passing time.

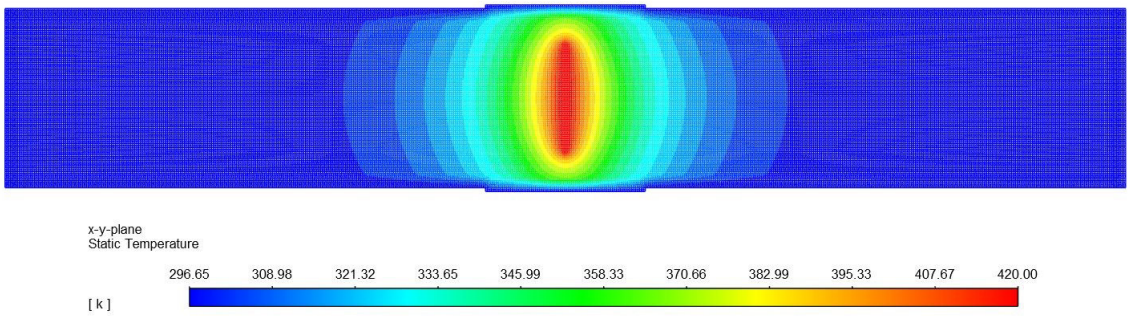

Figure 27: Temperature contour plot of the full cross-sectional pipe area at $t = 200\,000$ s

In Figure 27 above, the temperature distribution across the "Thermo-Pipe's" entire cross-section at steady-state conditions can be observed. The heat conduction in x-axis direction caused by the heat source at the centre of the pipe and the temperature drop towards the pipe's wall in the y-axis direction is visualised here.

The temperature distribution over time in the "Thermo-Pipe" is visualised in Figure 28 below.

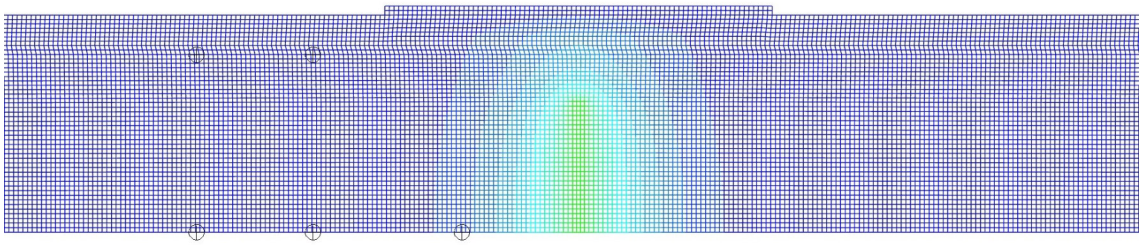

(a) Temperature contour plot of the cross-sectional pipe area at t = 5.000 s.

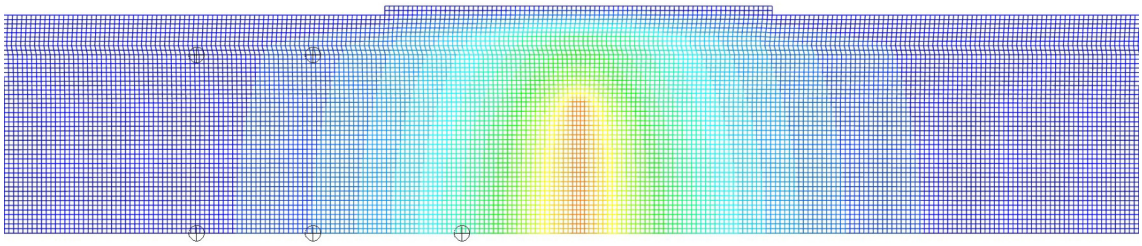

(b) Temperature contour plot of the cross-sectional pipe area at t = 25.000 s.

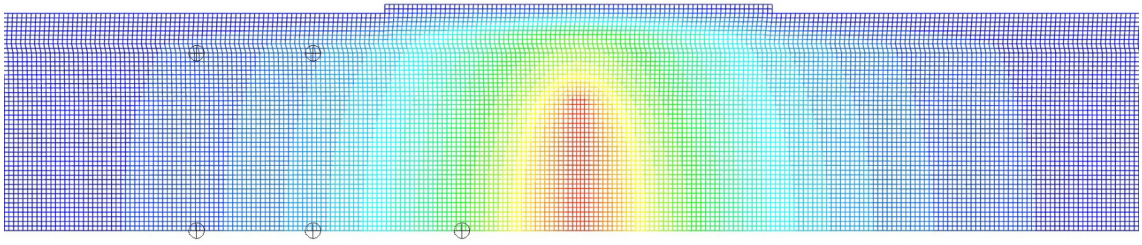

(c) Temperature contour plot of the cross-sectional pipe area at t = 50.000 s.

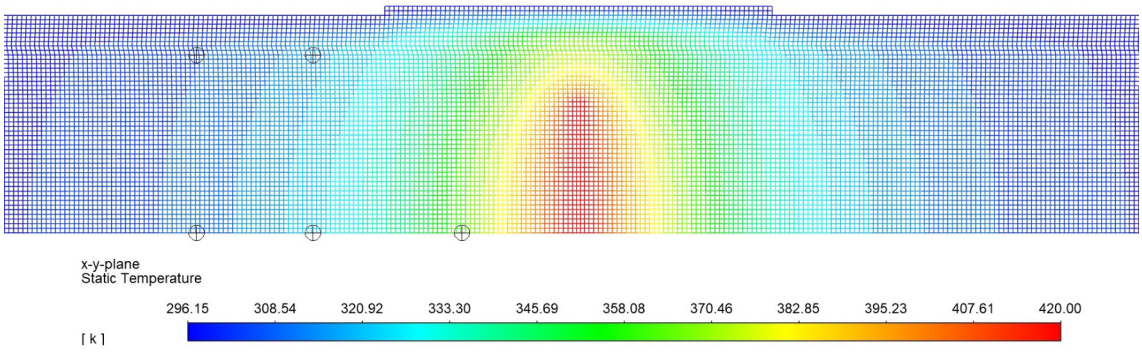

(d) Temperature contour plot of the cross-sectional pipe area at t = 150.000 s.

Figure 28: Temperature contour plots of the Thermo-Pipe during the transient period.

The coordinates of the RTD sensors are indicated by the black point surfaces. The model is behaving as expected, was deemed mesh-independent and the time-step size of $1\,000$ s also

provides an accurate solution. Therefore, the temperature data at the sensor locations can now be compared to the logged "Thermo-Pipe" experimental data in the following section.

6.4 Comparison between Experiment and Model

Now, the numeric model described in the previous section is compared to the recorded data from the corresponding experiment.

In Figure 29 below, the solution of the numeric model, at the RTD sensor positions T1, T2, and T3 situated on the x-axis in the centre of the pipe, are plotted against the results of the experimentally logged temperature data at the same positions. Simulation results are always plotted with dashed lines and experiment data is plotted with a solid line, unless stated otherwise. Once steady-state conditions in the experiment have been reached and no significant change in temperature was detected at the sensor points, the experiment run was completed. For better visualisation purposes, the steady-state temperature level of the experimental data is indicated by a dotted line.

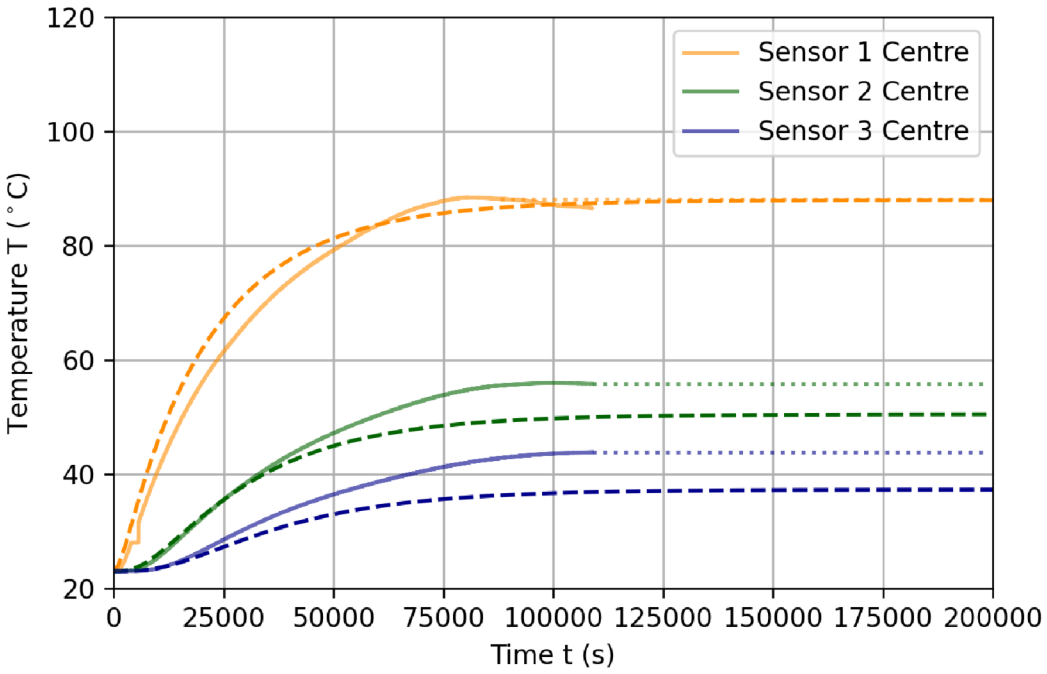

Figure 29: Thermo-Pipe simulation (- - -) and experiment (—) at sensors T1, T2 and T3.

While comparing the simulation results with the data recorded during the experiment, two aspects should be regarded independently of each other. Firstly, the match of the experimentally measured and simulated maximum temperature at steady-state conditions. As discussed in detail during the calculation of the analytical solution in a previous chapter, the thermal conductivity of the used materials is responsible for the magnitude of the maximum temperature at steady-state. Secondly, the fit of the experimentally measured and simulated temperature

curves at transient conditions should be inspected. The thermal diffusivity influences how "fast" the solution reaches the maximum temperature. Additionally, other factors regarding the nature of the model have to be addressed as well. In the case of the "Thermo-Pipe", the rather small scale and elongated shape of the pipe may cause the model's boundary conditions to have an unrealistically large impact on the solution. Furthermore, in small scale experiments and models the sensor placement accuracy might prove to be an issue as well. An off-set of a few millimetres may already have a large impact on the measured data and calculated solutions. As the "Thermo-Pipe" is manually wrapped in the $13\ \mathrm{mm}$ insulation sheet, the actual insulation efficiency may vary slightly from the supplied material properties as well.

In Figure 29 above, an increase in temperature difference at steady-state conditions between the experiment and simulation at the centre of the pipe, with increasing distance between sensor and heat source, can be observed. The same trend is also observable at the temperature sensors T4 and T5, as shown in Figure 30 below. They are placed at the "Thermo-Pipe's" inner wall, at the same distance in x-axis direction as temperature sensors T2 and T3. Therefore, this temperature difference is most likely caused by the "Thermo-Pipe's" relatively short distance between the sensor point locations and the model's boundary conditions, which are applied to its outer walls.

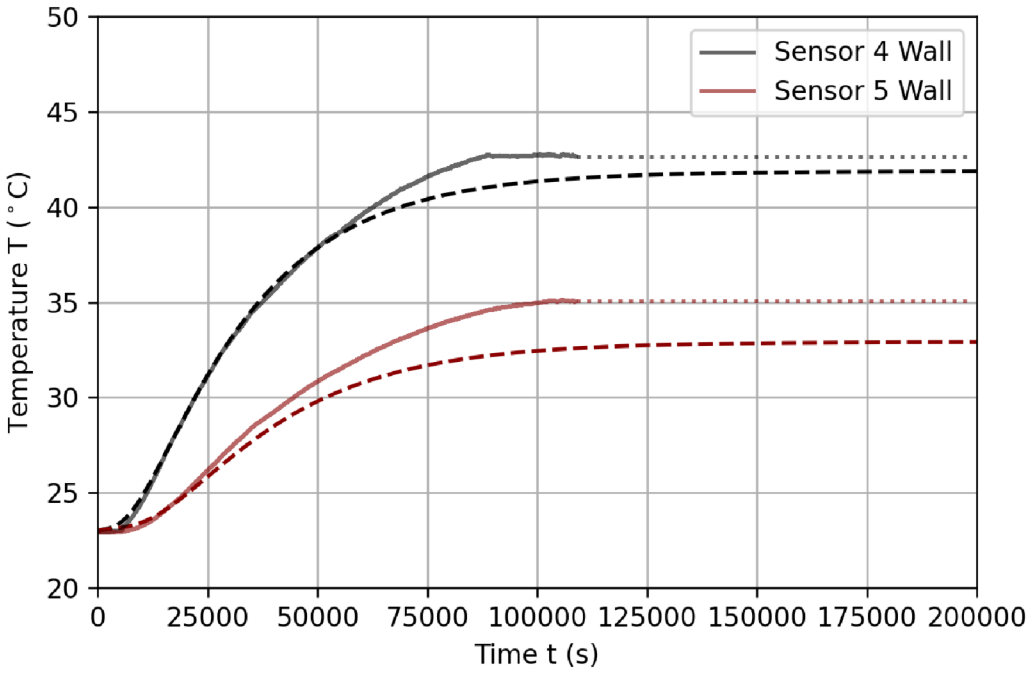

Figure 30: Thermo-Pipe simulation (- - -) and experiment (—) at sensors T4 and T5.

Taking a closer look at the transient section of the model and experiment, it is evident that the best fit between the model and experiment is at the two sensor positions T2 and T4. Both are placed at a medium distance of $114\ \mathrm{mm}$ in x-axis direction from the heat source. While the model's solution seems to be slightly too "fast" at the nearest sensor position T1 and slightly too "slow" at the furthest sensor positions T3 and T5 (see Figures 29 and 30). This can

be better visualised by plotting the absolute temperature difference between the model and experiment over time at the corresponding sensor positions. This has been done in Figures 31 and 32 below, whereby the experiment's measured data has always been subtracted from the simulated model's solution.

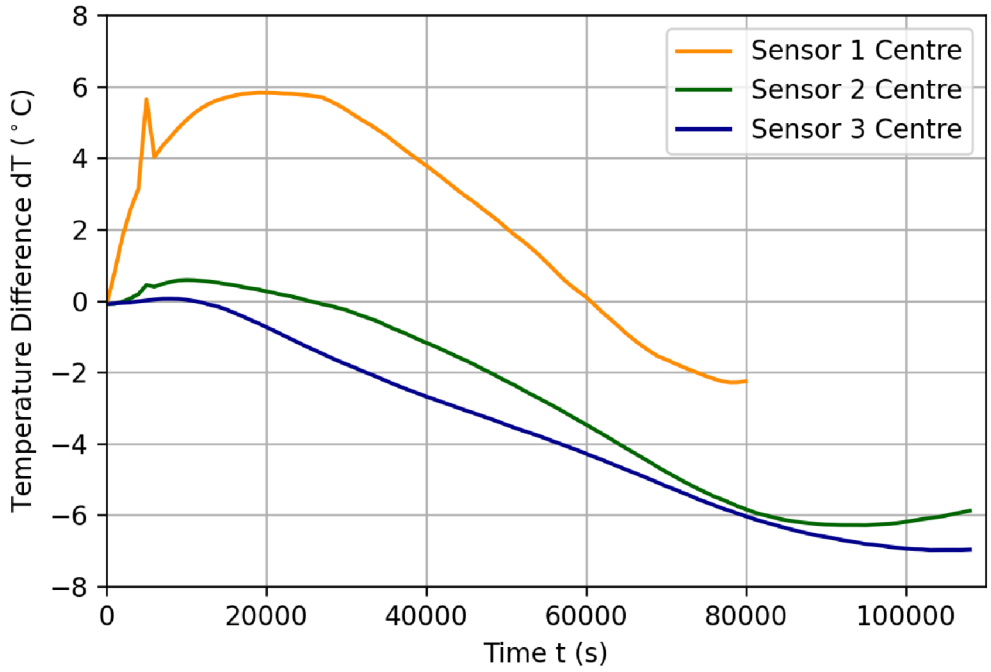

Figure 31: Thermo-Pipe temperature difference at T1, T2 and T3: simulation – experiment.

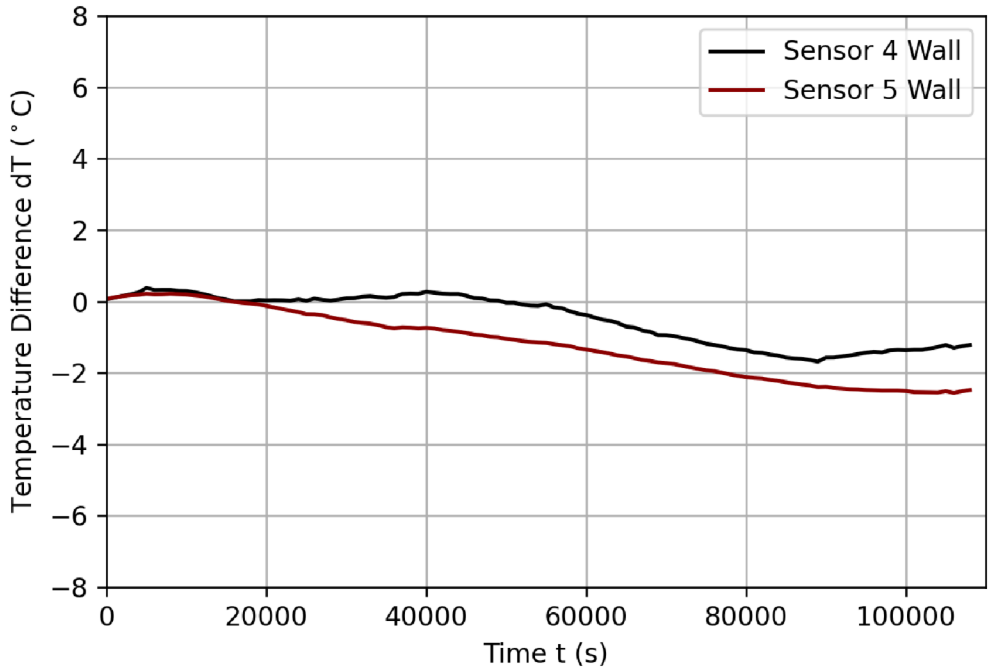

Figure 32: Thermo-Pipe temperature difference at T4 and T5: simulation – experiment.

Taking a closer look at the temperature difference curves of sensor points T1, T2 and T3 in Figure 31 above, all three sensor points follow the same trend. The temperature spike, which is visible in Figures 29 and 31, as well as the temperature decrease at sensor point T1 after steady-state conditions have been reached, completely fall out of the trend and are therefore declared as an anomaly. Disregarding these anomalies, the trends at the centred sensor positions as well as at the wall show good parallel behaviour. The large positive temperature difference at T1 during the early transient period could be explained by the close vicinity of the sensor point to the heat source. With a distance of 44 mm from the heating plate, a sensor placement inaccuracy of 1 mm could already cause detectable temperature differences. The other sensor points, which are placed further away from the heat source, are more resistant to inaccuracies in sensor positioning.

6.5 Implications for Large-Scale Experiments

The results of the "Thermo-Pipe" validation have to be interpreted by keeping the nature and purpose of the experiment and corresponding model in mind. As discussed previously, the pipe's scale and geometrical shape causes a deviation regarding the maximum temperature at steady-state conditions between model and experiment. Nonetheless, the transient temperature profile during the transient period is satisfyingly accurate. The goal of the "Thermo-Pipe" experiment and model is to serve as a pre-selection and testing tool for potential soil and sand combinations, to be used as a heat conductive medium in further large-scale and time consuming experiment runs. If the previously discussed and analysed deviations between model and experiment are factored into future simulations, the model can be deemed as sufficiently accurate to serve its purpose as a fast heat conductive simulation for varying material properties, with a corresponding small-scale and fast experiment.

7 Earth Basket Experiment

As part of the framework of the *GEOFIT* research project, an earth basket experiment and corresponding model was created by the AIT's *GEOFIT* research team. A successful match between the model's solution and the recorded experimental data will validate the exported near-field model-data used by the AIT's *GEOFIT* partners in further far-field modelling, as described previously in chapter two. Additionally, it will further substantiate models of different heat exchanger types, as well as geometrical and material property variations, conducted under similar parameters in this thesis and to which further experimental runs may follow.

7.1 Experiment Setup

In this experiment, the helical shape of an earth basket heat exchanger has been reconstructed by a heating cable with a diameter of 350 mm, a height of 1 m and a loop-pitch of 100 mm, resulting in 10 vertical turns (as seen in Figure 33 and 34 below). This helix has been placed in a container with the following dimensions in mm: $1\,115$ x 720 x $1\,340$ and filled with dry sand. As explained in the previous chapter and displayed in Table 1, multiple probes of the in-situ sand were taken and the sand's material properties like density, thermal conductivity and specific heat capacity were measured in the AIT's laboratory.

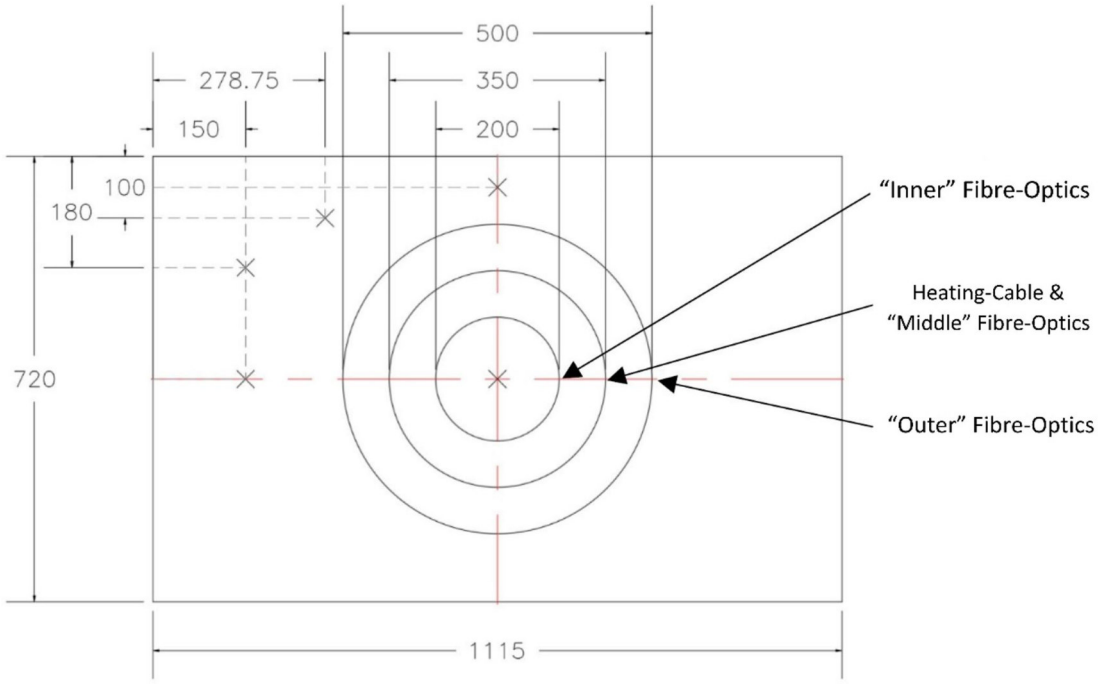

Figure 33: Plan view sketch and dimensions of the earth basket experiment. [1]

[1] AIT Austrian Institute of Technology. (2020). GEOFIT research project

The sensors with which the temperature measurements inside the box have been taken, vary slightly from the ones used in the "Thermo-Pipe" model from the previous chapter. As indicated by the crosses in Figure 33 above and the red dots in Figure 34 below, the same *PT1000* RTD sensors used in the "Thermo-Pipe" experiment were placed around the helix and used for far-field measurements. Six RTD sensors each were placed at the indicated coordinates in Figure 33 with a vertical spacing of 200 mm along the entire height of the heat source.

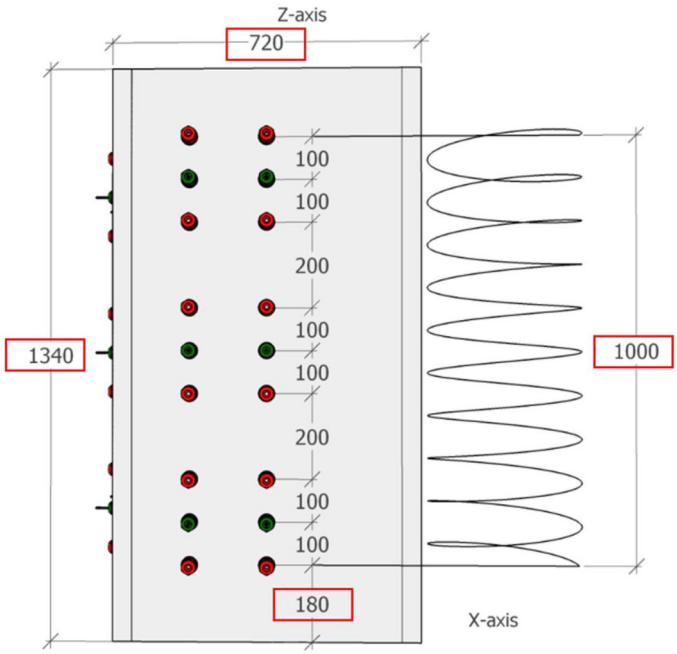

Figure 34: Side view sketch and dimensions of the earth basket experiment. [2]

Additionally to the RTD sensors, helically formed fibre-optic thermometer cables with a resolution of a quarter of a metre were used in the heating cable's vicinity and on the heating cable itself. The fibre-optic cable measuring the temperature of the heat source was named "Middle", while the other two fibre-optic cables with the same loop pitch of 100 mm and a larger and smaller diameter of 500 mm and 200 mm were named "Inner" and "Outer" respectively. The placement of the *PT1000* RTD and helically shaped fibre-optic cable temperature sensors are neatly displayed in Figure 35 below. The RTD sensors indicated in red can be seen mounted onto the inner walls of the box and protrude 50 mm to 150 mm, depending on the position, into the interior of the box. The helical shaped fibre-optic cable thermometers are displayed in green at the centre of the sketch displayed in Figure 35, while the heating cable situated directly next to the "Middle" fibre-optic cable is orange coloured.

This sand filled box, weighing almost two tons, is situated in a cooling chamber, which can accurately regulate the ambient temperature at a constant $10\,°C$. These $10\,°C$ are the boundary and initial conditions. It may take up to three weeks until the entire interior of the box is cooled down to said temperature and all temperature sensors read $10\,°C$. Once the initial condition in the experiment has been reached, the experimental run can be started. Hereby, a constant

[2] AIT Austrian Institute of Technology. (2020). GEOFIT research project

heat input, which has been logged at exactly 113.1 W, is applied to the heating cable and the thermal response at the temperature sensors is recorded. One full experimental run, until steady-state conditions are reached, takes approximately an additional two weeks.

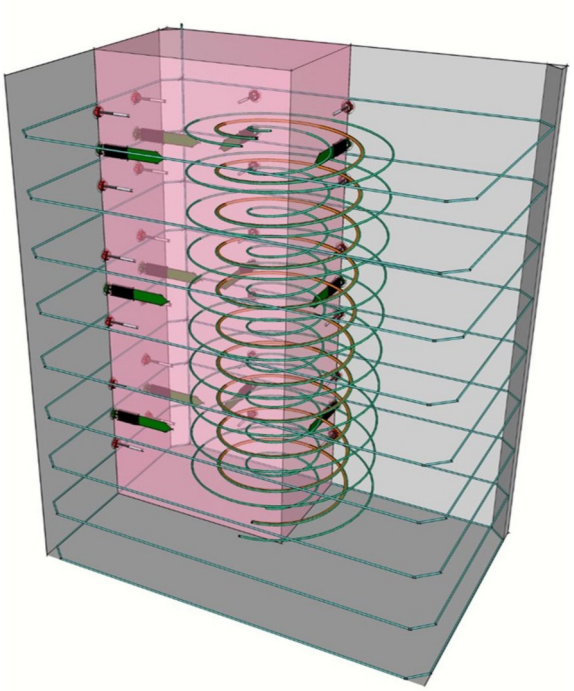

Figure 35: 3D sketch of the earth basket experiment's temperature sensor placement. [3]

7.2 Comparison between Experiment and Model

In Figure 36 below, the experimentally measured temperature (transparent) and the simulated data (bold) at the respective fibre-optic cable sensor positions are plotted against the model's height in z-axis direction at the thermal equilibrium reached at time $t = 788\,000$ s, which approximates to 9 days. As previously explained, the helical fibre-optic cable next to the heat source is denoted as "Middle" and plotted in orange. The other two helical fibre-optic cables, with a radial distance of 75 mm to the heat source, are denoted as "Inner" and "Outer" and plotted in blue and green respectively. Overall, Figure 36 shows a good match between experiment and model. The best fit is at the centre of the model, while a slight deviation towards the boundaries at the top can be observed. This deviation in the upper half of the box may be credited to sand consolidation due to movement of the box. The rectangular shape of the box, in which the earth basket is placed, can be observed at the model's "Outer" fibre-optic temperature sensors. There is a stronger temperature difference between data points placed directly next to each other along the helical path of fibre optic cable, as the distance to the boundaries vary in x and y axis directions. This effect is the strongest on the "Outer" fibre-optic sensors, because the effect of the boundary conditions is stronger, as they are radially placed closer to the boundaries and experience lower temperatures.

[3] AIT Austrian Institute of Technology. (2020). GEOFIT research project

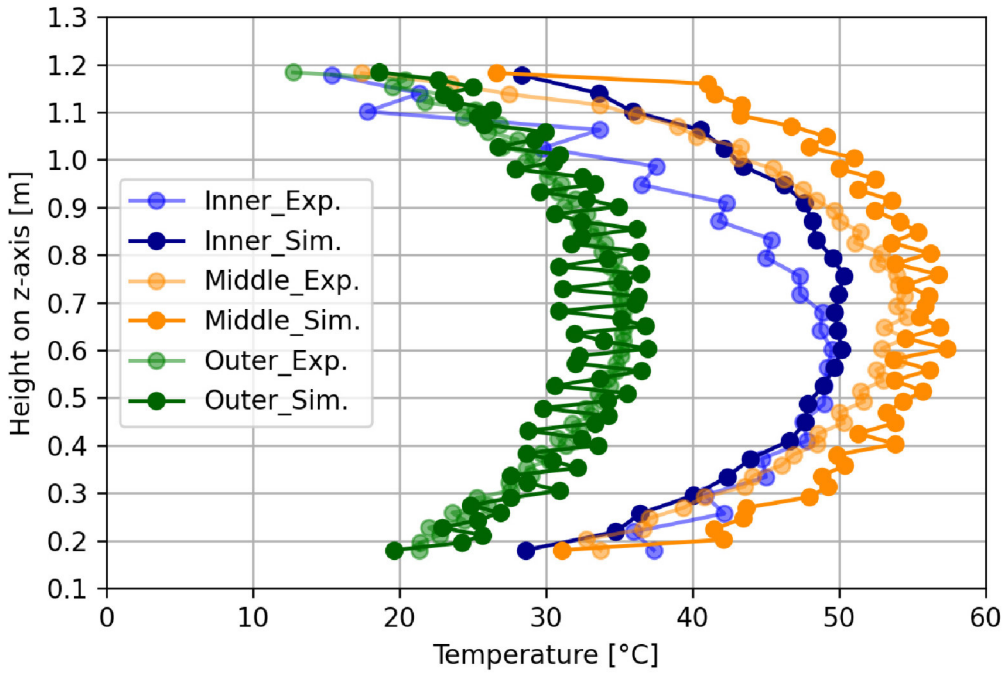

Figure 36: Simulation and experiment results from fibre-optic temperature sensors at steady-state.

Additionally to the fibre-optic temperature sensors in the vicinity of the heat source, model and experiment are further compared at chosen RTD sensor positions in Figure 37 below.

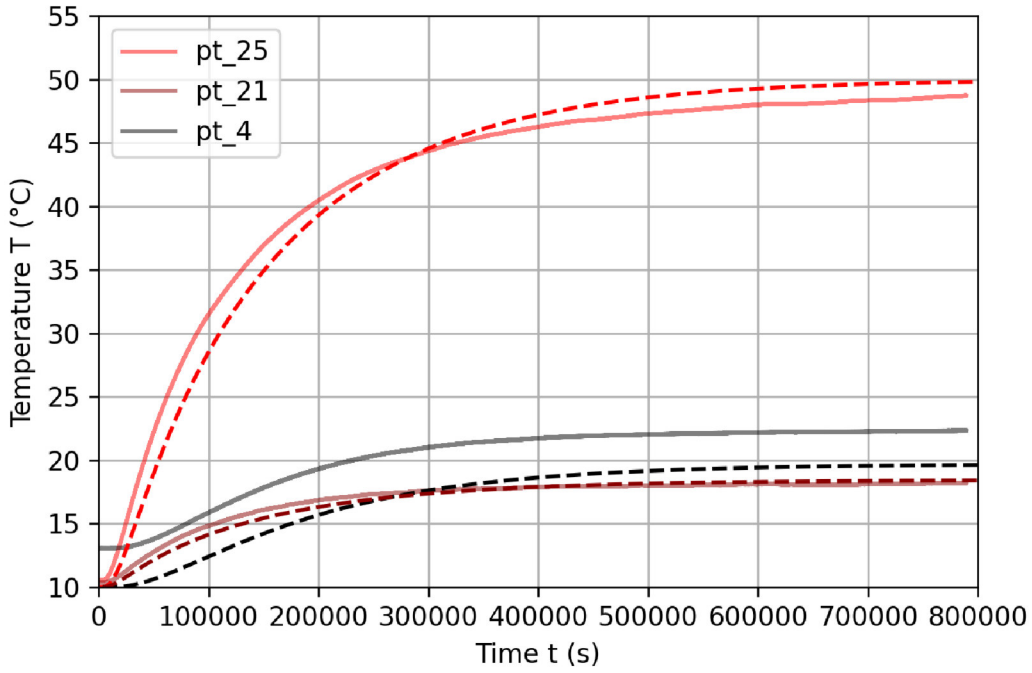

Figure 37: Earth basket simulation (- - -) and experiment (—) at three distinct RTD sensor positions.

For optimal visualisation purposes, three distinct sensor positions were chosen and compared in Figure 37 above. Sensor point "pt-25" is located exactly at the centre of the box, while the other two sensors "pt-4" and "pt-21" are located on the x and y axis respectively, at a medium height. Their exact coordinates are the following in mm: "pt-4" $(0\,|\,-405.5\,|\,580)$, "pt-21" $(-310\,|\,0\,|\,780)$ and "pt-25" $(0\,|\,0\,|\,670)$. Experimentally measured data is plotted in solid lines again, while the simulated results at the corresponding sensor positions are plotted in dashed lines. A rapid temperature increase with passing time can be observed in the early transient stage, while near steady-state conditions are clearly visible after approximately nine days. Initially, the temperature difference at the discussed RTD sensor positions in Figure 36 above seem quite large. However, at time $t = 0$ s a distinct offset at all three sensor positions can be observed. This is due to the fact that in the large experiment, the initial condition of 10 $°C$ has not spread throughout the entire box. In order to accurately compare the simulated results with the measured experimental data, the temperature differences between simulation and experiment at the corresponding sensor positions are plotted against time in Figure 38 below.

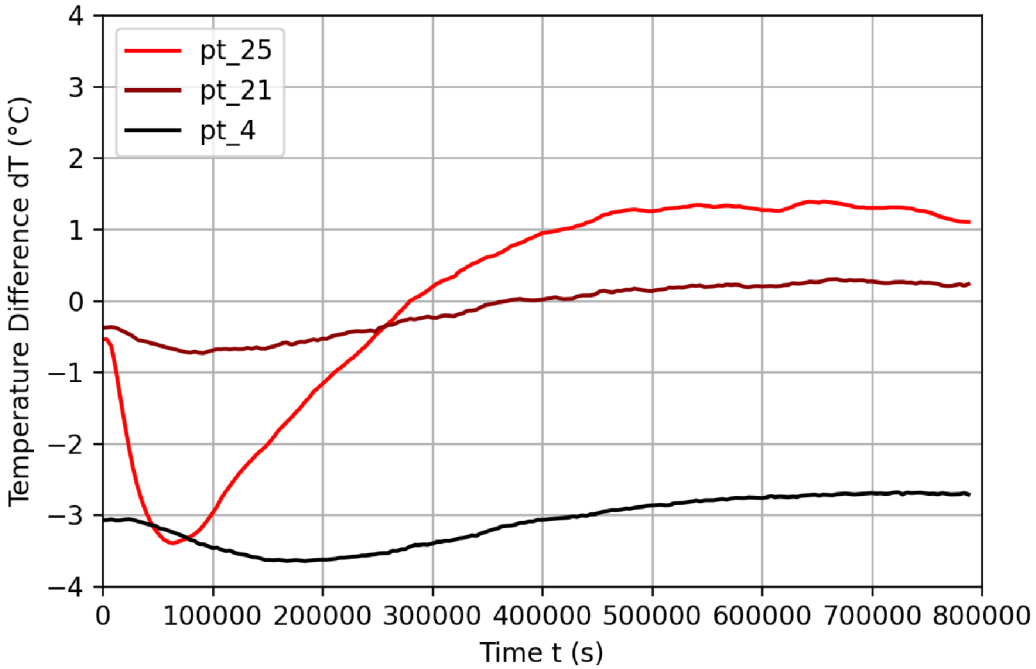

Figure 38: Earth basket temperature difference at three RTD sensor points: simulation – experiment.

The experimentally measured data is subtracted from the simulation's results at the respective sensor locations in Figure 38 above. Now, the initial offset at the model's initial condition is clearly visible. By taking this offset into account, the absolute temperature difference between experiment and simulation at steady-state conditions are a mere 0.36 $°C$ at sensor position "pt-4" and 0.61 $°C$ at "pt-21". The higher deviation between model and experiment at sensor location "pt-25" during the early transient stage can be attributed to the steep temperature increase at the centre of the model (see Figure 37 above). By taking these relatively high

absolute temperatures at the centre of the box into account, a deviation of $1.5\ ^{\circ}C$ at steady-state conditions can still be deemed as accurate. Furthermore, as depicted in Figure 37 above, the rate of the temperature increase during the transient period shows a very good match between model and experiment. This is an indication that the thermal diffusivity and therefore the relation between the measured material properties of the heat conducting medium sand are accurate and representative of the experiment's in-situ conditions.

In the following chapters models with varying geometries and material properties, but similar setups regarding inputs like initial and boundary conditions, solver and mesher settings, model volume, heat input, etc. will be presented and their results discussed. These results are substantiated by the good match of the comparison between the AIT's earth basket experiment and the corresponding simulation previously discussed.

8 Double Earth Basket Model

In the following chapter a geometric variation of the previously discussed earth basket model is presented. Hereby two helical heat sources are placed side by side in a box with the same dimensions as the single earth basket model and their effect on each other will be studied. Additionally, the model's heat conducting medium is varied with measured material properties of sands and soils and the results are compared.

8.1 Model Setup

The model has the same dimensions as the previous earth basket model in order to provide a basis for an accurate comparison between the two and to additionally create the possibility of performing a corresponding experiment with the AIT's resources and facilities in place. As previously stated, the rectangular box has the dimensions $1\,115$ x 720 x $1\,340$ in mm while the two helical heat sources are identical in shape. They possess a cable diameter of 6 mm, a helix diameter of 350 mm with a loop pitch of 100 mm, which results in 10 turns over a vertical height of $1\,000$ mm. As seen in Figure 39 below, the two helical heat sources are evenly spaced along the model's y-axis at a distance equal to their radius.

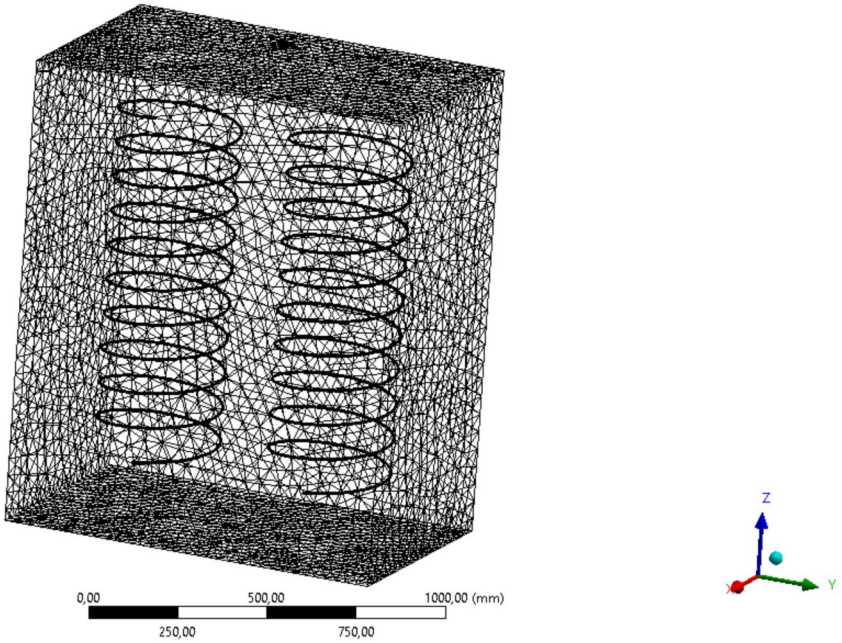

Figure 39: Helical heat source placement and geometry of the double earth basket model.

The mesh consists out of $1\,964\,925$ elements with a minimal element size of 1.85 mm on the heating coil's surface and a maximum element size of 50 mm on the walls of the box (see Figures 40 and 41 below). The growth rate of the elements or cells has been limited to a factor of 1.9. These settings create a sufficiently accurate mesh with a high resolution on

the surface of the thin heating cables, between the cables' helical turns and between the two separate helices as well. Additionally, the specified maximum growth rate and larger element sizes on the model's outer boundaries ensure a manageable mesh size without compromising accuracy.

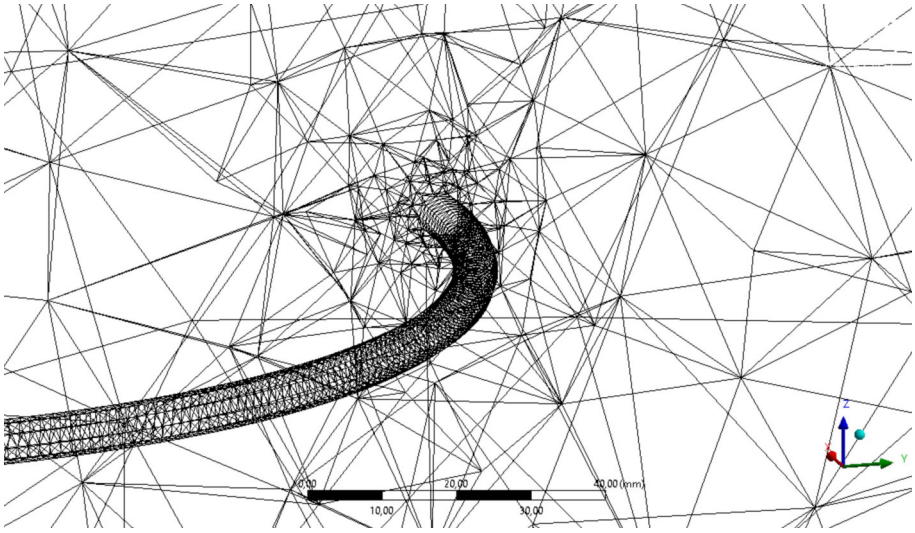

Figure 40: Close-up of the heating cable's surface meshing in the double earth basket model.

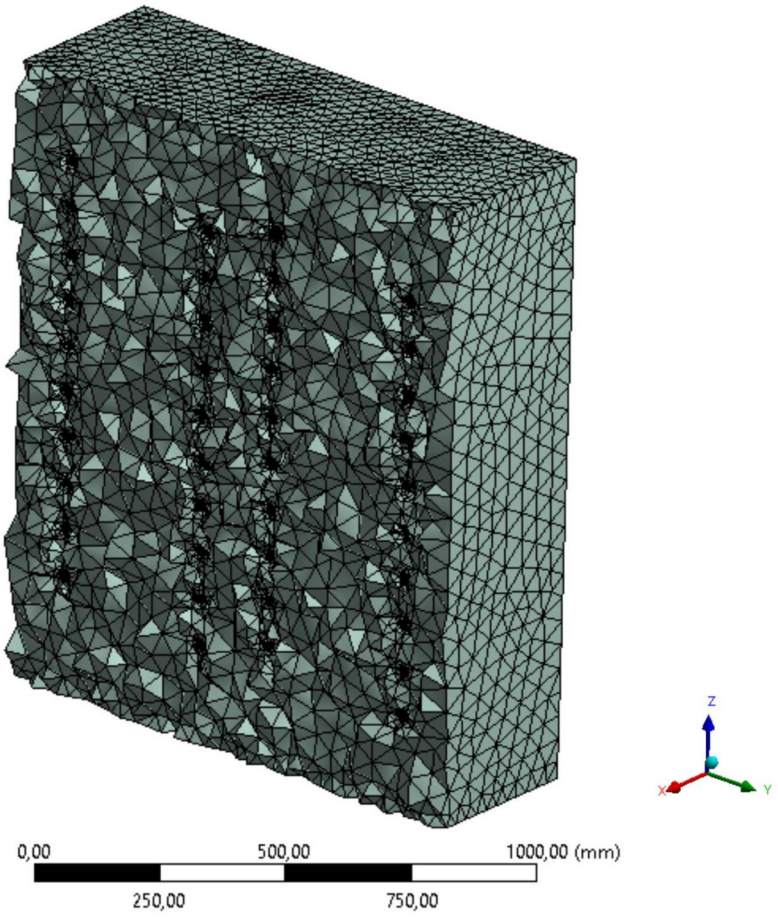

Figure 41: Cross-section (yz-plane) of the double earth basket model's tetrahedral and triangular mesh.

As shown in Figure 41 above, the model consists out of tetrahedral elements in the body's three dimensional volume space and triangular elements on the body's two dimensional surfaces, which are namely the six walls of the box as well as the heating cables' surfaces. Figure 42 below shows an enlarged view of the mesh in the heating cable's vicinity. The gradual increase in element size through the growth factor is visualised here.

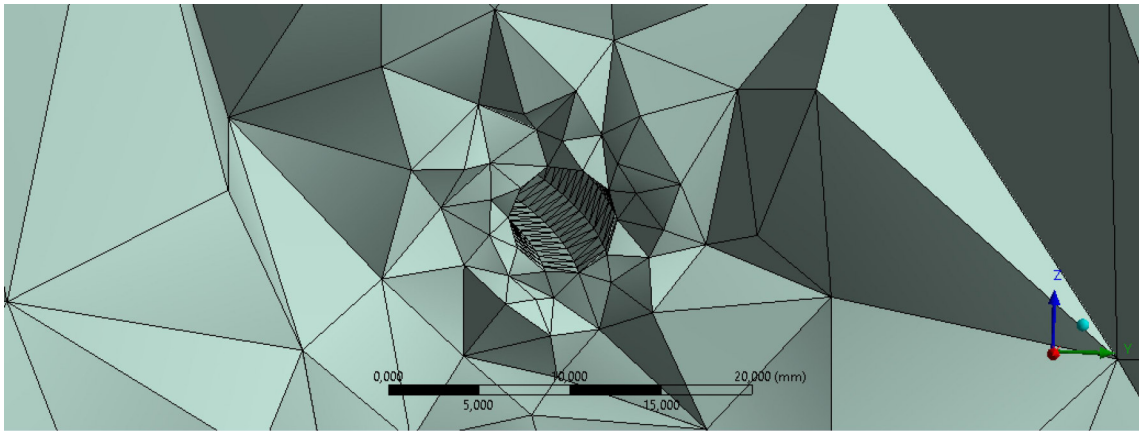

Figure 42: Close-up of the double earth basket model's cell structure at the heating cable.

Similar to the single earth basket model discussed in the previous chapter, a boundary condition of a constant $10\ °C$ is applied to all walls of the box. The same temperature is applied as an initial condition throughout the model. Then, a constant heat input is applied to both heating cable's surfaces, which are also defined as walls in the model. In order to accurately compare the single earth basket model with the double earth basket model, the total heat input into the model remains the same as well, as the dimensions of the model have not changed. This means a constant heat input of 113.1 W into the model or 56.55 W on each heating cable's mantle surface. The time-step size of $1\,000$ s is still sufficiently accurate for this model as well, with 50 iterations per time-step. After $1\,500$ time-steps, steady-state conditions have been reached, with the the total heat flux flowing from the heating cable to the model's walls measured at -113.098 W and therefore matching the heat input.

Figure 43 below depicts the static temperature distribution in the yz-plane as well as on the two helical heating cables after $1\,500$ time-steps, at steady-state conditions. This figure serves as a visualisation purpose to indicate the position and shape of the helical heat sources, which may no longer be depicted in further plane-view contour plots. The temperature range in the contour plot from Figure 43 below ranges from the initial condition of 283.15 K to the maximum temperature reached at the heat source during steady-state conditions, which is 315.78 K in this case. In the following sections contour plots taken during different time-steps or even different models will be compared. These are always plotted against the same specified maximum temperature, in order to enable a meaningful qualitative comparison between the individual models and time-steps.

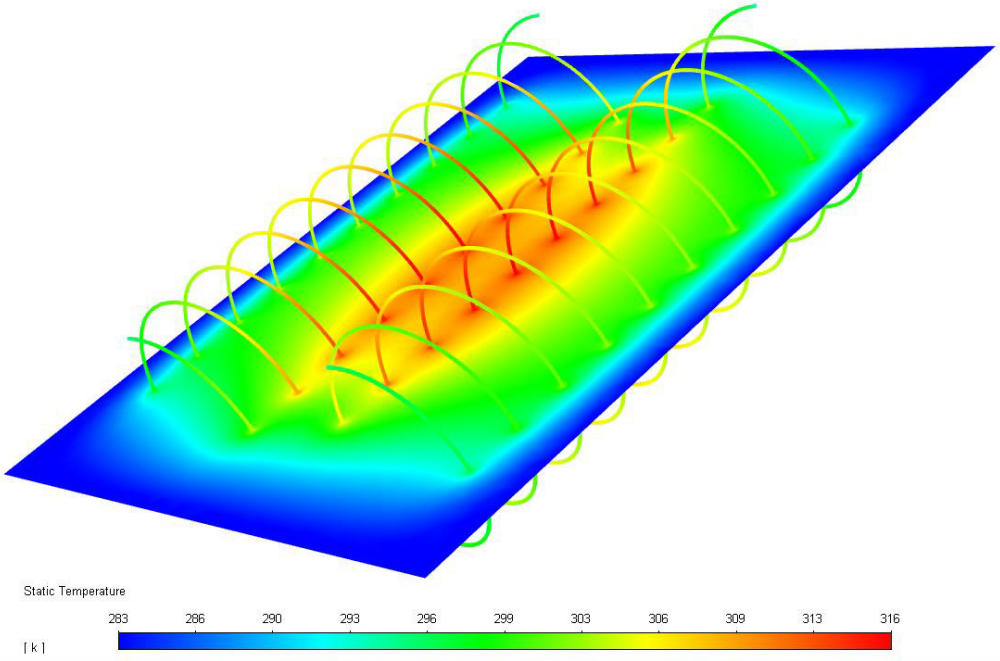

Figure 43: Contour plot depicting the temperature of the earth basket model at steady-state.

8.2 Results

In Figure 44 below, smooth contour plots of the model's cross-sectional yz-plane are displayed at four different time-steps. For better visualisation purposes, the protruding helical heating cables have been projected onto the yz-plane, similarly to the previous Figure 43 above. Once the heat input of 113.1 W is applied to the mantle surface of the heating cables, their surfaces begin to heat up and possess a higher temperature than the medium which surrounds them. This is still clearly visible after 13.3 hours at the protruding heating cables' surfaces (see Figure 44a below). In the cross-section of the yz-plane the radial heat conduction from the heating cables through the surrounding medium sand is visible as well. This results in a gradual temperature increase of approximately $10\ ^{\circ}C$ after 13.3 hours between the cable's helical turns and the two neighbouring earth baskets. Taking a closer look at Figure 44b and doubling the passed time to approximately 26.6 hours, the distinct shape of the maximum temperature field at steady-state conditions is already beginning to form. Approximately doubling the passed time to 2.3 days again, the temperature is beginning to uniformly increase between the two earth baskets, as well as inside the individual helices (see Figure 44c below). After $t = 800\,000$ s, which is approximately 9.3 days, the total heat transfer through the model is measured at -113.096 W and thus sufficient near steady-steady state conditions have been reached. This means that the temperature increase with time has diminished to the second decimal order and is visually undetectable in the static temperature contour plots. In Figure 44d below, the final maximum temperature distribution at steady-state conditions is visualised. The distinct oval shape of the high temperature zone is directly dependent on the shape of the heat source and will be further discussed during the comparison with other geometric heat exchanger variations in the following section.

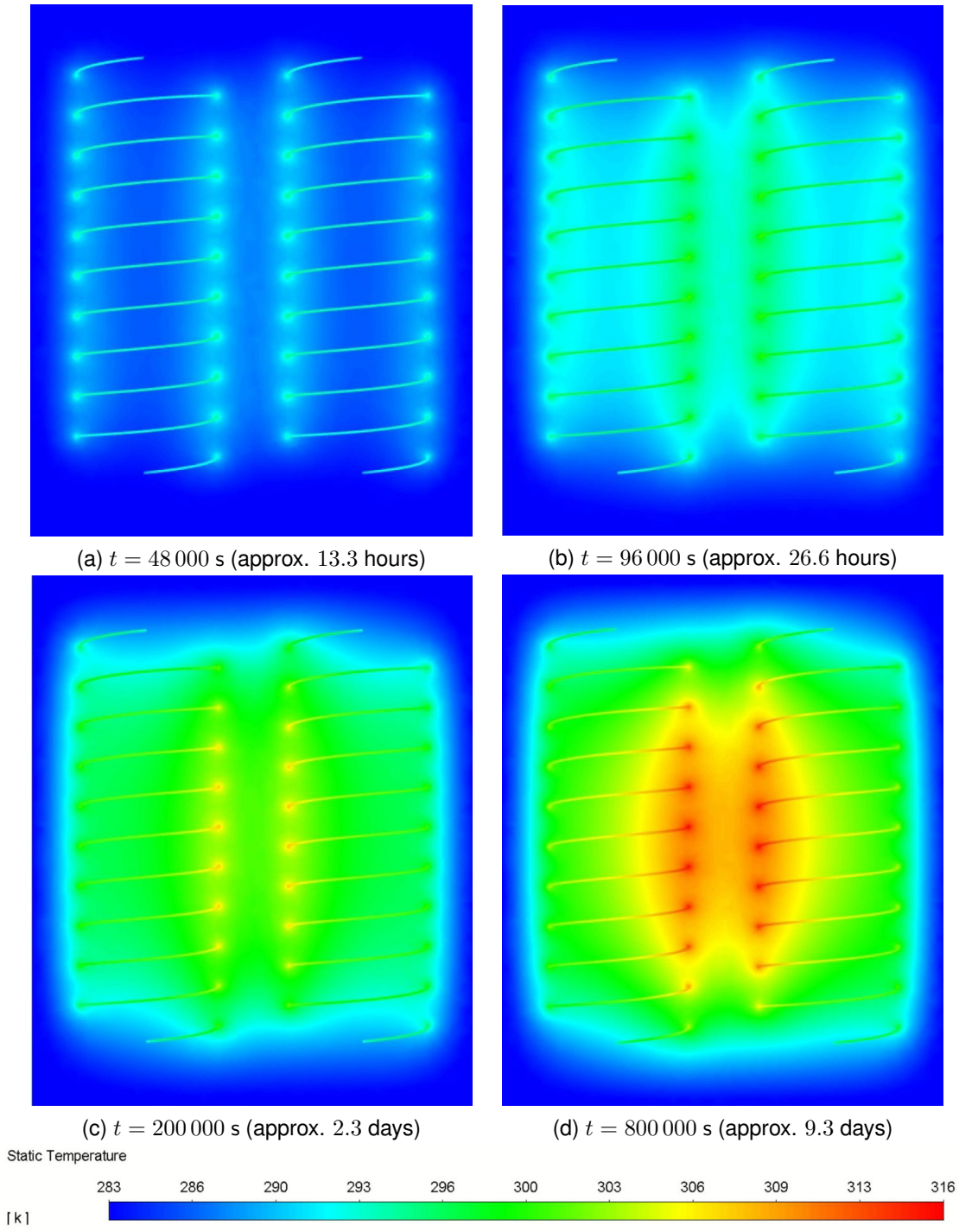

(a) $t = 48\,000$ s (approx. 13.3 hours)

(b) $t = 96\,000$ s (approx. 26.6 hours)

(c) $t = 200\,000$ s (approx. 2.3 days)

(d) $t = 800\,000$ s (approx. 9.3 days)

Figure 44: Double earth basket model contour plots in the yz-plane from transient to steady-state.

In Figure 45 below, the double earth basket model's cross-section in the xz-plane is visualised at the same time-steps as in Figure 44 above. The distinct difference to the yz-plane projection lies in the double earth basket model's geometry, as one full earth basket is now projected onto the xz-plane, while the second earth basket is not visible, as it is positioned behind the cross-sectional plane. The plane therefore has no intersections with the heating cable, as it passes through the centre of the space situated between the two earth baskets visible in Figure 44

above.

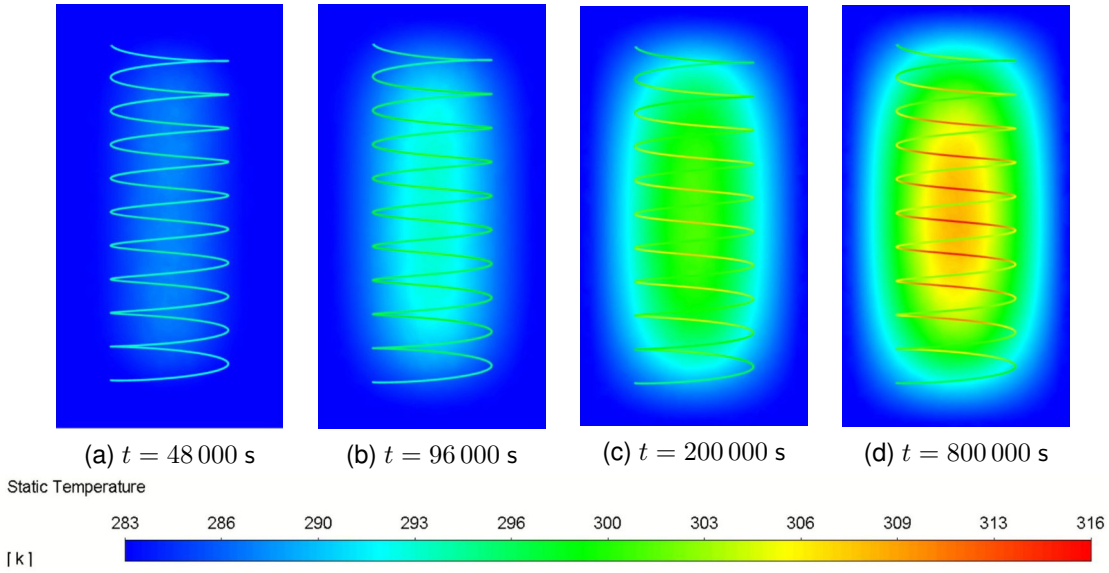

Figure 45: Double earth basket model contour plots in the xz-plane from transient to steady-state.

8.3 Material Parameter Variation

Two further simulation runs have been performed with varying substrates. For the first material parameter variation, moisture has been added to the same type of sand which has been used in the previously presented experiments and simulations and whose material parameters have been listed in Table 1. The moisture content and the resulting change in material parameters have been measured by the AIT's laboratory with the same procedures as previously explained. A measured moisture content of 6.18 % resulted in the following material's thermal conductivity, specific heat capacity and density listed in Table 3 below.

The measured material parameters are all in accordance with literature values (Männer, 2012). Additionally, the change in thermal conductivity, specific heat capacity and density of the two additional measured substrates moist sand and humus soil show expected trends. The density of the moist sand increased in comparison to its dry counterpart, as denser water has replaced some air in its pore space. This increased water content also leads to a significant increase in thermal conductivity, as explained by Männer (2012). Coarser grained soil with a high content in irregularly shaped organic matter has a significant lower density than sand. Interestingly, the trend of increasing thermal conductivity with increasing temperature is reversed for humus soil (see Table 4 below), but according to Männer (2012) this phenomenon is supported by existing literature as well.

Table 3: Mean values from AIT probe measurements of sand with a moisture content of 6.18 %.

Mean Material Property Values of Moist Sand Probes			
Temperature (°C)	λ (W m^{-1} K^{-1})	c_p (J g^{-1} K^{-1})	ρ (g cm^{-3})
-10	1.2435	1.070	1.9279
0	0.9788	x-x-x	1.9279
10	0.9514	1.095	1.9279
20	0.9339	1.152	1.9279
25	0.9619	1.100	1.9279
30	0.9728	1.116	1.9279
40	1.09	1.134	1.9279
50	1.19	1.139	1.9279
60	1.31	1.184	1.9279
70	1.46	1.295	1.9279

As a third heat conducting medium conventional dry garden humus soil with the following material parameters listed in Table 4 has been used. Just as before, the mean values from multiple measurement runs conducted by the AIT's engineers have been listed in Table 3 and 4, while all measurement runs and their statistical analysis can be found Appendix C as well. The temperature dependence of the thermal conductivity λ and the specific heat capacity c_p are integrated into the model as well, while the density ρ is constant again.

Table 4: Mean values from AIT probe measurements of dry humus soil.

Mean Material Property Values of Dry Humus Soil Probes			
Temperature (°C)	λ (W m^{-1} K^{-1})	c_p (J g^{-1} K^{-1})	ρ (g cm^{-3})
-10	0.3401	0.913	1.6424
0	0.3370	0.966	1.6424
10	0.3251	0.974	1.6424
20	0.3162	1.006	1.6424
25	0.3121	x-x-x	1.6424
30	0.3068	1.056	1.6424
40	0.2991	1.086	1.6424
50	0.3058	1.085	1.6424
60	0.3024	1.072	1.6424
70	0.2972	1.106	1.6424

In Figure 46 below, the model's temperatures at full steady-state conditions after approximately two and a half weeks ($t = 1\,500\,000$ s) for the three different materials dry sand, moist sand and dry humus soil have been compared. It should be noted that the colour map legend has changed, compared to previous figures, due to the increased maximum temperature in the simulation run with humus soil as a heat conducting medium. Therefore, the other two contour plots have been plotted relative to said new maximum temperature of 324 K. As ex-

pected, the maximum temperature of the moist sand with 297 K is the lowest, followed by the same sand without moisture content with 316 K.

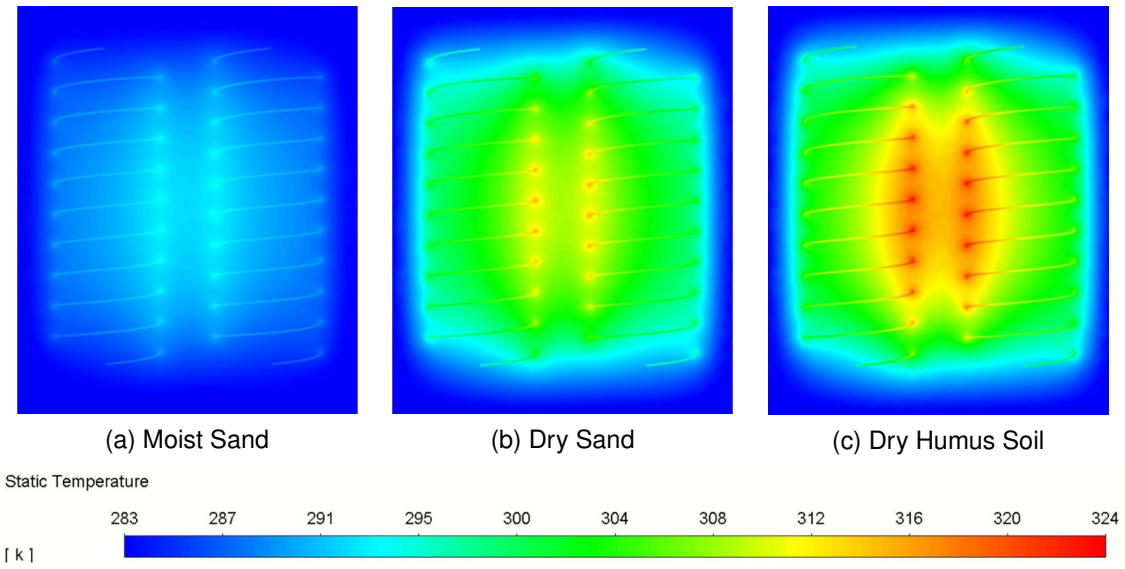

Figure 46: Double earth basket model temperature contour plots of different materials (steady-state).

As previously explained and derived during the calculation of the analytical solution of the rod model in chapter five, the steady-state solution depicted in Eq. (23) is responsible for the model's maximum temperature. The only material property appearing in the steady-state solution is the thermal conductivity and it is inversely proportional to the temperature. As the the thermal conductivity increases with rising water content, the maximum temperature of the moist sand (see Table 1 & 3) will be lower than the corresponding simulation run with the same type of sand but without water content. In return the significantly lower thermal conductivity of conventional garden humus soil, depicted in Table 4 above, causes a maximum temperature increase of approximately $8\ ^{\circ}C$.

In order to visually display the effect that the change of the heat conducting medium has on the transient solution, the models' colour map legends are plotted relative to the individual model's maximum temperature. This means that in Figure 47 below, the static temperature contour plots taken at the early transient stage at approximately 26.7 hours ($t = 96\,000$ s) are all showing temperature legends to their left, that depict each model's maximum temperature at steady-state conditions. Through that the speed, at which the double earth basket model with the respective heat conducting medium reaches steady-state conditions, can be neatly visualised. After approximately 26.7 hours the model with moist sand (see Figure 47a) is much closer to steady-state conditions than the models with the other two materials. Analogically dry humus soil depicted in Figure 47c takes the longest to reach steady-state conditions. As previously shown in chapter five, the thermal diffusivity α in the transient solution displayed in Eq. (71) is responsible for the time it takes to reach steady-state conditions (see Table 5 below). The moist sand has the highest average thermal diffusivity of $45.23 \cdot 10^{-4}$ $\mathrm{cm}^2\,\mathrm{s}^{-1}$ at

a temperature of $30\ °C$, while humus soil has the lowest with $17.69 \cdot 10^{-4}$ cm^2 s^{-1}.

Table 5: Calculated thermal diffusivity from mean values of AIT measurements of sand and humus soil.

Mean Thermal Diffusivity Values for varying Materials and Temperatures			
Temperature (°C)	α Moist Sand (10^{-4} cm^2 s^{-1})	α Dry Sand (10^{-4} cm^2 s^{-1})	α Dry Humus (10^{-4} cm^2 s^{-1})
-10	60.31	23.52	22.67
0	x-x-x	21.93	21.24
10	45.09	22.13	20.33
20	42.06	21.91	19.14
25	45.34	x-x-x	x-x-x
30	45.23	21.58	17.69
40	50.1	20.82	16.77
50	54.1	20.17	17.16
60	57.2	20.78	17.18
70	58.4	20.03	16.36

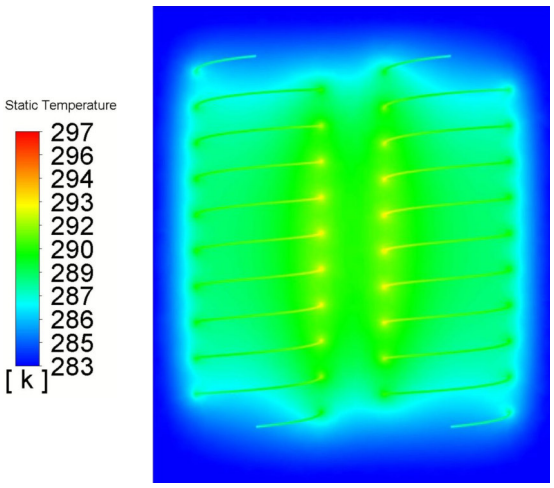

(a) Moist Sand

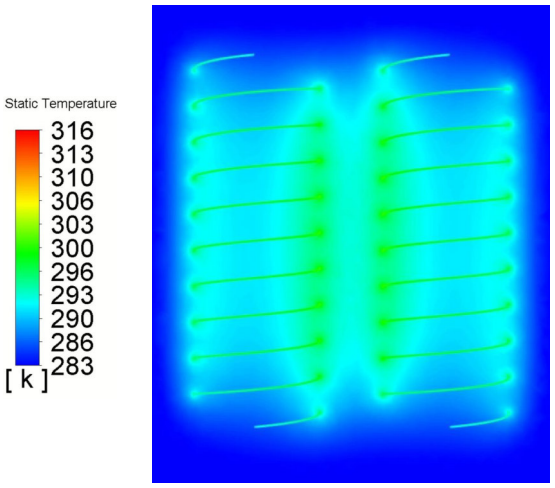

(b) Dry Sand

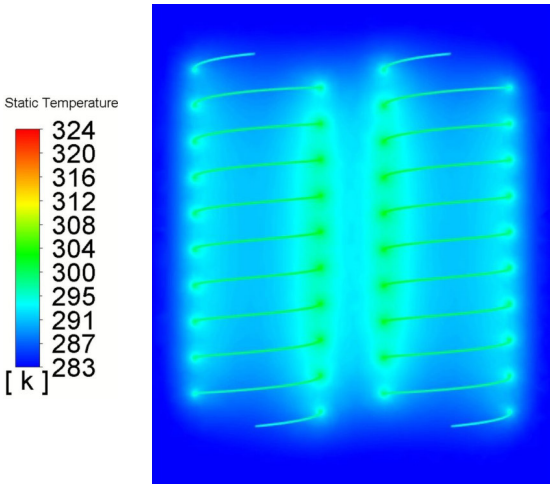

(c) Dry Humus Soil

Figure 47: Double earth basket model temperature contour plots of different materials at $t = 96\,000$ s (scaled to individual models' maximum temperature at thermal equilibrium).

While disregarding the further far-field modelling that is necessary to fully quantify the thermal behaviour of heat exchangers in varying substrates, some conclusions for realistic applications can already be drawn from the near-field models. Substrates with a higher bulk density, like consolidated sand, and a significant moisture or water content are better thermal conductors than unconsolidated dry substrates with a high content of irregularly shaped organic matter. Additionally, the thermal equilibrium in such consolidated substrates with a high moisture content is reached significantly faster as well. However, convective heat transport may play a large role in the far-field heat transport in poorly consolidated substrates with high moisture contents. Therefore, this will be separately investigated by the AIT's *GEOFIT* project partners, responsible for far-field modelling.

8.4 Comparison to Single Earth Basket Model

In the following section the double earth basket configuration will be compared to the AIT's pre-existing single earth basket model. In Figure 48 below, these two models are depicted in the yz-plane at steady-state conditions after 800 time-steps, which approximates to 9.3 days. The single earth basket model is shown in Figure 48a on the left, while the double earth basket model is depicted on the right-hand-side in Figure 48b.

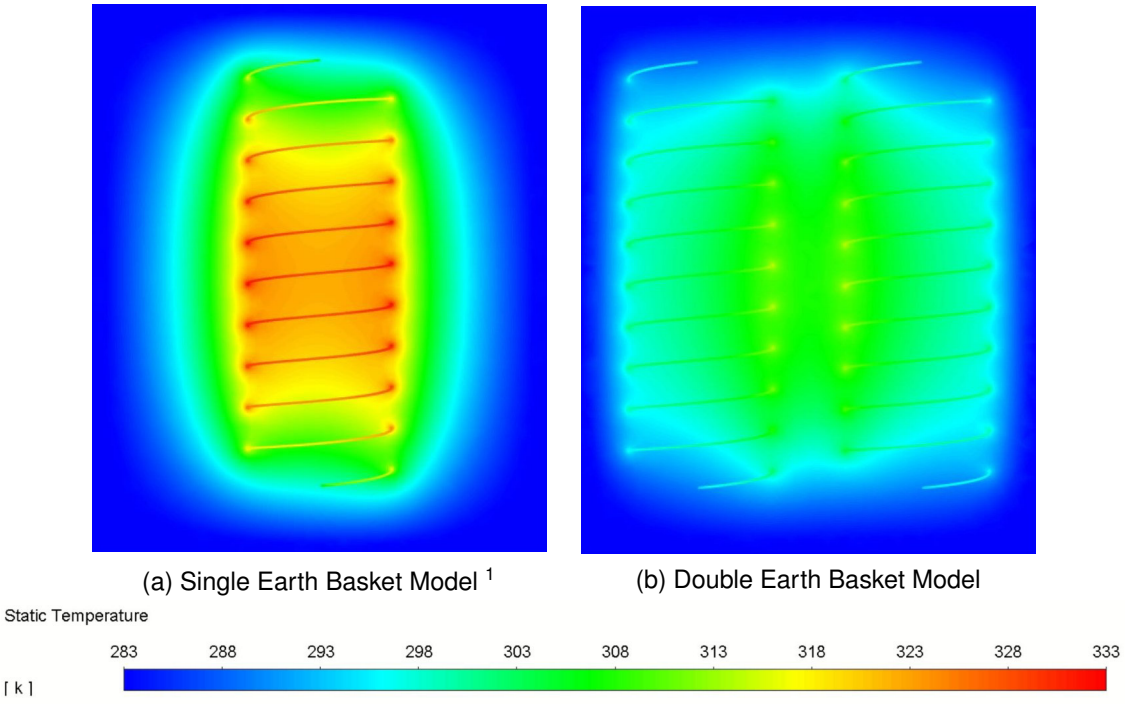

(a) Single Earth Basket Model [1] (b) Double Earth Basket Model

Figure 48: Comparison between single and double earth basket model at steady-state in the yz-plane.

[1] Steurer, A. (2020). GEOFIT research project - CFD modelling. Austrian Institute of Technology

To make a qualitative comparison possible, the two models have been set up in the same control volume with the same material properties of dry sand, who's measurements have been previously displayed in Table 1. The heat input in these control volumes, as well as the external parameters like boundary and initial conditions are identical. The single earth basket model displayed in Figure 48a above reaches significantly higher temperatures at steady-state, with a maximum temperature of 333 K compared to the 316 K of the double earth basket model displayed in Figure 48b, at identical heat input and material parameter values. Even when taking the closer distance of the two helical heat sources from Figure 48b to the model's boundaries into consideration, the temperature distribution at the centre of the two models significantly differ in magnitude and shape. This was expected, as the heat exchanger's surface area is effectively doubled. On the one hand, this indicates that heat can be transferred away from the heating cable effectively, without stagnant temperature build-ups in the centre of model, as seen in the single earth basket model in Figure 48a. A good heat transport from the model's heat source throughout the control volume is usually desirable, as it indicates a good geometric efficiency of the respective heat exchanger's design. However, as the two earth baskets in Figure 48b above act as separate units, the depicted temperature field also indicates that the two earth baskets drastically influence each other at a distance equal to one earth basket's radial length. Therefore, the fact that twice as many loops have been used in the heat exchanger model displayed in Figure 48b and thus twice as much material is needed has to be kept in mind. The best practice of spacing earth baskets several diameters apart, to ensure no significant influence on the adjacent earth basket's temperature field, should always be adopted. This aspect no longer plays a role in the comparison to the horizontal slinky heat exchanger in the upcoming chapter, as both models possess a comparable amount of loops.

9 Horizontal Slinky Heat Exchanger Model

Additionally to the vertical earth basket heat exchanger, a model of a section of a horizontal slinky heat exchanger has been created and is presented in the following chapter. The results will be compared to the heat exchanger geometries discussed in the previous chapters.

9.1 Model Setup

In order to ensure a meaningful and qualitative comparison between the horizontal slinky heat exchanger model and the earth basket model, quantities like the overall volume of the body, diameters of the heating cable and slinky coils, total heat input and meshing parameters were kept constant to the previously discussed models and have been described in the previous chapter. Due to the horizontal slinky heat exchanger's geometric nature, the height of the box has been halved and its length doubled. This results in the same control volume with the new box dimensions $2\,230$ x 720 x 670 in mm. In Figures 49 and 50 the model's side and top view are displayed, in which nine horizontally spaced and on one side connected loops at the centre of the previously described box are visible.

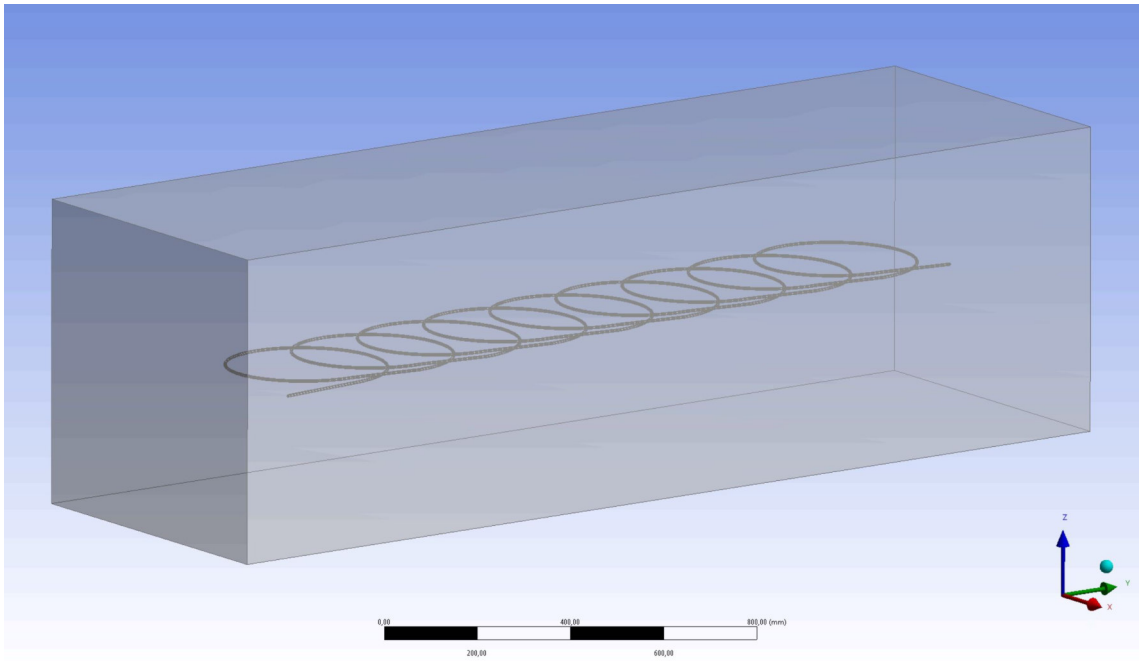

Figure 49: 3D sketch of the horizontal slinky heat exchanger model.

As previously discussed in chapter three, horizontal slinky heat exchangers consist of horizontally spaced helical loops, which usually overlap each other in order to maximise the surface contact with the ground. This overlap is called the loop pitch in this case and is the horizontal distance between two neighbouring loops measured from the same relative position on each ring. As shown in the plane view sketch of the model in Figure 50 below, a common loop pitch

equal to the helical radius of 175 mm was chosen for the horizontal slinky heat exchanger model. This results in an overlap of exactly half a loop. Analogically, doubling the loop pitch to the helical diameter would result in the loops lying adjacent to each other with no overlap at all.

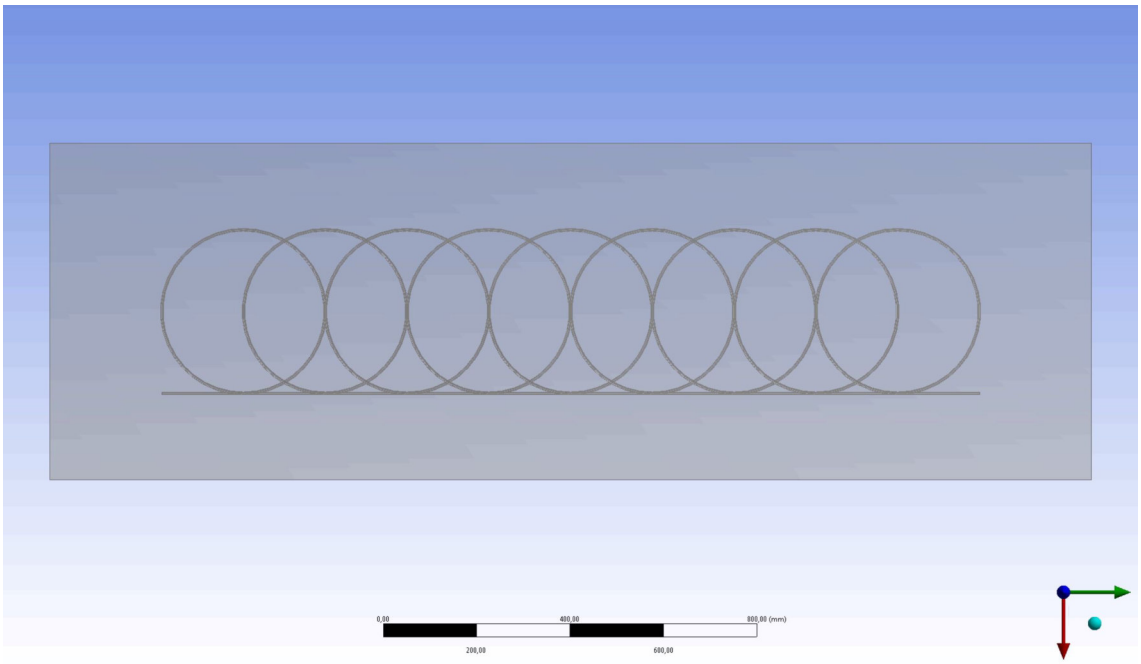

Figure 50: Plane view sketch of the horizontal slinky heat exchanger model.

To ensure good mesh quality at the adjacent points of neighbouring loops, a vertical spacing of 6 mm – which is equal to the heating cable's diameter – was chosen to separate the individual loops lying on top of each other (see Figure 51 below). This is agreeable with industry standards, as it is best practice to avoid surface contact between adjacent loops with small vertical spacers, in order to minimise the influence of the marginally colder working fluid from the previous loop onto the current loop. The close spacing of the heating cable's loops also has an effect on the mesh size, as smaller and thus more cells between the heating cable's loops are required. This leads to more than double the mesh size with $4\,484\,675$ tetrahedral volume and triangular surface elements, compared to the previously discussed double earth basket model. The mesher's settings of a minimal element size of 1.85 mm on the cable's surface and a maximum mesh size of 50 mm on the surface of the box with a maximum growth factor of 1.9 has been kept constant to the previously presented models. Similarly, the boundary conditions applied to the walls of the box and the initial condition remain equal to $10\ °C$, while a constant heat input of 113.1 W has been applied to the heating cable's mantle surface.

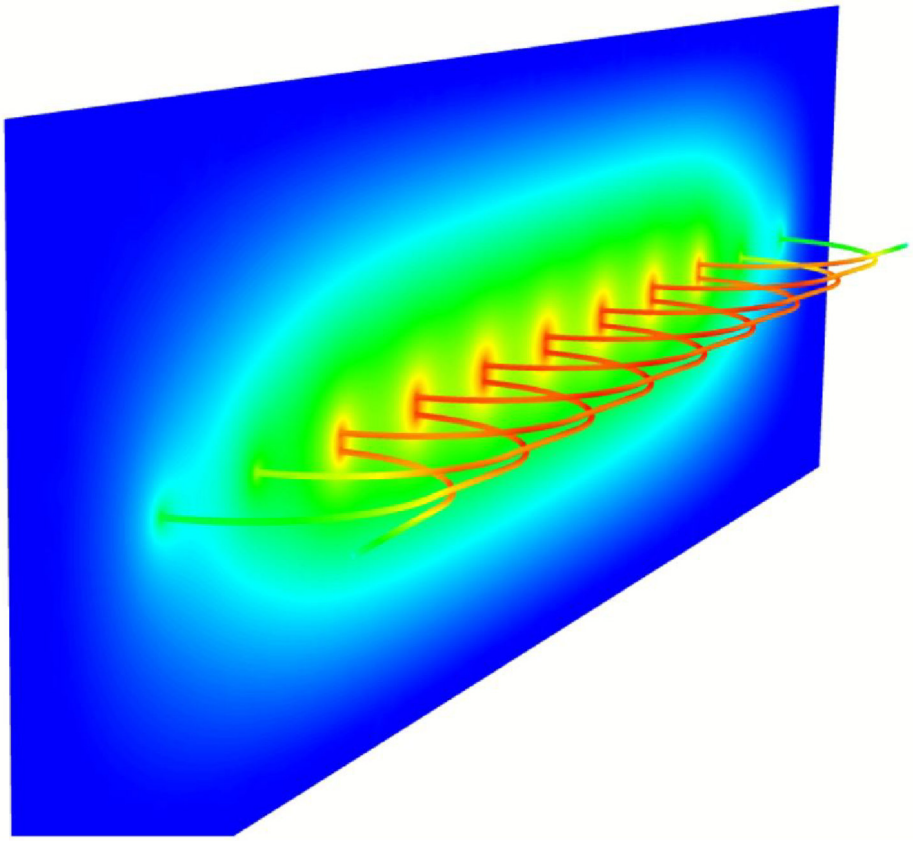

(a) 3D contour plot of the heating cable in the yz-plane.

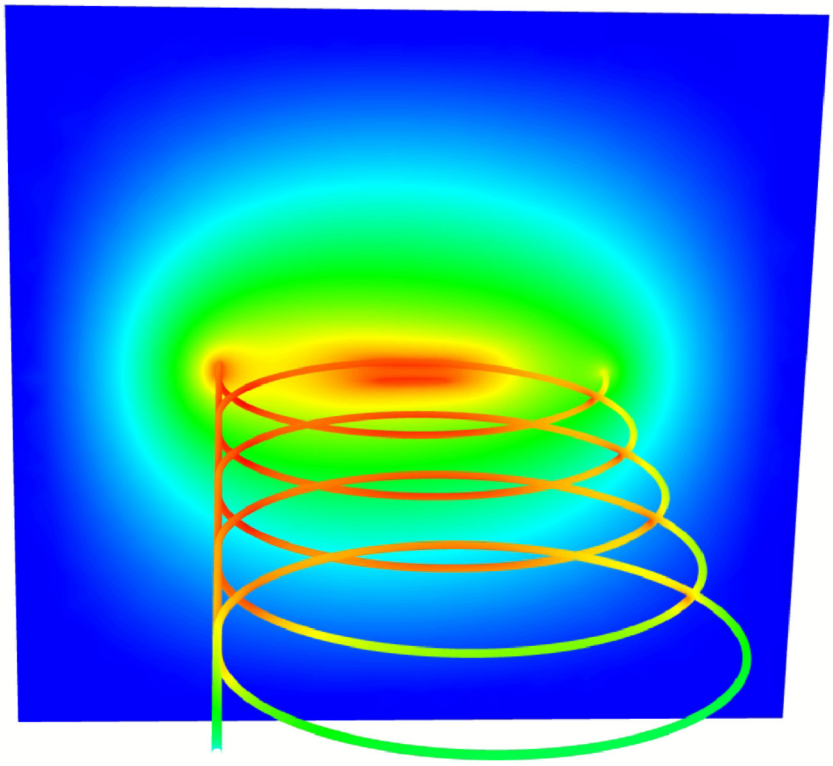

(b) 3D contour plot of the heating cable in the xz-plane.

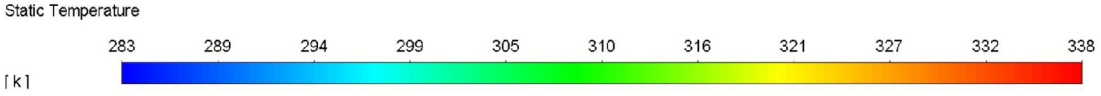

Figure 51: 3D contour plots depicting the temperature of the horizontal slinky model at steady-state.

Figure 51 above displays three dimensional views of the horizontal slinky heat exchanger model. Both are taken at steady-state condition and subsequently scaled to the maximum temperature of 338 K reached at the thermal equilibrium. A cross-section of the temperature distribution in the model's yz-plane is depicted in Figure 51a. The vertically uniform temperature distribution and the vertical spacing between adjacent loops equal to one heating cable's diameter with 6 mm is visualised here. On the other hand, the temperature distribution at steady-state in the cross-sectional xz-plane is depicted in Figure 51b above. The non uniform horizontal distribution, due to the horizontal slinky heat exchanger's geometric configuration, is visualised here. These aspects of the horizontal slinky heat exchanger's temperature distribution will be discussed in the further detail in the following sections.

9.2 Results

In Figure 52 below, temperature contour plots at different time-steps from transient to steady-state conditions of the cross-section through the model in the horizontal xy-plane are depicted. The maximum temperature reached at steady-state conditions is 338 K. These maximum temperatures develop as expected on one side of the heat exchanger, where the adjacent loops connect and at the overlaps, even with a vertical spacing of one coil diameter. The geometric asymmetry of the horizontal slinky heat exchanger is also clearly visible in the temperature field around the heating cables in the xy-plane, whereby a temperature difference of $10\ °C$ between the two inner sides of heat exchanger can be detected in Figure 52d. The heating cable's surface temperature is almost doubled in value between the sides with and without connections. Similarly to the previously discussed model, sufficient steady-state conditions with no change in temperature up to the first decimal point have been achieved after 800 time-steps, which approximates to 9.3 days (see Figure 52d below).

In the following Figure 53 below, temperature contour plots at the same time-steps of the vertical cross-section in the yz-plane are depicted. They will be discussed in further detail on the following page. Similarly to the temperature contour plots from the previous chapter, the heating cable and its temperature have been projected onto the cross-sectional yz-plane in order to indicate and visualise its position. The actual intersections of the helical loops are indicated by the radial temperature increase in the xy-plane, visible during the early transient stage in Figure 53a above. This radial heat conduction can be observed in the early transient stage in Figure 53a and begins to form a uniform temperature field of 310 K between the heat exchanger's individual loops after approximately 26.6 hours in Figure 53b. At steady-state conditions in Figure 53d this increased temperature field has fully expanded.

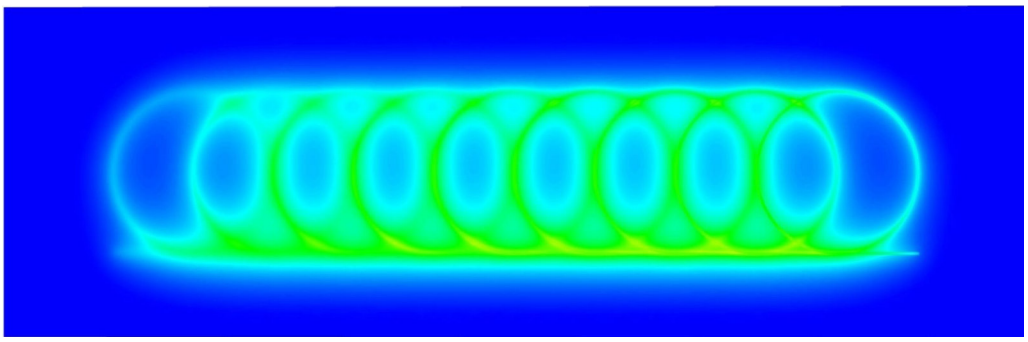

(a) $t = 48\,000$ s (approx. 13.3 hours)

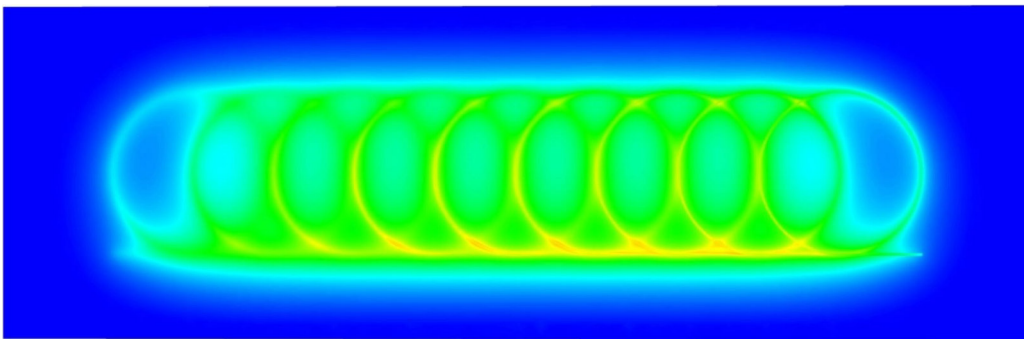

(b) $t = 96\,000$ s (approx. 26.6 hours)

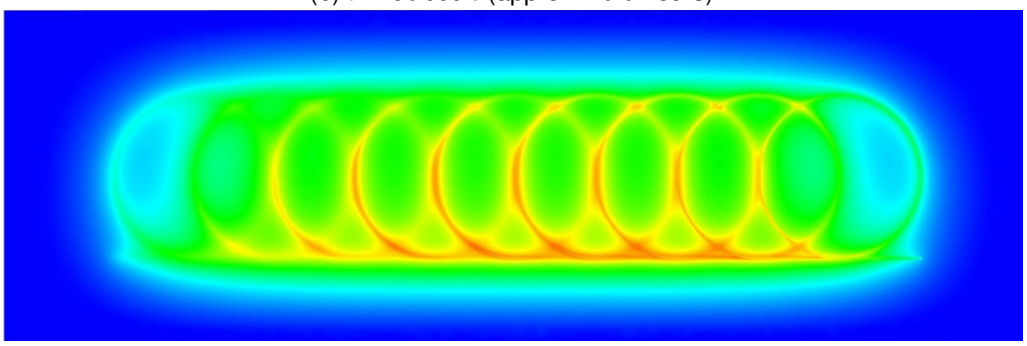

(c) $t = 200\,000$ s (approx. 2.3 days)

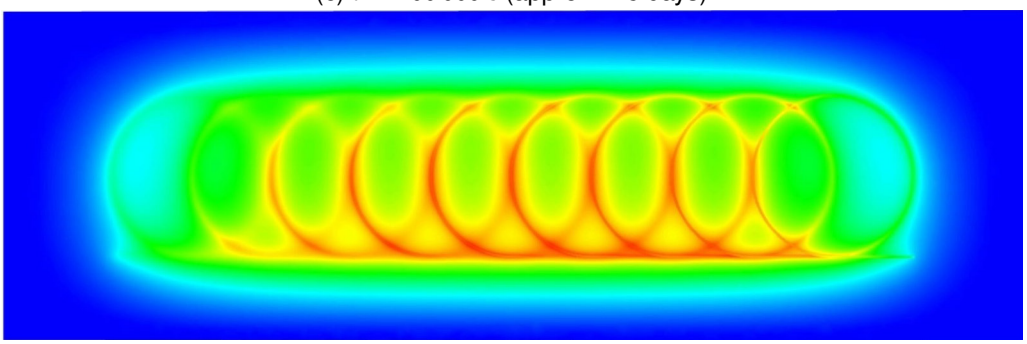

(d) $t = 800\,000$ s (approx. 9.3 days)

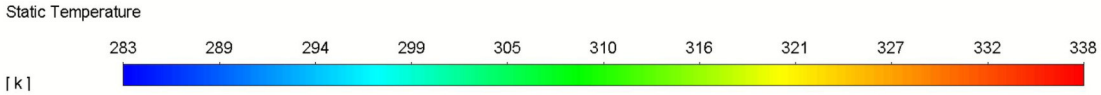

Figure 52: Temperature contour plots in the xy-plane from transient to steady-state.

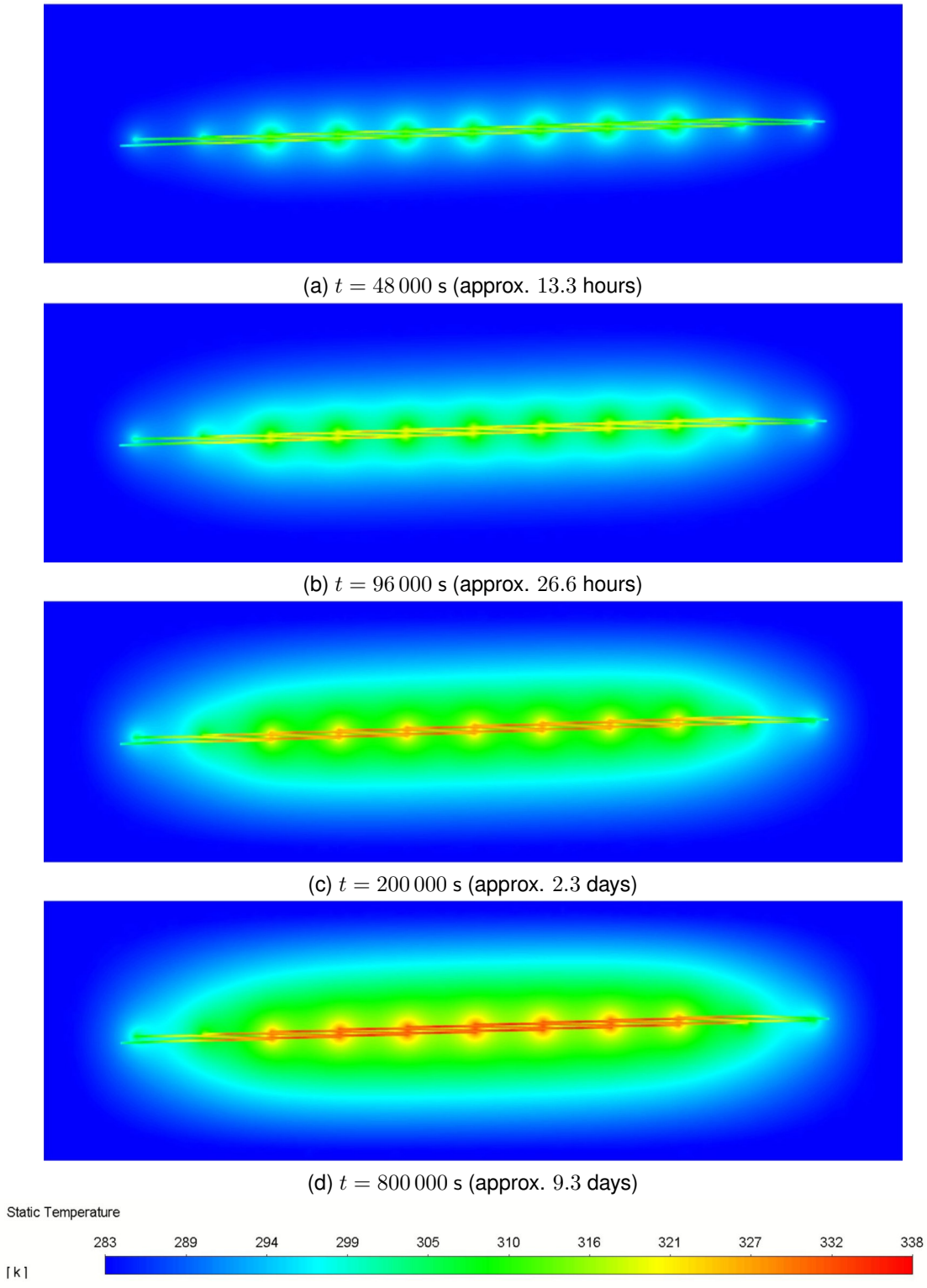

(a) $t = 48\,000$ s (approx. 13.3 hours)

(b) $t = 96\,000$ s (approx. 26.6 hours)

(c) $t = 200\,000$ s (approx. 2.3 days)

(d) $t = 800\,000$ s (approx. 9.3 days)

Figure 53: Temperature contour plots in the yz-plane from transient to steady-state.

As previously explained in chapter two, just like the earth basket model, the results of this horizontal slinky heat exchanger model will be recorded at every time step on a radially uniform surface. This exported data can then be used by the AIT's *GEOFIT* partners, responsible for far-field heat conduction modelling, as time dependent input parameters.

9.3 Comparison between Heat Exchanger Geometries

In the following section the three varying geometries presented in this thesis are compared. Contour-plots at steady-state conditions of all three models with a colour map scaled to the maximum temperature of the horizontal slinky heat exchanger model are displayed in Figure 54 below. The three models were all modelled with the material properties of dry sand, displayed previously in Table 1, as the heat conducting medium. After approximately 9.5 days ($t = 800\,000$ s) the horizontal slinky model in Figure 54c shows the highest temperature of 338 K, closely followed by the single earth basket model in Figure 54a with 333 K. The double earth basket model in Figure 54b has by far the lowest maximum temperature at steady-state conditions with 316 K. The varying maximum temperatures can be traced back to the respective heat exchanger's distance between the heating cable's loops. Even though the horizontal slinky model has a slightly larger heating cable surface area of 0.21596 m^2, compared to the earth basket model with a heating cable surface area of 0.20429 m^2, the horizontal slinky model displays the highest temperatures at steady-state. Yet, the minimum vertical distance between adjacent loops is 6 mm in the horizontal slinky model and 94 mm in the earth basket model. This creates small zones of higher temperatures between the horizontally spaced loops. The single and double earth basket models have already been compared in detail in the previous chapter.

While a uniform vertical temperature distribution is observed in the horizontal slinky model's yz-plane, the horizontal temperature distribution is asymmetric in the xy-plane (see Figure 54c below). This geometric asymmetry is the most prominent difference to the single earth basket model depicted in Figure 54a below. Even though the horizontal slinky heat exchanger displays a $5\ ^\circ C$ higher maximum temperature on its asymmetric side, where the adjacent loops are connected, the internal temperature field between the slinky loops is higher and significantly larger in the single earth basket model. Temperatures above 320 K are only limited to a small area on the inner side of the horizontal heat exchanger, where its loop connections are situated (see Figure 54c below). This high temperature field is significantly larger inside the single earth basket model, as it also extends radially inside the helix (see Figure 54a below). Naturally, the loops situated the furthest from the models' centres are affected the strongest by the boundary conditions and therefore display significantly lower temperatures than their adjacent counterparts in both models. If identical material properties and heat inputs are used, zones of high temperature build-ups, which are not situated directly on the heating cable's surface, indicate a lower efficiency of transporting heat from the model's heat source to its boundaries. Thus, for realistic heat exchanger applications the conclusion can be drawn, that the portrayed stagnant temperature build-up inside the single earth basket

at thermal equilibrium displayed in Figure 54a indicates a disadvantage regarding efficiency, compared to the horizontal slinky heat exchanger displayed in Figure 54c. The heat input applied on the heating cable's surface is not transported as efficiently away from the earth basket's centrally placed loops, as is the case with the horizontal exchanger's loops.

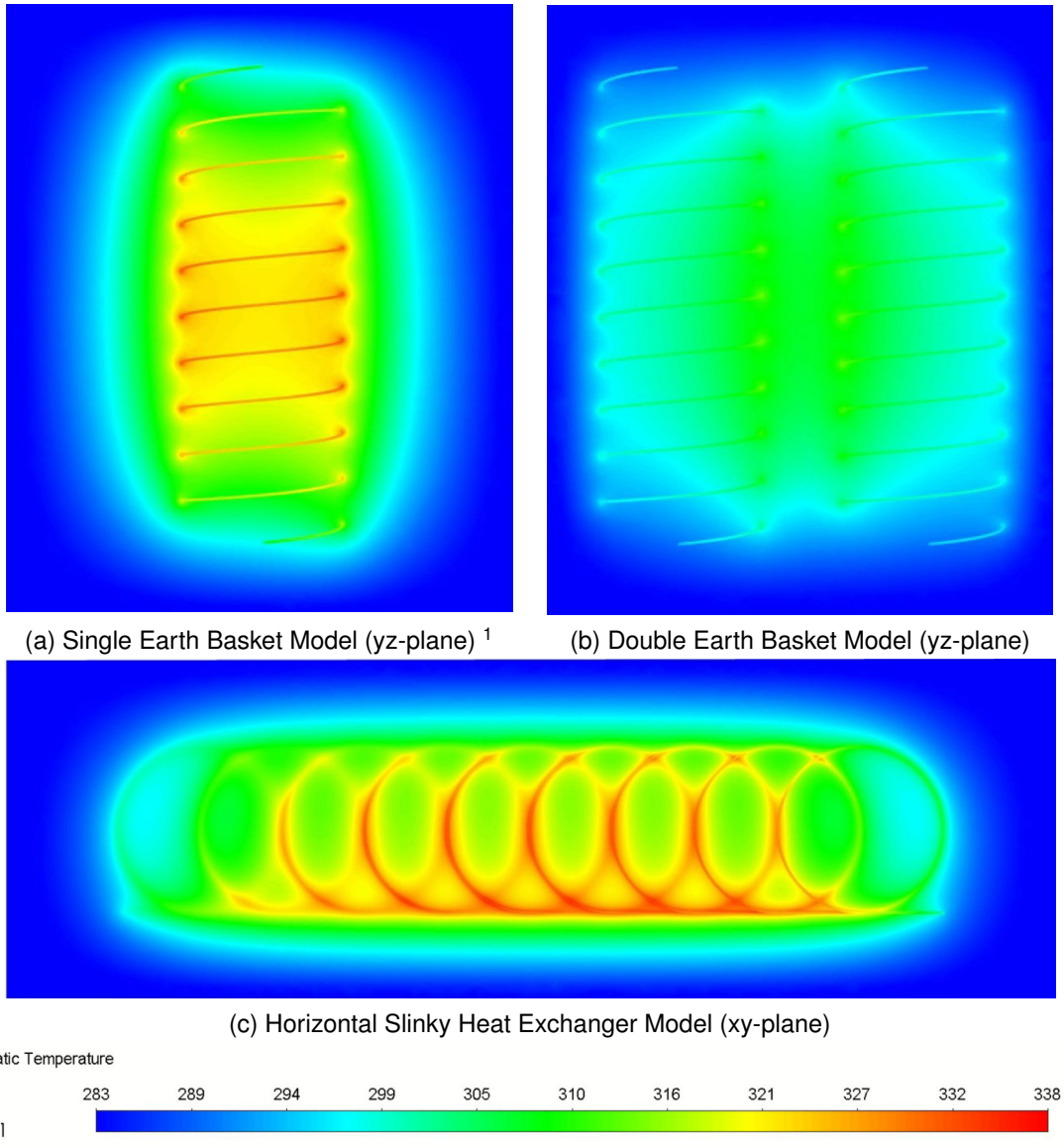

(a) Single Earth Basket Model (yz-plane) [1]

(b) Double Earth Basket Model (yz-plane)

(c) Horizontal Slinky Heat Exchanger Model (xy-plane)

Figure 54: Comparison between single, double earth basket and horizontal slinky at steady-state.

The only significant temperature build-up in the horizontal slinky model is visible at the adjacent loop's overlaps and where the connections are situated (see Figure 54c above). It should be noted, that varying types of horizontal slinky heat exchangers exist, which do not only vary in diameter and loop pitch configurations, but also in the way their flow and return pipes are placed. The modelled geometry presented in this chapter represents a more efficient configuration, whereby the individual slinky coils are placed in a loop around buildings,

[1] Steurer, A. (2020). GEOFIT research project - CFD modelling. Austrian Institute of Technology

which separates the flow and return piping. In geometrically symmetric applications, that are placed in horizontally spaced rows, the return flow is located on the opposite side of the loop connections and thus affects the heat exchangers efficiency. A sketch of such a configuration is displayed in Figure 2a in the second chapter. Implemented in a model, this would mitigate the horizontal heat exchangers asymmetric temperature profile in the xy-plane, displayed in Figure 54c above. However, the temperature build-up at the horizontal heat exchanger's centre would still be significantly lower than at the earth basket's centre displayed in Figure 54a above.

Additionally, the coils or loops placed at the outer positions and thus closest to the boundary conditions of all models experienced significantly lower temperatures than their centrally placed counterparts, whereby at every model's centre a stagnant high temperature area has formed at steady-state conditions. As previously described, this effect is the strongest in the earth basket heat exchanger configuration displayed in Figure 54a above. These observations make further planned loop pitch variations of the individual heat exchanger configurations highly interesting. In the earth basket's case, non-uniform loop pitch distributions may prove to be a viable concept to increase the heat exchanger's efficiency. The loop pitch is decreased towards both vertical ends and subsequently increased at the earth basket's centre. This results in a higher number of loops at the earth basket's vertical ends, where the heat transport efficiency could be increased with a larger surface area of the heat exchanger, i.e. loops. Subsequently, less loops will exist at the earth basket's centre, where the stagnant temperature distribution lowers the efficiency of the heat transport from the heat exchanger's surrounding to its surface. However, this investigation would reach beyond the scope of this thesis. Nonetheless, it proves to be an interesting topic waiting to be addressed in future *GEOFIT* research.

The *GEOFIT* research project aims to accurately analyse and quantify this difference in heat transfer efficiency caused by varying geometric parameters of shallow ground source heat exchangers. This goal will be achieved through the design of an engineering tool for accurate heat exchanger dimensioning. Together with the far-field models, conducted by the AIT's *GEOFIT* partners, the presented horizontal slinky heat exchanger model's exported data at every time-step provides the necessary research groundwork for this design tool.

10 Conclusion

Lastly, the previously presented and discussed models and their results will be briefly concluded in the following chapter.

The comparison between the analytically calculated solution and the numeric results of the geometrically simplified rod model has shown extremely accurate matches. The temperature difference relative to the maximum temperature reached at thermal equilibrium between the two solutions at steady-state conditions lay well below 0.025 percent for varying amplitudes and maximum positions of the time-independent heat source function. Naturally, the deviation between the two solutions is larger in the early transient period, but the relative temperature difference is still well below 0.3 percent. The accurate match of these results substantiates the use of the *ANSYS Fluent* numeric solver to perform CFD simulations with the developed models presented in this thesis. This is extremely important, as further far-field modelling and design tool development, as part of the *GEOFIT* work package three deliverable, is dependent on accurate solutions of the CFD heat exchanger models. Furthermore, it has proven to be a neat way to display the applied physical concepts of heat conduction by the numeric solver to the reader.

The pre-existing earth basket heat exchanger model is further substantiated by a corresponding experimental setup, whose comparison is presented in this thesis. However, the large-scale experiment is highly time-consuming and possesses a fairly low and static data resolution, depending on the physical placement of temperature sensors. Hence, the need for accurate CFD models, whose data can be exported at very high resolutions and adjustable locations, once a sufficient match between model and experiment has been proven. This comparison between the simulated temperature distribution and experimentally measured data has shown sufficiently good matches. Naturally, the difference between model and experiment in high temperature areas during the early transient period is the largest. This is due to the high temperature increase over a short period of time, which leads to larger absolute temperature differences. Nonetheless, if the initial temperature off-sets at the *PT1000* sensors due to an existing non-uniform initial temperature distribution within the experiment are taken into account, the earth basket model and corresponding experiment show sufficiently accurate matches throughout the entire experimental run.

Solving the heat conduction equation with a time-independent source term in chapter five has provided the theoretical basis needed to analyse the double earth basket model's behaviour during the material parameter variation, which has been conducted as part of the framework of this thesis as well. As mentioned in the introduction, the AIT took accurate material property measurements of the thermal conductivity, specific heat capacity and bulk density from in-situ probes of varying substrates. As previously indicated by the heat conduction equation during the calculation of the analytical solution, the thermal conductivity is the sole material

parameter influencing the maximum temperature reached at the thermal-equilibrium. Therefore, substrates with a low thermal conductivity like conventional dry garden humus displayed the highest temperatures. The thermal diffusivity, a combination of all three previously mentioned material parameters, influences the time it takes for the solution to reach the thermal equilibrium. Inversely, the garden humus soil's low thermal conductivity coincides with its low bulk density and thus the resulting low thermal diffusivity caused the model with humus soil as a heat conducting medium to take the longest time to reach steady-state conditions.

As previously explained in the introduction, due to the large dimensions of the earth basket experiment, varying the heat conductive medium is a time-consuming process. Therefore, a small-scale experiment named the "Thermo-Pipe" was developed by the AIT to test the heat conductive behaviour of substrates before they are implemented in the large-scale earth basket experiment. The corresponding CFD Model was developed as part of the framework of this thesis. While the pipe's scale and elongated geometrical shape causes a deviation between experiment and simulation at the furthest placed senors positions from the heat source, the temperature profile during the transient period is satisfyingly accurate. The results of the "Thermo-Pipe" have to be interpreted while keeping the nature and purpose of the experiment and corresponding model in mind. The experiment and model may serve as a pre-selection tool for different materials with varying moisture contents to be chosen as heat conducting substrates in the large-scale heat exchanger experiments.

The heat exchanger CFD models developed as part of the framework of this thesis, were designed with the same external parameters as the earth basket experiment and corresponding model. Factors like the initial and boundary condition, control volume and total heat input were kept constant for two reasons. Firstly, to make further corresponding experimental runs with the existing facilities at the AIT possible and secondly, to create a viable comparison between the different heat exchanger models. The latter is important, as the previously mentioned match between earth basket model and experiment therefore also substantiates the results of the other models with a high degree of certainty. Therefore, the results of the horizontal slinky heat exchanger model will be exported at every time-step and may serve as high resolution input data for further far-field modelling and a basis for the development of an engineering tool conducted by the AIT's *GEOFIT* partners. The horizontal slinky heat exchanger's results have also shown expected differences to the earth basket model, whereby the most visible difference lies in the geometric asymmetry of the chosen horizontal slinky variant. Naturally, the coils or loops placed at the outer positions and thus closest to the boundary conditions of all models experienced significantly lower temperatures than their centrally placed counterparts. Whereby at the model's centre a stagnant high temperature area has formed at steady-state conditions. This effect is the strongest in the earth basket heat exchanger configuration.

These observations make further planned loop pitch variations of the individual heat exchanger configurations highly interesting. In the earth basket's case, non-uniform loop pitch distributions may prove to be a viable concept to increase the heat exchanger's efficiency. The loop pitch would be decreased towards both vertical ends and subsequently increased at the earth basket's centre. This results in a higher number of loops at the earth basket's vertical ends and less loops at the earth basket's centre, which may drastically influence the heat exchanger's efficiency. This can be addressed in further *GEOFIT* research in the near future with the validated methodology and the parameterised models developed within this thesis.

References

AIT Austrian Institute of Technology. (2020). GEOFIT research project.

Al-Khoury, R. (2011). *Computational modeling of shallow geothermal systems*. CRC Press.

Connor, N. (2019). *What is fourier's law of thermal conduction - definition* [Thermal engineering] [Section: Heat Transfer / Thermal Conduction]. Retrieved August 5, 2020, from https://www.thermal-engineering.org/what-is-fouriers-law-of-thermal-conduction-definition/

Conti, P. (2018). An analytical method to simulate the dynamic performances of truncated cone helix ground heat exchangers. *Energy Procedia*, *148*, 1214–1221. https://doi.org/10.1016/j.egypro.2018.08.009

Eswiasi, A., & Mukhopadhyaya, P. (2020). Critical review on efficiency of ground heat exchangers in heat pump systems [Number: 2 Publisher: Multidisciplinary Digital Publishing Institute]. *Clean Technologies*, *2*(2), 204–224. https://doi.org/10.3390/cleantechnol2020014

Florides, G., & Kalogirou, S. (2007). Ground heat exchangers - a review of systems, models and applications. *Renewable Energy*, *32*(15), 2461–2478. https://doi.org/10.1016/j.renene.2006.12.014

Ganster, M. (2015). *Partielle differentialgleichungen* [Mathematik 2 Bauingenieure SS 2015]. Graz University of Technology. Mathematik 2 Bauingenieure SS 2015. Retrieved June 10, 2020, from https://www.math.tugraz.at/~ganster/lv_mathematik_2_bau_ss_2015/08_partielle_dgln.pdf

GEOFIT – compact geothermal heat exchangers. (2020). Retrieved February 26, 2020, from https://geofit-project.eu/technologies/non-standard-and-cost-effective-compact-heat-exchangers/

GEOFIT – project objectives. (2020). Retrieved February 26, 2020, from https://geofit-project.eu/project/objectives/

Hancock, M. (2006). *The 1-d heat equation*. Massachusetts Institute of Technology. Massachusetts Institute of Technology: MIT OpenCourseWare. Retrieved June 10, 2020, from https://ocw.mit.edu/courses/mathematics/18-303-linear-partial-differential-equations-fall-2006/#

Javadi, H., Mousavi Ajarostaghi, S. S., Rosen, M. A., & Pourfallah, M. (2019). Performance of ground heat exchangers: A comprehensive review of recent advances. *Energy*, *178*, 207–233. https://doi.org/10.1016/j.energy.2019.04.094

Kaimann GmbH. (2020). Kaiflex ST Datenblatt. Retrieved June 17, 2020, from https://www.kaimann.com/authoring/auth/Documents/Kaiflex_ST-AUTDE.pdf

Männer, J. (2012). *Untersuchung des thermischen Verhaltens von Böden*. Technische Universität Dresden, Institut für Geotechnik. Retrieved November 3, 2020, from https://tu-dresden.de/bu/bauingenieurwesen/geotechnik/ressourcen/dateien/studium/abschlussarbeiten/abgeschlossene-arbeiten/projektarbeiten/2012/Kurzfassung_JM.pdf?lang=de

Manzella, A. (2015). Geothermal energy [Publisher: EDP Sciences]. *EPJ Web of Conferences*, *98*(4004), 22. https://doi.org/10.1051/epjconf/20159804004

Rau, H., Moran, P., Manton, R., & Goggins, J. (2019). Changing energy cultures? household energy use before and after a building energy efficiency retrofit. *Sustainable Cities and Society*, *54*, 13. https://doi.org/10.1016/j.scs.2019.101983

Showalter, R. E. (2013). *The diffusion equation* [Mathematical Methods for Engineers & Scientists, WS 2013, MTH 482/582]. Oregon State University, Corvallis. Mathematical Methods for Engineers & Scientists, WS 2013, MTH 482/582. Retrieved August 6, 2020, from http://sites.science.oregonstate.edu/~show/docs/482-Notes1.pdf

Steurer, A. (2020). GEOFIT research project - CFD modelling. Austrian Institute of Technology.

Wetzel, T., & von Böckh, P. (2012). *Heat transfer: Basics and practice*. Berlin, Heidelberg, Springer. https://doi.org/10.1007/978-3-642-19183-1

Widder, D. V. (1976). *The heat equation* (Vol. 76). Academic Press.

Xiong, Z., Fisher, D. E., & Spitler, J. D. (2015). Development and validation of a slinky™ ground heat exchanger model. *Applied Energy*, *141*, 57–69. https://doi.org/10.1016/j.apenergy.2014.11.058

Appendices

Appendix A

Steady-State Solution Integration Steps

In the following section the calculation steps for the steady-state solution of Eq. (17) from chapter 5 displayed below are shown.

$$T^*(x) = -\frac{A}{\lambda}\iint_x e^{-\sigma(s-\xi)^2} ds dx$$

The first integral is displayed and calculated below. The additional positional integration variable s is the substituted by the standard positional variable x.

$$T^*(s) = -\frac{A}{\lambda}\int_x e^{-\sigma(s-\xi)^2} ds \tag{17.1}$$

Substitute $u = \sqrt{\sigma}(s-\xi) \quad \Rightarrow \quad \frac{\mathrm{du}}{\mathrm{ds}} = \sqrt{\sigma} \quad \Rightarrow \quad ds = \frac{1}{\sqrt{\sigma}}\, du$:

$$= -\frac{A}{2\lambda}\sqrt{\frac{\pi}{\sigma}}\int \frac{2e^{-u^2}}{\sqrt{\pi}}\, du \tag{17.2}$$

Now, the constant is carried over to the solution and the integral is solved. This specific integral is special though, as its solution is the Gaussian error function:

$$\int \frac{2e^{-u^2}}{\sqrt{\pi}} du = \mathrm{erf}\,(u) \tag{17.3}$$

The full solution, including constants is thus:

$$T^*(s) = -\frac{A}{2\lambda}\sqrt{\frac{\pi}{\sigma}}\int_x \frac{2e^{-u^2}}{\sqrt{\pi}} du = -\frac{A}{2\lambda}\sqrt{\frac{\pi}{\sigma}}\,\mathrm{erf}\,(u) \tag{17.4}$$

Through re-substitution of $u = \sqrt{\sigma}(s-\xi)$, while the standard positional variable $s = x$ is used again, the following solution of the first integral is reached, which is presented as Eq. (18) in chapter 5:

$$T^*(x) = -\frac{A}{2\lambda}\sqrt{\frac{\pi}{\sigma}}\int \mathrm{erf}\left(\sqrt{\sigma}(x-\xi)\right) + C_1\, dx$$

Applying the constant and sum rule, $C_1\, dx = C_1 x$ and other constants will be added later. The integral to be solved is therefore the following:

$$\int \mathrm{erf}\left(\sqrt{\sigma}(x-\xi)\right) dx \tag{18.1}$$

The following expression is substituted again $u = \sigma(x - \xi) \quad \Rightarrow \quad \frac{\mathrm{d}u}{\mathrm{d}x} = \sqrt{\sigma} \quad \Rightarrow \quad dx = \frac{1}{\sqrt{\sigma}}\, du$ and leads to the following integral:

$$= \frac{1}{\sqrt{\sigma}} \int \operatorname{erf}(u)\, du \tag{18.2}$$

The integral $\int \operatorname{erf}(u)\, du$ in Eq. (18.2) above is a standard integral and will be solved with the aid of partial integration: $\int f'g = fg - \int fg'$. Whereby $f' = 1 \quad \Rightarrow \quad f = u$ and $g = \operatorname{erf}(u) \quad \Rightarrow \quad g' = \frac{2e^{-u^2}}{\sqrt{\pi}}$ leads to the following expression:

$$\int \operatorname{erf}(u)\, du = u \operatorname{erf}(u) - \int \frac{2ue^{-u^2}}{\sqrt{\pi}}\, du \tag{18.3}$$

The integral from Eq. (18.3) above is now solved through further substitution: $v = -u^2 \quad \Rightarrow \frac{\mathrm{d}v}{\mathrm{d}x} = -2u \quad \Rightarrow \quad du = -\frac{1}{2u}\, dv$ which leads to the following solvable integral:

$$= -\frac{1}{\sqrt{\pi}} \int e^v\, dv \tag{18.4}$$

As $\int e^v\, dv = e^v$, $v = -u^2$ is re-substituted into the solution of Eq. (18.4) above and thus leads to the following solution for Eq. (18.2) above:

$$\frac{1}{\sqrt{\sigma}} \int \operatorname{erf}(u)\, du = \frac{1}{\sqrt{\sigma}} \left(u \operatorname{erf}(u) + \frac{e^{-u^2}}{\sqrt{\pi}} \right) \tag{18.5}$$

Re-substituting $u = \sqrt{\sigma}(x - \xi)$ into Eq. (18.5) above leads to the following solution for the calculated integral from Eq. (18.1) above:

$$= (x - \xi) \operatorname{erf}\left(\sqrt{\sigma}(x - \xi)\right) + \frac{e^{-\sigma(x-\xi)^2}}{\sqrt{\pi\sigma}} \tag{18.6}$$

Now, the integration constants and $-\frac{A}{2\lambda}\sqrt{\frac{\pi}{\sigma}}$ from Eq. (18) may be added to Eq. (18.6) displayed above again. This expression is then further simplified, while keeping in mind that $\frac{\sigma}{\sqrt{\sigma}} = \sqrt{\sigma}$, which eventually leads to the following steady-state solution displayed as Eq. (19) in chapter 5:

$$T^*(x) = -\frac{A}{2\lambda\sigma} \left[\sqrt{\pi\sigma}\, (x - \xi) \operatorname{erf}\left(\sqrt{\sigma}(x - \xi)\right) + e^{-\sigma(x-\xi)^2} \right] + C_1 x + C_2$$

The integration constants C_1 and C_2 will be calculated in chapter 5 again and their solutions are presented as Eq. (22) and Eq. (21) respectively.

Appendix B

Transient Solution: Integral I_2 Integration Steps

In the following section the calculation steps of the second integral I_2 of the transient solution from Eq. (65) in chapter 5 are shown.

$$I_2 = -C_3 \int_0^L \sin\left(\frac{n\pi}{L}x\right)\frac{x}{L}dx$$

Due to the linearity rules of integration, the constant multiplication term $-\frac{C_3}{L}$ can be excluded and multiplied with the integral's solution at a later stage. Thus, the simplified integral to be calculated is the following:

$$= \int_0^L x \sin\left(\frac{\pi n x}{L}\right) dx \tag{65.1}$$

Firstly, this integral is solved without the integration boundaries $[0, L]$ by substituting $u = \frac{x}{L} \quad \Rightarrow \quad \frac{\mathrm{d}u}{\mathrm{d}x} = \frac{1}{L} \quad \Rightarrow \quad dx = L\,du$. This leads to the following integral dependent on the substituted variable u:

$$= L^2 \int u \sin(\pi n u)\, du \tag{65.2}$$

Applying the linearity rules of integration again and carrying over the constant L_2 to the integral's solution, the integral $\int u \sin(\pi n u)\, du$ will be solved through partial integration, whereby $\int f'g = fg - \int fg'$. This leads to: $f' = \sin(\pi n u) \quad \Rightarrow \quad f = -\frac{\cos(\pi n u)}{\pi n}$ and subsequently $g = u \quad \Rightarrow \quad g' = 1$. Applying the previous rules of partial integration yields the following expression:

$$= -\frac{u\cos(\pi n u)}{\pi n} - \int -\frac{\cos(\pi n u)}{\pi n}\, du \tag{65.3}$$

The integral $\int -\frac{\cos(\pi n u)}{\pi n}\, du$ from Eq. (65.3) above may be solved through further substitution, whereby $v = \pi n u \quad \Rightarrow \quad \frac{\mathrm{d}v}{\mathrm{d}u} = \pi n \quad \Rightarrow \quad du = \frac{1}{\pi n}\, dv$. This resulting integral displayed below can now be solved with ease.

$$= -\frac{1}{\pi^2 n^2} \int \cos(v)\, dv \tag{65.4}$$

The solvable integral has the following solution:

$$\int \cos(v)\, dv = \sin(v) \tag{65.5}$$

The solved integral may now be multiplied with the previously excluded constant $-\frac{1}{\pi^2 n^2}$, while the re-substitution of $v = \pi n u$ leads to the following expression:

$$= -\frac{\sin(\pi n u)}{\pi^2 n^2} \tag{65.6}$$

Inserting the solved integral into Eq. (65.3) from above and multiplying the solution with the previously excluded constant L^2 yields the following equation:

$$L^2 \int u \sin(\pi n u)\, du = \frac{L^2 \sin(\pi n u)}{\pi^2 n^2} - \frac{L^2 u \cos(\pi n u)}{\pi n} \tag{65.7}$$

Now, the substitution variable $u = \frac{x}{L}$ is re-substituted and multiplied with the previously excluded constant $-\frac{C_3}{L}$ from the original Eq. (65).

$$-\frac{C_3}{L} \int x \sin\left(\frac{\pi n x}{L}\right) dx = \frac{C_3 x \cos\left(\frac{\pi n x}{L}\right)}{\pi n} - \frac{C_3 L \sin\left(\frac{\pi n x}{L}\right)}{\pi^2 n^2} \tag{65.8}$$

Further simplification leads to the following solution without integration boundaries:

$$= -\frac{C_3 L \sin\left(\frac{\pi n x}{L}\right) - C_3 \pi n x \cos\left(\frac{\pi n x}{L}\right)}{\pi^2 n^2} \tag{65.9}$$

Inserting and subtracting the integration boundaries $[0, L]$, the following solution for Eq. (65) depicted in chapter 5 is reached:

$$= -\frac{C_3 L \left(\sin(\pi n) - \pi n \cos(\pi n)\right)}{\pi^2 n^2}$$

The solutions for the remaining integrals I_m, which are needed to solve the b_n factor and subsequently reach the transient solution of the rod model's analytical solution, are continued in chapter 5 again.

Transient Solution: Integral I_5

In the following section the solution of the fifth integral I_5 of the transient solution from Eq. (68) in chapter 5 is shown. Due to the complexity of the integral displayed below, the solution was calculated with the CAS software *Wolfram Mathematica 12.1* and presented in the appendix.

$$I_5 = \sqrt{\pi\sigma} \int_0^L x \sin\left(\frac{n\pi}{L}x\right) \operatorname{erf}\left(\sqrt{\sigma}(x-\xi)\right) dx$$

```
Integrate[Sqrt[Pi * σ] * Sin[n * Pi * (x / L)] * Erf[Sqrt[σ] * (x - ξ)] * x, {x, 0, L}]
```

Out[30]=

$$\sqrt{\pi}\,\sqrt{\sigma}\left(\frac{1}{4\,n\,\pi^{3/2}\,\sigma}e^{-\frac{i\,n\pi\,\xi}{L}}\,L\left(-2\,e^{-(L-\xi)\left(\frac{i\,n\,\pi}{L}+(L-\xi)\,\sigma\right)}\sqrt{\sigma}+2\,e^{-\frac{n^2\pi^2}{4L^2\sigma}}\sqrt{\pi}\,\xi\,\sigma\,\text{Erf}\left[\frac{i\,n\,\pi+2\,L\,(L-\xi)\,\sigma}{2\,L\,\sqrt{\sigma}}\right]+\frac{e^{-\frac{n^2\pi^2}{4L^2\sigma}}\,n\,\pi^{3/2}\,\text{Erfi}\left[\frac{n\pi-2\,i\,L\,(L-\xi)\,\sigma}{2\,L\,\sqrt{\sigma}}\right]}{L}\right)+\right.$$

$$\frac{e^{\frac{i\,n\pi\,\xi}{L}-\frac{n^2\pi^2}{4L^2\sigma}-(L-\xi)^2\sigma}\left(-2\,e^{\frac{n\pi\left(n\pi+4\,i\,L\,(L-\xi)\,\sigma\right)}{4L^2\sigma}}\,L\,\sqrt{\sigma}+e^{(L-\xi)^2\sigma}\sqrt{\pi}\,\left(n\,\pi-2\,i\,L\,\xi\,\sigma\right)\text{Erfi}\left[\frac{n\,\pi+2\,i\,L\,(L-\xi)\,\sigma}{2\,L\,\sqrt{\sigma}}\right]\right)}{4\,n\,\pi^{3/2}\,\sigma}-$$

$$\frac{e^{\frac{i\,n\pi\,\xi}{L}-\frac{n^2\pi^2}{4L^2\sigma}-\xi^2\sigma}\left(-2\,e^{\frac{n\pi\left(n\pi-4\,i\,L\,\xi\,\sigma\right)}{4L^2\sigma}}\,L\,\sqrt{\sigma}+e^{\xi^2\sigma}\sqrt{\pi}\,\left(n\,\pi-2\,i\,L\,\xi\,\sigma\right)\text{Erfi}\left[\frac{n\,\pi-2\,i\,L\,\xi\,\sigma}{2\,L\,\sqrt{\sigma}}\right]\right)}{4\,n\,\pi^{3/2}\,\sigma}-$$

$$\frac{e^{-\xi^2\sigma}\,L^2\left(e^{-\frac{n^2\pi^2-4\,i\,L\,n\pi\,\xi\,\sigma-4\,L^2\,\xi^2\,\sigma^2}{4L^2\sigma}}\,\text{Erfi}\left[\frac{n\,\pi-2\,i\,L\,\xi\,\sigma}{2\,L\,\sqrt{\sigma}}\right]+e^{-\frac{n^2\pi^2+4\,i\,L\,n\pi\,\xi\,\sigma-4\,L^2\,\xi^2\,\sigma^2}{4L^2\sigma}}\,\text{Erfi}\left[\frac{n\,\pi+2\,i\,L\,\xi\,\sigma}{2\,L\,\sqrt{\sigma}}\right]\right)}{2\,n^2\,\pi^2}-$$

$$\frac{e^{-\frac{i\,n\pi\,\xi}{L}}\,L\left(-2\,e^{\xi\left(\frac{i\,n\,\pi}{L}-\xi\,\sigma\right)}\sqrt{\sigma}+2\,e^{-\frac{n^2\pi^2}{4L^2\sigma}}\sqrt{\pi}\,\xi\,\sigma\,\text{Erf}\left[\frac{i\,n\,\pi-2\,L\,\xi\,\sigma}{2\,L\,\sqrt{\sigma}}\right]+\frac{e^{-\frac{n^2\pi^2}{4L^2\sigma}}\,n\,\pi^{3/2}\,\text{Erfi}\left[\frac{n\,\pi+2\,i\,L\,\xi\,\sigma}{2\,L\,\sqrt{\sigma}}\right]}{L}\right)}{4\,n\,\pi^{3/2}\,\sigma}+$$

$$\frac{e^{-\xi^2\sigma}\,L^2\left(e^{-\frac{n^2\pi^2-4\,i\,L\,n\pi\,\xi\,\sigma-4\,L^2\,\xi^2\,\sigma^2}{4L^2\sigma}}\,\text{Erfi}\left[\frac{n\,\pi+2\,i\,L^2\,\sigma-2\,i\,L\,\xi\,\sigma}{2\,L\,\sqrt{\sigma}}\right]+e^{-\frac{n^2\pi^2+4\,i\,L\,n\pi\,\xi\,\sigma-4\,L^2\,\xi^2\,\sigma^2}{4L^2\sigma}}\,\text{Erfi}\left[\frac{n\,\pi-2\,i\,L^2\,\sigma+2\,i\,L\,\xi\,\sigma}{2\,L\,\sqrt{\sigma}}\right]\right)}{2\,n^2\,\pi^2}-$$

$$\left.\frac{L\,\text{Erf}\left[(L-\xi)\,\sqrt{\sigma}\right]\left(L\,n\,\pi\,\text{Cos}\left[n\,\pi\right]-L\,\text{Sin}\left[n\,\pi\right]\right)}{n^2\,\pi^2}\right)$$

CAS software solution of the 5th integral (I_5) from b_n calculations in Eq. (68).

Appendix C

Material Property Measurements Conducted by the AIT's Laboratory

Dry Sand

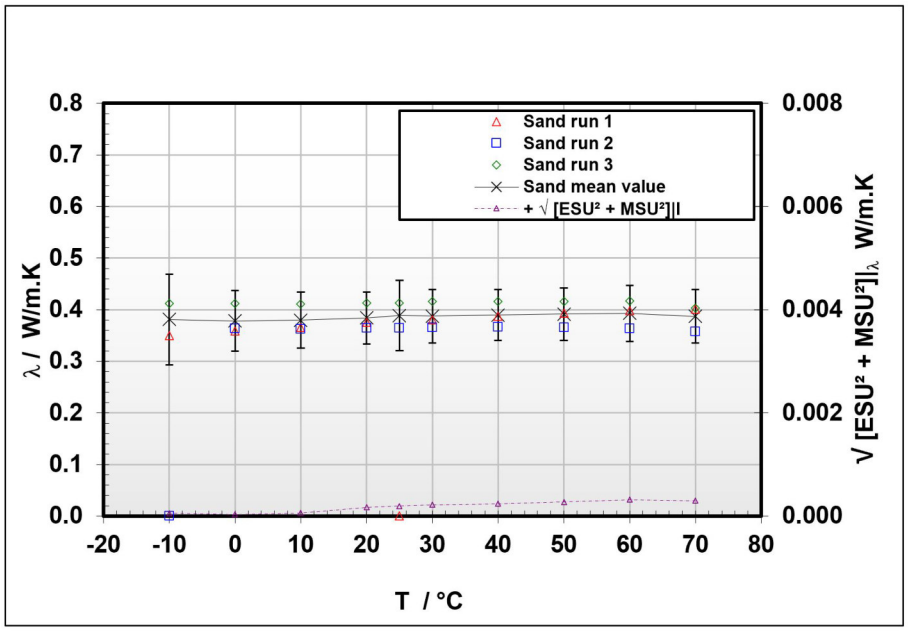

Measurements and statistical analysis of thermal conductivity of dry sand probes. [1]

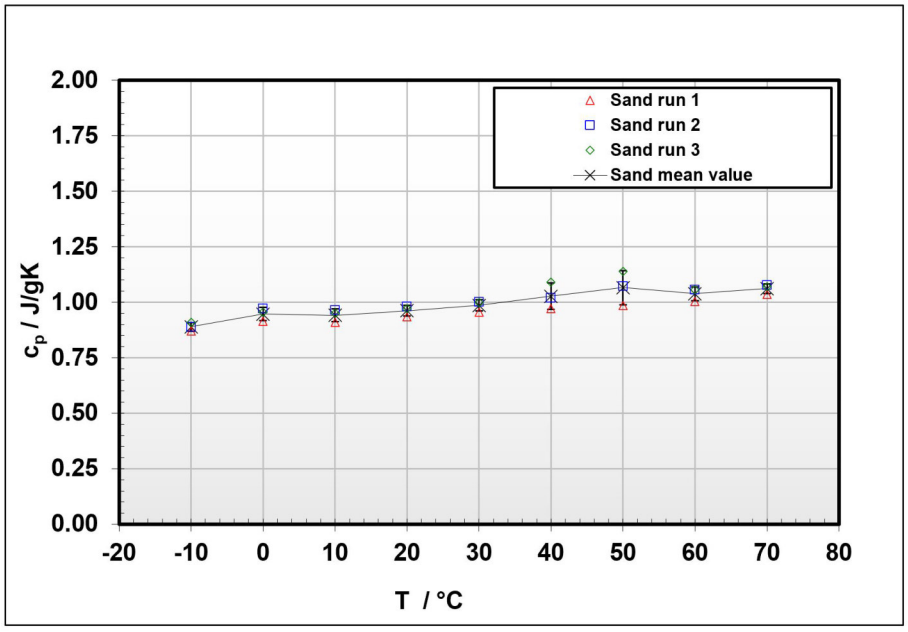

Measurements and statistical analysis of specific heat capacity of dry sand probes. [1]

[1] AIT Austrian Institute of Technology. (2020). GEOFIT research project

Sand	**Measurement procedure acoording to DIN EN 12664, DIN EN 12667, DIN EN 12939, ISO 8301, ASTM C518 and JIS A1412**				**Start of measurement:**		**18.11.2019**
					Gas flow:		**Ambient / Static**
					Isothermal conditions ∂T/∂t:		**< 0,1 K/min**
	measured data λ / W/m.K			**mean value λ / W/m.K**	**statistical analysis: k = 2 λ / W/m.K**		
T / °C	run 1	run 2	run 3	**mean value**	$+\sqrt{[ESU^2 + MSU^2]}\lambda$	$SDV\vert_\lambda$	$u_c(\lambda)$
70	0.4015	0.3575	0.4028	0.3873	0.00030	0.02575	0.05150
60	0.3984	0.3636	0.4168	0.3929	0.00032	0.02703	0.05407
50	0.3929	0.3653	0.4162	0.3915	0.00027	0.02545	0.05090
40	0.3871	0.3662	0.4155	0.3896	0.00024	0.02475	0.04950
30	0.3807	0.3654	0.4162	0.3874	0.00022	0.02608	0.05217
25	x-x-x	0.3643	0.4125	0.3884	0.00019	0.03406	0.06812
20	0.3751	0.3645	0.4125	0.3840	0.00017	0.02525	0.05050
10	0.3657	0.3622	0.4108	0.3796	0.00006	0.02712	0.05425
0	0.3591	0.3639	0.4122	0.3784	0.00003	0.02939	0.05879
-10	0.3499	x-x-x	0.4120	0.3809	0.00006	0.04393	0.08785

Sand	**Measurement procedure acoording to DIN EN 12664, DIN EN 12667, DIN EN 12939, ISO 8301, ASTM C518 and JIS A1412**				**Start of measurement:**		**18.11.2019**
					Gas flow:		**Ambient / Static**
					Isothermal conditions ∂T/∂t:		**< 0,1 K/min**
	measured data c_p / J/gK			**mean value c_p / J/gK**	**statistical analysis: k = 2 c_p / J/gK**		
T / °C	run 1	run 2	run 3	**mean value**	+ √ [ESU² + MSU²]|cp	SDV|$_{cp}$	**$u_c(c_p)$**
-10	0.870	0.888	0.908	0.889	x-x-x	0.01910	0.01910
0	0.915	0.971	0.955	0.947	x-x-x	0.02904	0.02904
10	0.910	0.964	0.950	0.941	x-x-x	0.02834	0.02834
20	0.935	0.980	0.971	0.962	x-x-x	0.02412	0.02412
30	0.956	1.002	0.998	0.985	x-x-x	0.02530	0.02530
40	0.971	1.020	1.090	1.027	x-x-x	0.06015	0.06015
50	0.986	1.073	1.138	1.065	x-x-x	0.07634	0.07634
60	1.003	1.056	1.055	1.038	x-x-x	0.03044	0.03044
70	1.036	1.077	1.071	1.061	x-x-x	0.02213	0.02213

Same Sand with 6.18 % Moisture Content

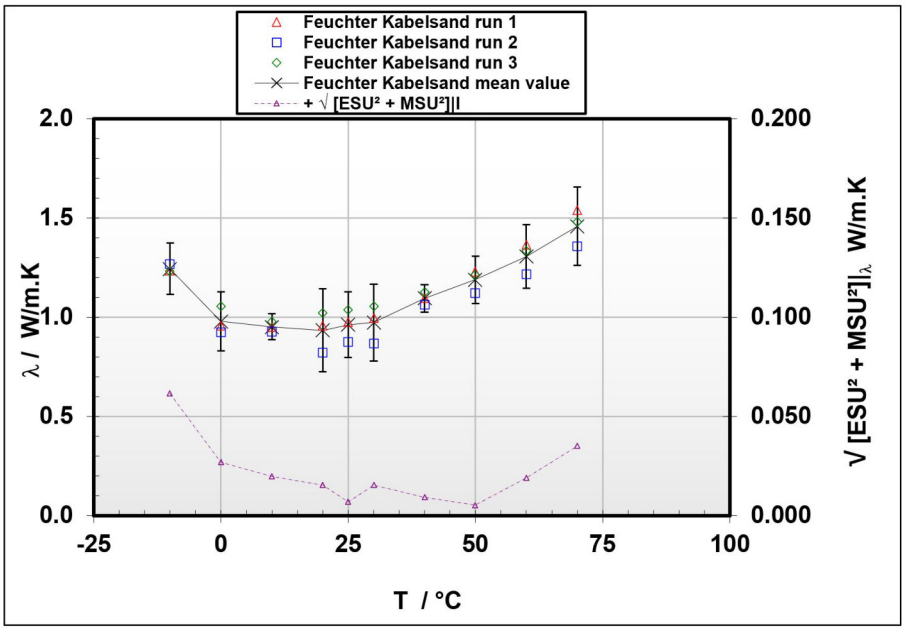

Measurements and statistical analysis of thermal conductivity of moist sand probes. [2]

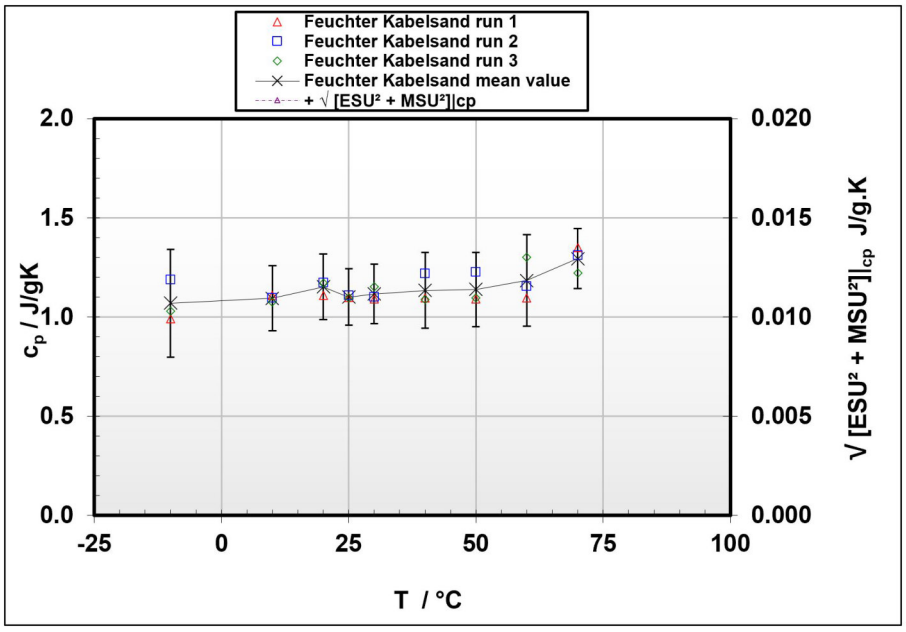

Measurements and statistical analysis of specific heat capacity of moist sand probes. [2]

[2]AIT Austrian Institute of Technology. (2020). GEOFIT research project

Feuchter Kabelsand	**Measurement procedure acoording to DIN EN 12664, DIN EN 12667, DIN EN 12939, ISO 8301, ASTM C518 and JIS A1412**				**Start of measurement:**		**01.07.2020**
					Gas flow:		**Ambient / Static**
					Isothermal conditions ∂T/∂t:		**< 0,1 K/min**
	measured data λ / W/m.K			**mean value λ / W/m.K**	**statistical analysis: k = 2 λ / W/m.K**		
T / °C	run 1	run 2	run 3	**mean value**	+ √ [ESU² + MSU²]|λ	SDV|λ	$u_c(\lambda)$
-10	1.2342	1.2657	1.2306	1.2435	0.06153	0.01933	0.12899
0	0.9567	0.9237	1.0558	0.9788	0.02695	0.06873	0.14765
10	0.9506	0.9258	0.9779	0.9514	0.01978	0.02604	0.06541
20	0.9575	0.8211	1.0230	0.9339	0.01543	0.10299	0.20827
25	0.9753	0.8739	1.0365	0.9619	0.00695	0.08210	0.16479
30	0.9960	0.8680	1.0545	0.9728	0.01539	0.09539	0.19324
40	1.0955	1.0610	1.1279	1.09	0.0092	0.0334	0.0694
50	1.2292	1.1200	1.2147	1.19	0.0053	0.0593	0.1191
60	1.3641	1.2165	1.3345	1.31	0.0189	0.0781	0.1607
70	1.5384	1.3574	1.4791	1.46	0.0351	0.0923	0.1974

Feuchter Kabelsand					**Start of measurement:**		**01.07.2020**
					Gas flow:		**Ambient / Static**
					Isothermal conditions ∂T/∂t:		**< 0,1 K/min**
	measured data c_p / J/gK			**mean value c_p / J/gK**	**statistical analysis: k = 2 c_p / J/gK**		
T / °C	run 1	run 2	run 3	**mean value**	+ √ [ESU² + MSU²]|cp	SDV|$_{cp}$	**$u_c(c_p)$**
-10	0.990	1.188	1.030	1.070	0.08694	0.10480	0.27233
10	1.109	1.097	1.077	1.095	0.08044	0.01633	0.16415
20	1.109	1.174	1.171	1.152	0.07406	0.03672	0.16532
25	1.098	1.108	1.095	1.100	0.07081	0.00684	0.14229
30	1.092	1.102	1.153	1.116	0.06748	0.03269	0.14996
40	1.096	1.219	1.088	1.134	0.06047	0.07342	0.19024
50	1.092	1.227	1.097	1.139	0.05287	0.07686	0.18657
60	1.095	1.154	1.302	1.184	0.04461	0.10632	0.23060
70	1.350	1.313	1.221	1.295	0.03565	0.06625	0.15047

Dry Humus Soil

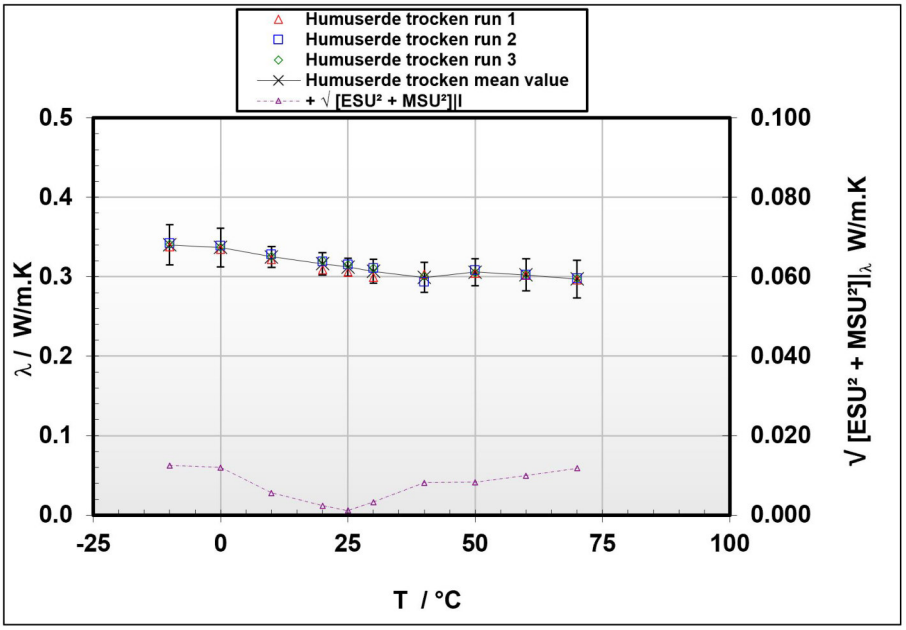

Measurements and statistical analysis of thermal conductivity of dry humus probes. [3]

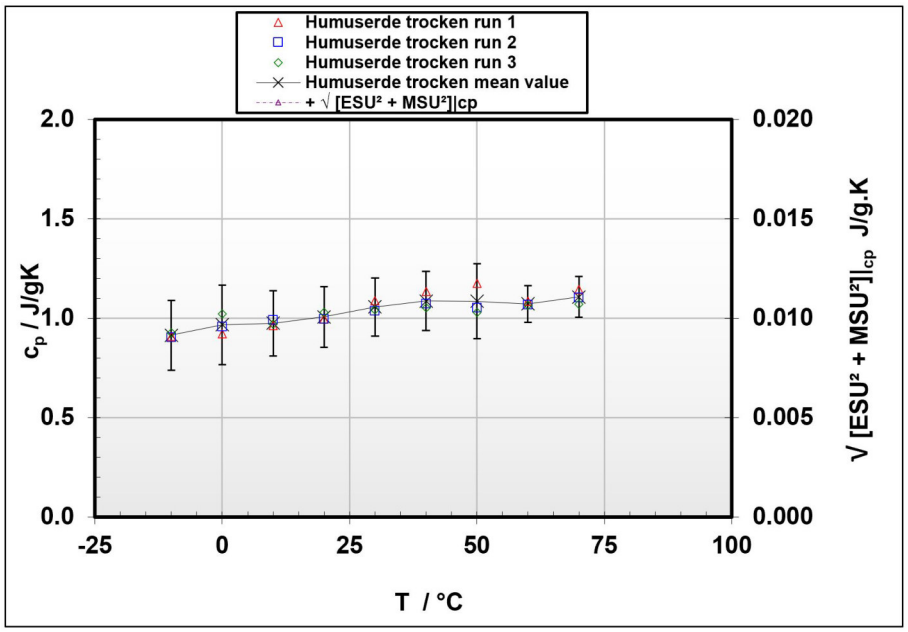

Measurements and statistical analysis of specific heat capacity of dry humus probes. [3]

[3] AIT Austrian Institute of Technology. (2020). GEOFIT research project

Humuserde trocken	Measurement procedure acoording to DIN EN 12664, DIN EN 12667, DIN EN 12939, ISO 8301, ASTM C518 and JIS A1412				Start of measurement:		01.07.2020
					Gas flow:		Ambient / Static
					Isothermal conditions ∂T/∂t:		< 0,1 K/min
	measured data λ / W/m.K			mean value λ / W/m.K	statistical analysis: k = 2 λ / W/m.K		
T / °C	run 1	run 2	run 3	mean value	+ √ [ESU² + MSU²]|λ	SDV|λ	$u_c(\lambda)$
-10	0.3377	0.3420	0.3407	0.3401	0.01251	0.00220	0.02540
0	0.3344	0.3392	0.3372	0.3370	0.01195	0.00239	0.02437
10	0.3213	0.3283	0.3257	0.3251	0.00558	0.00351	0.01318
20	0.3087	0.3193	0.3207	0.3162	0.00237	0.00652	0.01388
25	0.3059	0.3153	0.3152	0.3121	0.00115	0.00540	0.01104
30	0.2990	0.3109	0.3106	0.3068	0.00326	0.00676	0.01502
40	0.3030	0.2936	0.3008	0.2991	0.00812	0.00489	0.01897
50	0.3044	0.3081	0.3049	0.3058	0.00828	0.00201	0.01704
60	0.3019	0.3024	0.3029	0.3024	0.00994	0.00053	0.01992
70	0.2958	0.2981	0.2979	0.2972	0.01177	0.00128	0.02368

Humuserde trocken					Start of measurement:		01.07.2020
					Gas flow:		Ambient / Static
					Isothermal conditions ∂T/∂t:		< 0,1 K/min
	measured data c_p / J/gK			mean value c_p / J/gK	statistical analysis: k = 2 c_p / J/gK		
T / °C	run 1	run 2	run 3	mean value	+ √ [ESU² + MSU²]]cp	$SDV\|_{cp}$	$u_c(c_p)$
-10	0.909	0.904	0.927	0.913	0.08694	0.01173	0.17546
0	0.921	0.957	1.020	0.966	0.08694	0.04998	0.20057
10	0.961	0.991	0.970	0.974	0.08044	0.01525	0.16374
20	0.994	0.996	1.028	1.006	0.07406	0.01936	0.15309
30	1.089	1.037	1.042	1.056	0.06748	0.02857	0.14656
40	1.134	1.072	1.052	1.086	0.06047	0.04277	0.14814
50	1.174	1.053	1.029	1.085	0.05287	0.07792	0.18832
60	1.084	1.066	1.065	1.072	0.04461	0.01063	0.09171
70	1.145	1.103	1.071	1.106	0.03565	0.03697	0.10271